The role of charge recombination to triplet excitons in organic solar cells

Alexander J. Gillett[1], Alberto Privitera[2], Rishat Dilmurat[3], Akchheta Karki[4], Deping Qian[5], Anton Pershin[3,6], Giacomo Londi[3], William K. Myers[7], Jaewon Lee[4,8], Jun Yuan[5,9], Seo-Jin Ko[4,10], Moritz K. Riede[2], Feng Gao[5], Guillermo C. Bazan[4], Akshay Rao[1], Thuc-Quyen Nguyen[4*], David Beljonne[3*] and Richard H. Friend[1*].*

[1]Cavendish Laboratory, University of Cambridge, JJ Thomson Avenue, Cambridge, CB3 0HE, UK.

[2]Clarendon Laboratory, University of Oxford, Parks Road, Oxford, OX1 3PU, UK.

[3]Laboratory for Chemistry of Novel Materials, Université de Mons, Place du Parc 20, 7000 Mons, Belgium.

[4]Centre for Polymers and Organic Solids, Department of Chemistry and Biochemistry, University of California at Santa Barbara, CA 93106, USA.

[5]Department of Physics, Chemistry and Biology (IFM), Linköping University, Linköping, 58183, Sweden.

[6]Wigner Research Centre for Physics, PO Box 49, H-1525, Budapest, Hungary.

[7]Centre for Advanced ESR, Inorganic Chemistry Laboratory, University of Oxford, South Parks Road, Oxford, OX1 3QR, UK.

[8]Department of Chemical Engineering and Applied Chemistry, Chungnam National University, 99, Daehak-ro, Yuseong-gu, Daejeon, 34134, Republic of Korea.

[9]College of Chemistry and Chemical Engineering, Central South University, Changsha, 410083, P.R. China.

[10]Division of Advanced Materials, Korea Research Institute of Chemical Technology, Daejeon 34114, Republic of Korea.

*Corresponding authors: Alexander J. Gillett: E-mail: ajg216@cam.ac.uk; Thuc-Quyen Nguyen: E-mail: quyen@chem.ucsb.edu; David Beljonne: E-mail: david.beljonne@umons.ac.be; Richard H. Friend: E-mail: rhf10@cam.ac.uk.

The power conversion efficiencies (PCEs) of organic solar cells (OSCs) using non-fullerene acceptors (NFAs) have now reached 18%[1]. However, this is still lower than inorganic solar cells, for which PCEs >20% are commonplace[2]. A key reason is that OSCs still show low open-circuit voltages (V_{OC}) relative to their optical band gaps[3], attributed to non-radiative recombination[4]. For OSCs to compete with inorganics in efficiency, all non-radiative loss pathways must be identified and where possible, removed. Here, we show that in most NFA OSCs, the majority of charge recombination at open-circuit proceeds *via* formation of non-emissive NFA triplet excitons (T_1); in the benchmark PM6:Y6 blend[5], this fraction reaches 90%, contributing 60 mV to the reduction of V_{OC}. We develop a new design to prevent recombination *via* this non-radiative channel through the engineering of significant hybridisation between the NFA T_1 and the spin-triplet charge transfer exciton (^{3}CTE). We model that the rate of the back charge transfer from ^{3}CTE to T_1 can be reduced by an order of magnitude, allowing re-dissociation of the ^{3}CTE. We then demonstrate NFA systems where T_1 formation is suppressed. This work therefore provides a clear design pathway for improved OSC performance to 20% PCE and beyond.

Within the Shockley-Queisser model, an ideal solar cell should possess only radiative recombination, thus also acting as an ideal light emitting diode with 100% electroluminescence external quantum efficiency (EQE_{EL})[4,6–8]. This sets the limit to the photon energy loss (ΔE_{loss}), defined as the difference between the optical band gap (E_g) and the energy of the extracted charges (qV_{OC})[4]. However, when the EQE_{EL} falls below 1, non-radiative recombination incurs an additional voltage loss (ΔV_{nr})[7,8]:

$$\Delta V_{nr} = \frac{-k_B T}{q} ln(EQE_{EL}) \quad (1)$$

where k_B is the Boltzmann constant, T is temperature and q is the elementary charge. In most non-fullerene acceptor (NFA) organic solar cells (OSCs), EQE_{EL} is currently ~10^{-4}-10^{-5}, giving ΔV_{nr} ~230-290 mV and ΔE_{loss} =500-600 meV[3,9–12]. Thus, for PCEs >20% to be achieved in OSCs, ΔE_{loss} must be reduced[13,14], with ΔV_{nr} the key area for improvement[13,15]. To better understand the factors controlling the EQE_{EL}, it is useful to separate the different contributions[16]:

$$EQE_{EL} = \gamma \Phi_{PL} \chi \eta_{out} \quad (2)$$

where γ is the charge balance factor (often engineered to be ~1), Φ_{PL} is the photoluminescence quantum efficiency, χ is the fraction of recombination events that can decay radiatively (excitons in the spin-singlet configuration, S_1) and η_{out} is the photon out-coupling efficiency (typically ~0.3). Here, the two key factors that can be manipulated are Φ_{PL} and χ. For OSCs, we treat Φ_{PL} as equivalent to the luminescence yield of spin-singlet excitations. In an efficient OSC, almost all photo-generated S_1 dissociate into free charges (FCs); photon emission will occur following FC recombination. Thus, in the situation where recombination is able to proceed *via* the S_1 state of the lowest E_g component[11,17], we consider that Φ_{PL} of the neat low E_g material will set the upper limit for Φ_{PL} in an OSC blend. Whilst the recent empirical advances in EQE_{EL} have been achieved by raising Φ_{PL}[11,13,18,19], here, we address the role of χ in NFA OSCs.

In OSCs, the recombination of FCs proceeds *via* the formation of charge transfer excitons (CTEs), with an electron on the acceptor (A) and a hole on the donor (D) material. These CTEs will be created in a 1:3 ratio of spin-singlet (^{1}CTE) and spin-triplet (^{3}CTE) states

via spin-statistical non-geminate recombination[20]. However, OSC systems studied to date possess molecular triplet states (T_1) lower in energy than the ^{3}CTE on either the D or A. Thus, it is possible for back charge transfer (BCT) from ^{3}CTE to T_1 to occur[21–23]. Since the S_1-T_1 energy gap in most organic semiconductors is ~0.6–1 eV[24], T_1 will be too low in energy to thermally re-dissociate and must decay non-radiatively[25], resulting in χ <1 and an increased ΔV_{nr}[26]. To understand whether a system will generate T_1, it is necessary to analyse the competing processes that can occur from the ^{3}CTE. This includes BCT, re-dissociation into FCs, and conversion to ^{1}CTE. We note that ^{3}CTE-^{1}CTE conversion, with a typical rate of 10^8-10^6 s^{-1}, is too slow to compete with the other pathways (*vide infra*)[27]. Thus, T_1 formation from ^{3}CTE is determined by the competition between the rates of BCT (k_{BCT}) and re-dissociation ($k_{dissociation}$) of ^{3}CTE[22,28]. Furthermore, as ^{3}CTEs can be formed from both geminate[29,30] (Fig. 1a) and non-geminate[22,31,32] (Fig. 1b) charge carrier pairs, it is also important to consider that BCT to T_1 can occur through two distinct mechanisms.

In OSCs that use fullerenes as electron acceptors, T_1 generation is generally observed and has already been extensively studied, though the impact on device performance is debated[22,26,29–31,33–35]. In this work, we address the role of triplet states in NFA OSCs by examining nine high performance systems. The structures of the four polymer donors and seven NFAs used in this study are shown in Fig. 1c. A summary of device performance (current density-voltage and EQE_{EL} curves in Figs. S2-S3), Φ_{PL} for a neat film of the relevant NFA, ΔV_{nr}, and whether the blend exhibits geminate or non-geminate T_1 formation are given in Table 1. We find that geminate T_1 formation, as determined by transient electron paramagnetic resonance (trEPR) spectroscopy, is not observed in our NFA blends. However, non-geminate T_1 formation, probed through transient absorption (TA) spectroscopy, is generally seen, with the exception of the closely-related PTB7-Th:IEICO-0F and PTB7-Th:IEICO-2F systems.

Two NFA blends were selected to act as representative case studies; PM6:Y6 as one of the best performing OSC systems[5], despite exhibiting non-geminate T_1 formation, and PTB7-Th:IEICO-2F, which has no detectable BCT T_1. A full account of all other blends is in the SI.

Fig. 2a shows the TA of PM6:Y6, pumped at 532 nm for preferential PM6 excitation. Here, we focus solely on the infrared probe spectral region where the photo-induced absorptions (PIAs) of T_1 states are typically found (full spectral range TA in Fig. S14)[22]. At 0.1-0.2 ps after excitation, we observe PIA bands at 1250 nm and 1550 nm; though comparison to the TA of the neat materials (Figs. S5-6), these are respectively assigned to the PM6 S_1 and an intermolecular excitation between neighbouring Y6 molecules[36]. As charge transfer develops, these features are lost and a new PIA at 1450 nm grows beyond a few picoseconds, confirmed to be the Y6 T_1 by triplet sensitisation experiments (Fig. S4b). Kinetics from the T_1 spectral region (Fig. 2b) show a strong fluence dependence in T_1 formation, demonstrating that triplets are generated *via* bimolecular processes. Deviation of the T_1 region kinetics of the lowest and highest fluences begins on sub-picosecond timescales, demonstrating that non-geminate recombination can occur extremely quickly when the excitation fluence is high; from this, we can infer that k_{BCT} of the interfacial ^{3}CTE must be ~10^{11}-10^{12} s^{-1}. To determine $k_{dissociation}$, we have fitted the growth of the electro-absorption feature of the donor polymer in multiple blends (Figs. S29-S34), which is signature for the separation of interfacial CTEs into FCs[37–39]. Fitting reveals that $k_{dissociation}$ of the thermalized interfacial CTEs is between 10^{10}-10^{11} s^{-1} for the NFA blends studied here. Thus, we can rationalise why T_1 is observed in PM6:Y6 as $k_{BCT} >> k_{dissociation}$. Furthermore, utilising a previously employed kinetic model (full details in SI), we determine that ~90% of the recombination in this blend under conditions equivalent to open-circuit (no carriers are extracted from the film) proceeds non-radiatively *via* the Y6 T_1 (Fig. S37). The T_1 recombination fraction can be greater than the 75% predicted by spin-

statistics as CTEs form and separate multiple times prior to recombining[31,40]. We note that the presence of non-geminate T_1 formation in PM6:Y6 is representative of most NFA blends studied in this work.

When recombination via T_1 is present, it will accelerate the recombination of FCs *via* CTEs by providing an additional deactivation pathway. However, it has been reported that the bimolecular recombination rates of efficient NFA OSCs are significantly reduced from the Langevin rate[41,42]. In our TA measurements, we only detect the terminal recombination mechanism, not the preceding unsuccessful recombination attempts. Therefore, the high k_{BCT} we measure is only relevant for ^{3}CTEs at the D:A interface where rapid BCT to T_1 is favoured. Consistent with the large Langevin reduction factors reported, most recombination attempts must therefore be taking place at increased electron-hole separations where $k_{dissociation} >> k_{BCT}$, enabling rapid thermal ^{3}CTE re-dissociation. However, under open-circuit conditions, thermodynamics is the sole factor determining ΔV_{nr}[7,8]. Thus, the only relevant consideration for ΔV_{nr} is the final state through which terminal recombination takes place, not the kinetics of the preceding processes.

We next turn to trEPR to investigate geminate T_1 pathways. Fig. 2c shows the trEPR spectra of PM6:Y6 after 532 nm excitation (full discussion in Fig. S53). At 1 μs, we observe a single, intense peak at 346 mT that can be attributed to FCs[43] and a broader weak triplet feature. However, at 5 μs there are no remaining triplet signals, likely due to the rapid triplet-charge annihilation in this blend (Fig. S38). The triplet detected at 1 μs can be simulated by a single *eeeaaa* (*e* =emission, *a* =absorption) species, characteristic of T_1 formed *via* intersystem crossing (ISC) mediated by spin-orbit coupling (SOC)[23,44,45]; we attribute this T_1 to ISC from un-dissociated S_1 states. Importantly, the absence of any triplet species with an *aeeeae* or

eaaeea polarisation pattern, a clear and unique fingerprint of the geminate BCT pathway[23,44,45], confirms that geminate T_1 formation does not occur in this blend. This is a characteristic observation of all the NFA OSC systems studied.

We now focus on PTB7-Th:IEICO-2F, an NFA blend where T_1 generation from CTEs could not be detected; its TA is shown in Fig. 2d (excitation at 620 nm preferentially pumped PTB7-Th). In the infrared probe region (full spectral range data in Fig. S17), two distinct PIA features at 1175 nm and 1550 nm are observed at the earliest time of 0.2-0.3 ps. Through comparison to the TA of the neat materials (Figs. S7-S8), we assign the feature at 1175 nm to the edge of the IEICO-2F S_1 and the 1550 nm band to the PTB7-Th S_1. As charge transfer develops, both PIAs are lost and only the edge of the PTB7-Th hole PIA is visible at 1175 nm. Importantly, there is no detectable formation of the IEICO-2F T_1 PIA, found to be at 1350 nm from triplet sensitisation measurements (Fig. S4c). Furthermore, there is no fluence dependence of the kinetics taken from the IEICO-2F T_1 region (Fig. 2e), providing additional evidence that non-geminate T_1 formation is not a detectable recombination pathway.

In the trEPR of PTB7-Th:IEICO-2F excited at 532 nm (Fig. 2f, full discussion in Fig. S57), we observe a prominent SOC-ISC T_1 feature with a clear *eeeaaa* polarisation pattern that inverts to *aaaeee* by 5 μs[23,44,45], as well as an *ea* polarisation ^{3}CTE at 346 mT that evolves into FC[23]. The T_1 spectral inversion by 5 μs is due to differing decay rates from the three high-field triplet levels[46]. To explain the increased ISC T_1 intensity in PTB7-Th:IEICO-2F, we note that the IEICO derivatives exhibit relatively high ISC quantum yields of ~5% (Fig. S35), meaning substantial T_1 formation from any un-dissociated S_1 is expected. However, geminate BCT T_1 states are absent.

We next evaluate the impact of T_1 formation on device performance. In PM6:Y6, we have shown that ~90% of the recombination at open-circuit proceeds non-radiatively *via* the Y6 T_1; this equates to χ =0.1, reducing the EQE_{EL} by a factor of ten. From equation 1, this increases ΔV_{nr} by ~60 mV. We corroborate this ΔV_{nr} increase in the PTB7-Th:IEICO-2F and PTB7-Th:IEICO-4F blends, where only PTB7-Th:IEICO-4F exhibits non-geminate T_1 formation (Fig. S26), due to a poorer energy alignment between ^{3}CTE and T_1 (Fig. S66). Here, the NFA structures differ only by two fluorine atoms and the NFA S_1 (PTB7-Th blend ^{1}CTE) energies are 1.36 and 1.34 eV (1.29 and 1.26 eV) for IEICO-2F and IEICO-4F, respectively (Fig. S62). This enables a direct appraisal of the contribution from T_1 formation to ΔV_{nr} without a significant influence of molecular structure, Φ_{PL}, the absolute energies of S_1 and ^{1}CTE, and the S_1-^{1}CTE offset[17,47]. A ΔV_{nr} =0.28 V is obtained for PTB7-Th:IEICO-2F, whereas ΔV_{nr} =0.34 V is found for PTB7-Th:IEICO-4F (Fig. S3), consistent with our estimate of ~60 mV extra losses from significant recombination *via* T_1.

In the blends presented here, we find the highest ΔV_{nr} values (≥0.35 V) in systems with large S_1-^{1}CTE offsets and recombination *via* T_1 (PM6:IT-4F, PBDB-T:ITIC, J51:ITIC, Table S1); due to the large S_1-^{1}CTE energy gap, thermal reactivation from ^{1}CTE to the bright NFA S_1 state is not efficient[17,42]. Consequently, the primary radiative pathway available is *via* the ^{1}CTE, where Φ_{PL} is ~100 times lower than the NFA S_1[17]. The smaller ΔV_{nr} (<0.35 V) blends are those with reduced S_1-^{1}CTE gaps. We note that in low offset systems, ΔV_{nr} is particularly sensitive to the S_1-^{1}CTE energy gap[17]. However, we can generally rationalise the observed ΔV_{nr} using Φ_{PL} for the NFA and the presence or absence of recombination *via* T_1. For example, both PM6:Y6 and PTB7-Th:IEICO-0F possess an S_1-^{1}CTE offset of ~50 meV (Fig. S63). However, despite the significantly lower Φ_{PL} (0.6%) for IEICO-0F compared to Y6 (1.3%), we report the

lowest ΔV_{nr} =0.22 V in PTB7-Th:IEICO-0F (PM6:Y6 =0.25 V). Therefore, the improved ΔV_{nr} can be directly attributed to the suppressed recombination *via* T_1 in PTB7-Th:IEICO-0F.

To optimise power conversion efficiencies, we consider it of critical importance that OSCs are designed to avoid T_1 formation. We have therefore explored the role of D:A intermolecular interactions in T_1 generation through quantum-chemical calculations. Beginning with PTB7-Th:IEICO-2F, we have calculated the ^{1}CTE and ^{3}CTE energies at the equilibrium D:A geometry. We find the energy ordering of the CTEs is inverted from that expected when considering the electron exchange interaction[24], with the ^{3}CTE higher than the ^{1}CTE by ~70 meV. We next calculate the ^{1}CTE and ^{3}CTE excitation energies as a function of D:A separation. The results displayed in Fig. 3a show that below 0.5 nm, the ^{1}CTE is rapidly stabilised, whilst the ^{3}CTE is destabilised. In contrast, the explored PM6:Y6 configurations display the expected ordering with ^{1}CTE above ^{3}CTE (Figs. 3b and S66). By analysing the excited-state wavefunctions, we conclude that the inversion of ^{1}CTE and ^{3}CTE in PTB7-Th:IEICO-2F arises from hybridisation between the CTEs and local excitons (LEs)[11,18,19]. Inversion occurs because the NFA S_1 is higher in energy than the ^{1}CTE and the NFA T_1 is lower than the ^{3}CTE; hybridisation of these states therefore stabilises the ^{1}CTE and destabilises the ^{3}CTE (Fig. 3c). The primary reason for hybridisation is the enhanced electronic coupling in the PTB7-Th:IEICO-2F complex, due to: (i) the similar bonding-antibonding pattern of the highest-occupied molecular orbitals, with the same sequence of vertical nodal planes along the main molecular axis (Figs. 3d and S70); and (ii) the near-perfect registry between the NFA and the polymer backbone, offering significant molecular overlap (Fig. S65). The PM6 and Y6 combination does not possess these attributes and hence does not exhibit CTE:LE hybridisation. Additionally, we find excellent agreement between our calculations and

experimental observations, with BCT T_1 formation only suppressed in the blends that exhibit significant CTE:LE hybridisation (Figs. 3a, 3b, S67).

The consequence of hybridisation destabilising the ^{3}CTE at close D:A separations is that it causes the electron and hole to remain more distant in the spin-triplet configuration, effectively increasing the interfacial ^{3}CTE radius. As the D:A electronic coupling, and thus k_{BCT}, falls exponentially with distance[48], this can provide additional time for the thermal re-dissociation of ^{3}CTE[49]. Our calculations of the CTE energies as a function of intermolecular separation for the PTB7-Th:IEICO-2F complex indicate that CTE:LE hybridisation results in a new ^{3}CTE energetic minima at a D:A stacking distance of 0.42 nm. When comparing k_{BCT} to the IEICO-2F T_1 at 0.42 nm to 0.35 nm, we observe that it is reduced by an order of magnitude from ~10^{12} s^{-1} to ~10^{11} s^{-1} (Fig. 3a). Consistent with our experimental observations where the NFA T_1 is populated *via* BCT, we also find that when the D polymer T_1 is energetically accessible from ^{3}CTE, k_{BCT} to the NFA is consistently higher (Fig. S64). Critically, the $k_{dissociation}$ of between 10^{10}-10^{11} s^{-1} that we observe experimentally in our NFA OSCs is comparable to the reduced k_{BCT} enabled by CTE:LE hybridisation, confirming that it is a feasible route to suppress BCT to T_1. We note that in thin films of organic semiconductors, there will be a range of intermolecular stacking distances (broadly centred around ~0.38 nm in conjugated polymers) due to disorder induced by the side chains[50]. Thus, in an operational OSC blend, our calculations suggest that the ^{3}CTE excitations will preferentially locate at lower energy interfacial sites with increased D:A stacking distances and reduced k_{BCT}.

From these observations, we offer design rules that encourage (triplet) CTE:LE hybridisation in OSC blends: (i) close energy resonance (preferably <100 meV) between the interacting LE and CTE states; (ii) strong overlap and phase matching between the interacting

frontier molecular orbital wavefunctions of the D and A; and (iii) spatial registry between the D and A materials, allowing for the close intermolecular contacts necessary for strong wavefunction interactions.

Whilst the importance of optimising Φ_{PL} in OSCs is already well known[13], the insight provided by this work demonstrates the critical role of T_1 states in ΔE_{loss}. If T_1 formation can be suppressed, with ^{3}CTE-T_1 hybridisation providing one viable pathway, ΔE_{loss} can be reduced by ~60 meV; enough to enable PCEs of 20% with the current best device performance metrics[13,14]. Therefore, future OSC development should focus on simultaneously increasing Φ_{PL} and engineering-out T_1 formation. To achieve this, quantum chemical calculations on the D:A electronic interactions will provide a valuable predictive tool for screening perspective D:A pairs *in silico*. Furthermore, we anticipate the unprecedented spin-control over charge recombination demonstrated here will be of great interest to the broader field of excitonic semiconductors.

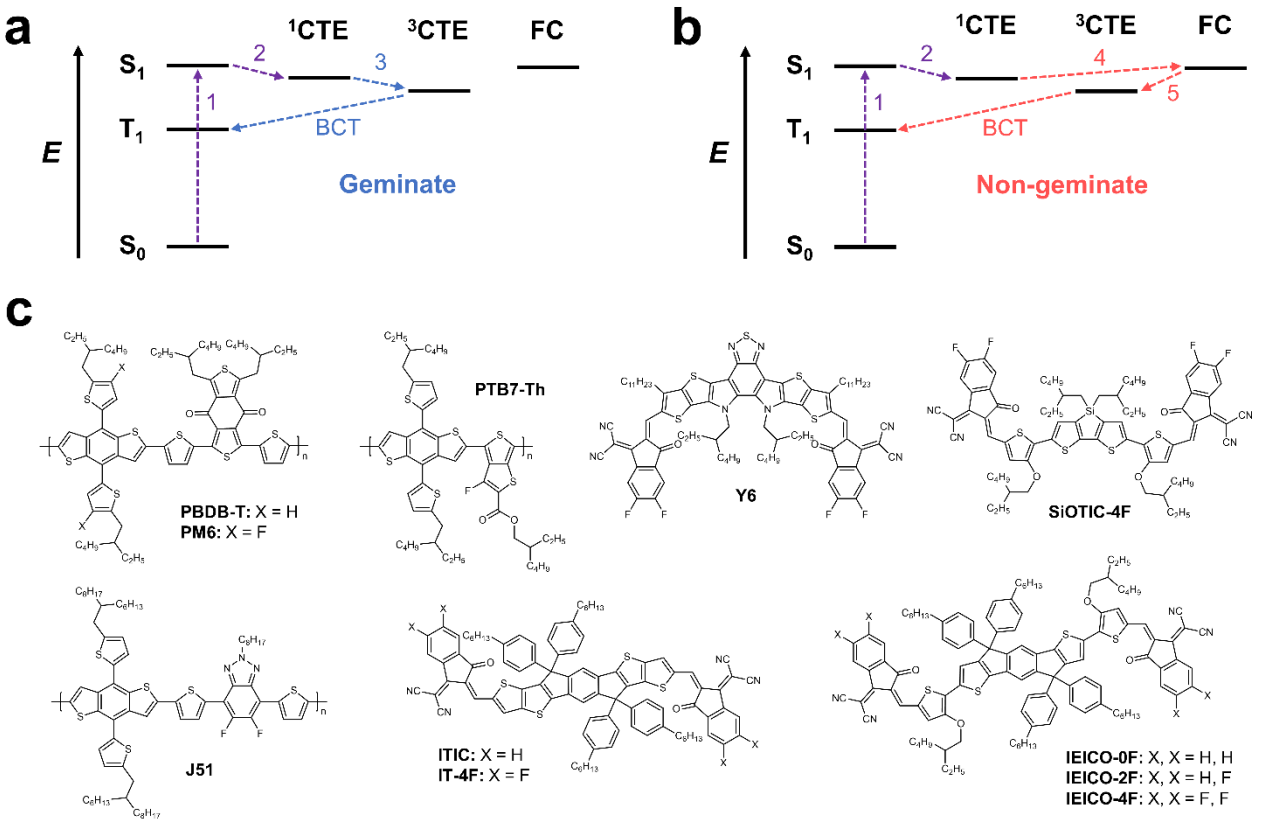

Figure 1: The triplet formation pathways and organic solar cell materials investigated in this study. (a) A diagram to illustrate the geminate pathway for T_1 formation in OSCs. After optical excitation (1), charge transfer from the S_1 to ^{1}CTE occurs (2). However, the ^{1}CTE does not manage to separate into FC before spin-mixing with the ^{3}CTE occurs on ns timescales (3). From the ^{3}CTE, BCT to a lower energy T_1 on either the D or A can occur. **(b)** A diagram to illustrate the non-geminate pathway for T_1 formation in OSCs. After optical excitation (1), charge transfer from the S_1 to ^{1}CTE occurs (2). The ^{1}CTE then successfully dissociates in FC (4). The FC then undergo non-geminate recombination, forming a 3:1 ratio of ^{3}CTE to ^{1}CTE (5). From the ^{3}CTE, BCT to a lower energy T_1 on either the D or A can occur. **(c)** The molecular structures of the four polymer donors and seven NFA materials used in this study.

Blend	PCE (%)	Φ_{PL} of NFA (%)	EQE_{EL}	ΔV_{nr} (V)	Geminate T_1	Non-geminate T_1
PM6:Y6	15.2	1.3	4.3×10^{-5}	0.25	No	Yes
PM6:IT-4F	12.0	1.4	9.5×10^{-7}	0.35	No	Yes
PM6:ITIC	9.2	1.4	5.0×10^{-5}	0.25	No	Yes
PBDB-T:ITIC	11.2	1.4	8.8×10^{-7}	0.35	No	Yes
J51:ITIC	7.2	1.4	7.1×10^{-8}	0.42	No	Yes
PTB7-Th: SiOTIC-4F	8.9	<0.1*	8.7×10^{-7}	0.35	No	Yes
PTB7-Th: IEICO-4F	10.2	0.4	1.6×10^{-6}	0.34	No	Yes
PTB7-Th: IEICO-2F	11.7	0.4	1.3×10^{-5}	0.28	No	No
PTB7-Th: IEICO-0F	7.2	0.6	1.4×10^{-4}	0.22	No	No

Table 1: A summary of the key parameters for the OSC blends investigated in this study. Φ_{PL} was measured for a neat film of the NFA used in the blend. The error in the Φ_{PL} is ±0.1%. *Φ_{PL} of SiOTIC-4F was too low to be measured and is therefore quoted as less than the smallest value reliably resolvable on our setup (0.1%). For the determination of ΔV_{nr}, the EQE_{EL} at 293 K was taken at $-J_{SC}$ to ensure that carrier densities were relevant to device operating conditions. Additionally, it is stated whether the blend forms triplet excitons resulting from either geminate or non-geminate recombination pathways.

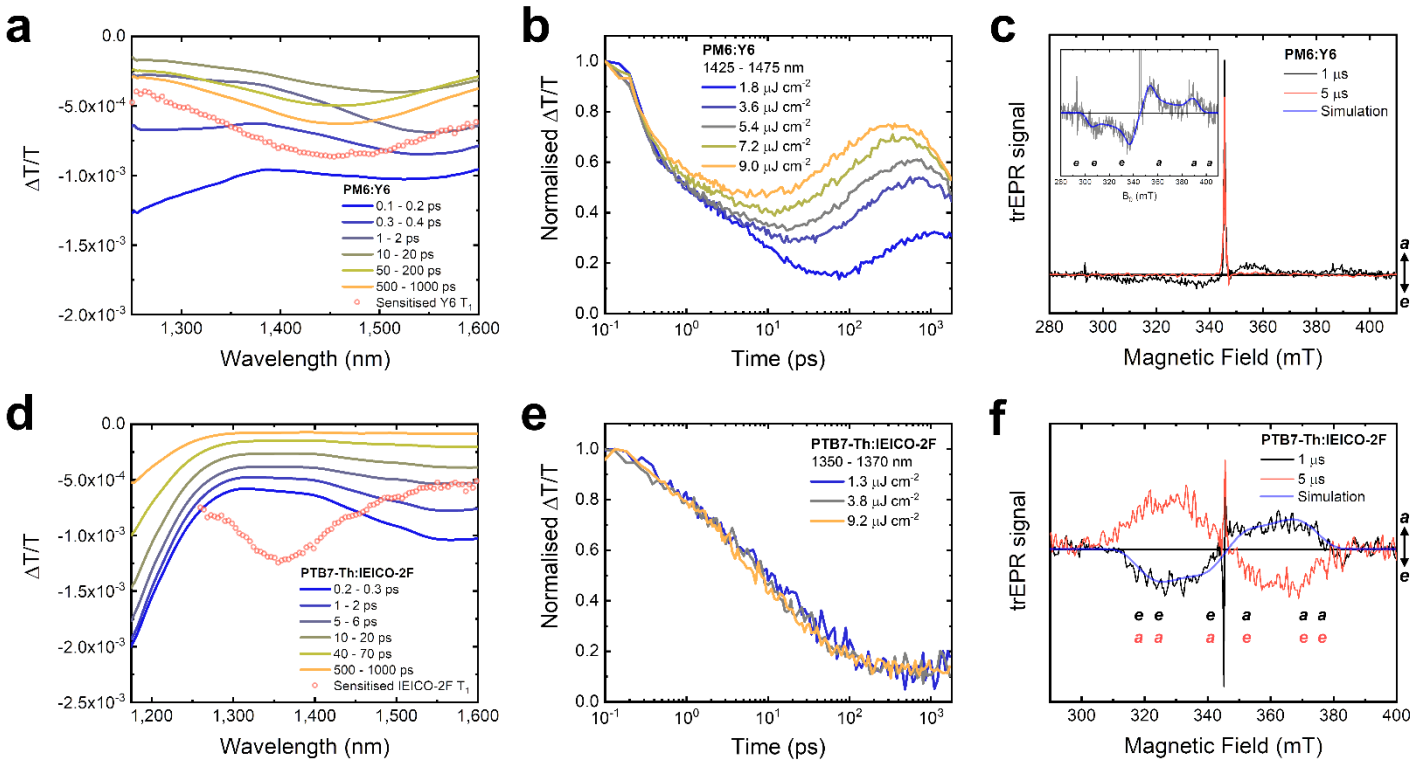

Figure 2: Spectroscopic investigations of triplet formation in model non-fullerene acceptor blends. (a) The IR region TA spectra of the PM6:Y6 blend (293 K), excited with a moderate fluence of 5.4 μJ cm^{-2} at 532 nm for preferential PM6 excitation. The Y6 T_1 PIA forms at 1450 nm, as confirmed by triplet sensitisation experiments. **(b)** The normalised TA kinetics of the PM6:Y6 blend, taken around the maximum of the Y6 T_1 feature between 1425 – 1475 nm. The clear fluence dependence of T_1 formation is indicative of a bimolecular generation pathway. **(c)** The trEPR spectra of the PM6:Y6 blend (80 K) after excitation at 532 nm, taken at 1 and 5 μs. The inset shows a magnification and simulation of the weak ISC triplet signal. The field positions of the absorption (*a*) and emission (*e*) EPR transitions of the ISC triplet are overlaid on the plot for clarity. **(d)** The IR region TA spectra of the PTB7-Th:IEICO-2F blend (293 K), excited with a moderate fluence of 3.8 μJ cm^{-2} at 620 nm for preferential PTB7-Th excitation. The IEICO-2F T_1 PIA at 1350 nm does not form in the blend. **(e)** The normalised TA kinetics of the PTB7-Th:IEICO-2F blend, taken around the maximum of the IEICO-2F T_1 PIA at 1350 – 1370 nm. No fluence dependence in the IEICO-2F T_1 region is observed. **(f)** The trEPR spectra of the PTB7-Th:IEICO-2F blend (80 K) after excitation at 532 nm, taken at 1 and 5 μs. The field positions of the absorption (*a*) and emission (*e*) EPR transitions of the ISC triplet are overlaid on the plot for clarity.

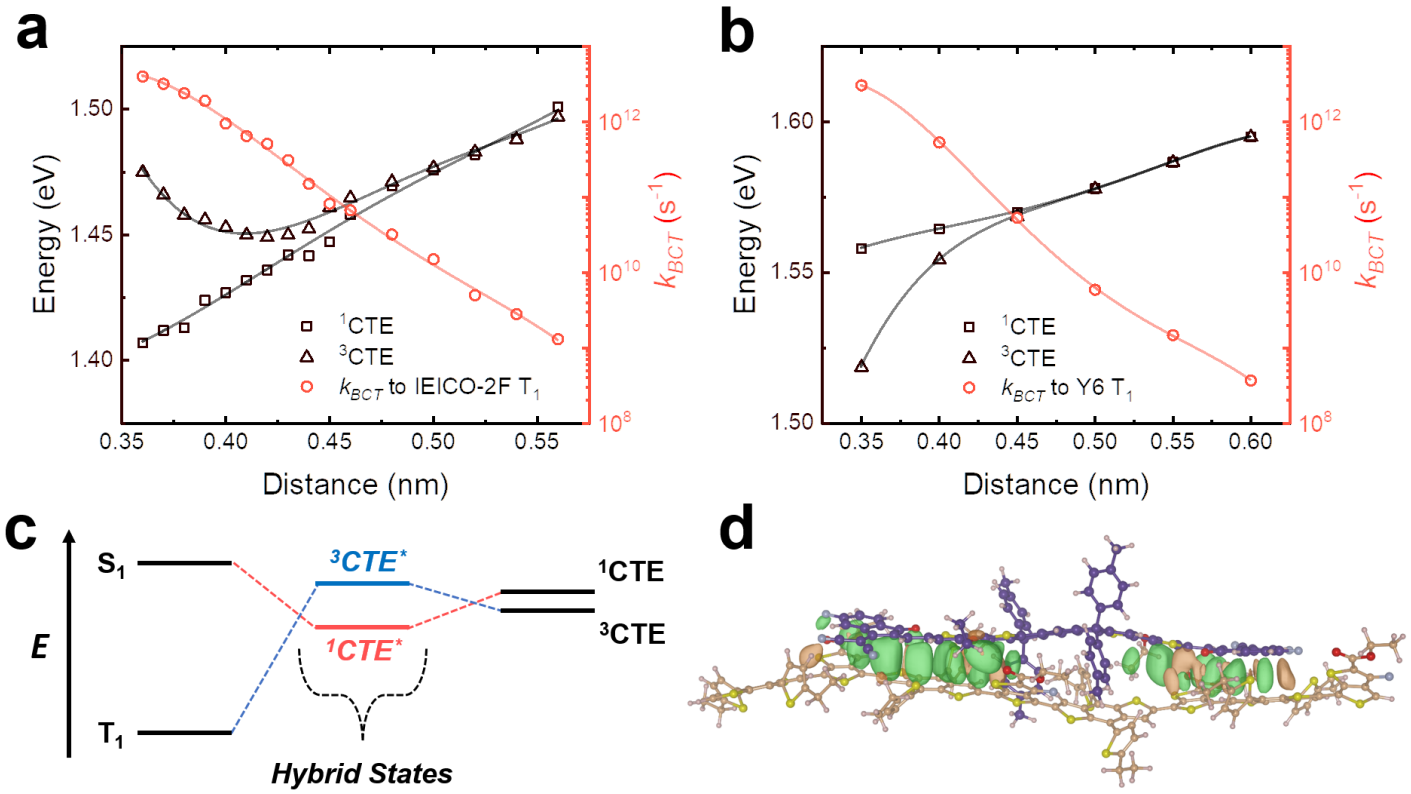

Figure 3: The role of hybridisation in organic solar cell blends. (a) The results of a rigid scan of the ^{1}CTE and ^{3}CTE energies for a representative PTB7-Th:IEICO-2F supramolecular configuration as a function of D:A separation. At each D:A separation, k_{BCT} from ^{3}CTE to T_1 of the NFA has also been calculated. The solid lines provide polynomial guides to the eye. **(b)** The results of a rigid scan of the ^{1}CTE and ^{3}CTE energies for a representative PM6:Y6 supramolecular configuration. At each D:A separation, k_{BCT} from ^{3}CTE to T_1 of the NFA has also been calculated. The solid lines provide polynomial guides to the eye. **(c)** A schematic to represent the effect of CTE-LE hybridisation on the energetic ordering of the ^{1}CTE and ^{3}CTE. **(d)** An image showing the same optimised supramolecular configuration between PTB7-Th (beige) IEICO-2F (purple) used for the calculations in Fig. 3a. The lobes represent regions of constructive overlap between the highest-occupied molecular orbitals (HOMOs) of D and A. The HOMO overlap that controls the size of the electronic coupling and thus mediates hybridisation between the NFA LE and the CTEs; for hybridisation between the LE states of the D polymer and the CTEs, the lowest occupied molecular orbital overlap is the relevant interaction.

Methods

Rate equations for the processes controlling triplet formation in OSC blends

In the event that BCT proceeds to the electron acceptor, k_{BCT} and $k_{dissociation}$ can be defined as[51]:

$$^3[D^+][A^-] \xrightarrow{k_{BCT}} {}^1_0[D] + {}^3_1[A] \quad (3)$$

$$^3[D^+][A^-] \xrightarrow{k_{dissociation}} [D^+] + [A^-] \quad (4)$$

Where $[D^+]$ is the free hole on the donor component, $[A^-]$ is the free electron on the acceptor material, $^3[D^+][A^-]$ represents the coulombically-bound ^{3}CTE, ${}^1_0[D]$ is the spin-singlet ground state of the donor and ${}^3_1[A]$ is T_1 of the acceptor. We note that the conversion of ^{3}CTE back into ^{1}CTE primarily occurs via hyperfine coupling (HFC), typically taking place with a rate of 10^8-10^6 s^{-1} in organic semiconductors[27]; we note that this is significantly slower than the k_{BCT} and $k_{dissociation}$ determined in our work, which are both on the order of 10^{10}-10^{12} s^{-1}. The rate of the HFC-induced ^{3}CTE-^{1}CTE interconversion process (k_{HFC}) is given by:

$$^3[D^+][A^-] \xrightarrow{k_{HFC}} {}^1[D^+][A^-] \quad (5)$$

Where $^1[D^+][A^-]$ represents the coulombically-bound ^{1}CTE. In addition to the primary geminate and non-geminate pathways occurring via CTEs that are discussed in our work, T_1 formation via direct SOC-ISC from un-dissociated S_1 states can also be considered a geminate T_1 formation mechanism and is the only geminate pathway detected in the trEPR measurements of our NFA blends. However, as it requires S_1 to remain undissociated, it will not be a

significant pathway in blends that exhibit efficient exciton dissociation and good device performance. The rate of intersystem crossing (k_{ISC}) from S_1 to T_1, defined here for the acceptor component, is given by:

$$ {}^1_1[A] \xrightarrow{k_{ISC}} + {}^3_1[A] \quad (6) $$

Where ${}^1_1[A]$ is S_1 of the acceptor.

OSC device fabrication

Indium tin oxide (ITO) patterned glass substrates were cleaned by scrubbing with soapy water, followed by sonication in soapy water, deionized (DI) water, acetone, and isopropanol for 20 minutes each. The substrates were dried using compressed nitrogen and placed in an oven overnight at 100 °C. The conventional architecture devices were made by treating the ITO substrates with UV-ozone for 15 minutes and spin-coating a layer of poly(3,4-ethylenedioxythiophene):poly(styrenesulfonate) (PEDOT:PSS, Clevios P VP Al 8043) at 3000 rpm for 40 s onto the ITO substrates in air. The substrates were then annealed in air at 150 °C for 20 minutes. Active layers were spin coated on top of the PEDOT:PSS layer inside a nitrogen filled glovebox following the recipes from previous reports[9,42,52]. The substrates were then pumped down under vacuum ($<10^{-7}$ torr), and a 5 nm thick Ca interlayer followed by a 100 nm thick Al electrode were deposited on top of the active layer by thermal evaporation using the Angstrom Engineering Series EQ Thermal Evaporator. In the case of inverted architecture devices, ZnO was used as the bottom transparent electrode (replacing PEDOT:PSS), where the ZnO solution was prepared in a nitrogen glovebox by mixing tetrahydrofuran and diethylzinc (2:1). The fresh ZnO solution was then spin-coated atop the clean ITO substrates at 4000 rpm for 30 seconds and then placed on a hotplate at 110 ^{0}C for 15 minutes. Following active layer

spin-coating, the inverted devices were pumped down under vacuum (<10^{-7} torr), and 7 nm of MoO_x and 100 nm thick Ag electrode were deposited on top of the active layer by thermal evaporation. The electrode overlap area was 0.22 cm^2 for both conventional and inverted devices. The active area of the device was determined using an optical microscope. The optimized active layer compositions used for the blend solutions were based on previously published reports[9,42,52].

OSC device testing

Photovoltaic characteristic measurements were carried out inside a N_2 filled glove box. Solar-cell device properties were measured under illumination by a simulated 100 mW cm^{-2} AM1.5 G light source using a 300 W Xe arc lamp with an AM 1.5 global filter. The irradiance was adjusted to 1 sun with a standard silicon photovoltaic cell calibrated by the National Renewable Energy Laboratory. No spectral mismatch correction was applied. A Keithley 2635A source measurement unit was used to scan the voltage applied to the solar cell between -2 to 1 V at a speed of 0.43 V/s with a dwell time of 46 ms. Scans were performed in both the forward and reverse directions, with no unusual behaviour observed. Between eight and 30 individual solar cell devices were tested for each blend reported. The error associated with the reported PCE values is ±0.2%.

Electroluminescence and EQE_{EL} measurements

EL measurements were performed using two setups depending on the wavelength range of interest. For measurements under 1050 nm, a home-made EL spectrometer was used. The EL emission from a sample driven by a Keithley source-measure unit (model 2602A) was collected by a lens system and focused on the entrance slit of a spectrograph (Acton Research SP-500) equipped with a Si charge-coupled detector (Princeton Instruments Pixis:400). The spectra

collected by the detector were corrected for the instrument response function. The correction factors were determined by measuring the spectrum of a black body-like light source (Ocean Optics LS-1). For EL measurements in the range 900 - 1700 nm, we utilized a Photon Technology International (PTI) Quantamaster fluorimeter equipped with an Edinburgh Instruments EI-L Ge detector. The excitation monochromator of the fluorimeter was not used, and the EL emission was generated by driving the devices by a Keithley 2602 source-measure unit. An optical chopper (Thorlabs MC2000) was placed in front of the emission monochromator to make use of the fluorimeter's lock-in amplifier-based detection system. The PTI Felix fluorimeter software was used for the data collection and correction of the instrumental artefacts. The efficiency of EL was obtained by applying a bias from -1 to 2V with a dual-channel Keithley 2602 to the solar cell and placing a silicon or germanium photodiode directly in front of it to collect the emission as a function of applied bias. The current running through the device and the photodiode were simultaneously measured.

Photoluminescence quantum efficiency measurements

The PLQE was determined using method previously described by De Mello *et al.*[53]. Samples were placed in an integrating sphere and photoexcited using a 658 nm continuous-wave laser. The laser and emission signals were measured and quantified using calibrated Andor iDus DU420A BVF Si and Andor CCD-1430 InGaAs detectors.

TA spectroscopy

In TA, T_1 states often possess distinct PIA features, allowing for their unambiguous assignment. Furthermore, by investigating the fluence dependence of the T_1 dynamics, we can readily determine whether formation follows the bimolecular kinetics expected for NGR[22], or the monomolecular kinetics anticipated if T_1 is produced from geminate processes[29]. We can

409 also quantify the T_1 population (N_T) directly from the TA signal through knowledge of the T_1
410 absorption cross section (σ_T), corresponding to the TA signal produced by a single T_1 state[54]
411 (see SI for more details).

412 $$\frac{\Delta T}{T} = \sigma_T N_T \quad (7)$$

413

414 Samples for TA measurements were fabricated by spin-coating solutions onto quartz substrates
415 using identical conditions to the optimised devices. The samples were encapsulated in a
416 nitrogen glovebox environment to ensure oxygen-free measurements.

417

418 TA was performed on either one of two experimental setups. The broadband probe (525 – 1650
419 nm) TA was performed on a setup powered using a commercially available Ti:sapphire
420 amplifier (Spectra Physics Solstice Ace). The amplifier operates at 1 kHz and generates 100 fs
421 pulses centred at 800 nm with an output of 7 W. A TOPAS optical parametric amplifier (OPA)
422 was used to provide the tuneable ~100 fs pump pulses for the "short-time" (100 fs – 1.8 ns) TA
423 measurements, whilst the second harmonic (532 nm) of an electronically triggered, Q-switched
424 Nd:YVO_4 laser (Advanced Optical Technologies Ltd AOT-YVO-25QSPX) provided the ~1 ns
425 pump pulses for the "long-time" (1 ns – 100 μs) TA measurements. The probe was provided
426 by a broadband visible (525 – 775 nm), NIR (800 – 1200 nm) and IR (1250 – 1650 nm) NOPAs.
427 The probe pulses are collected with an InGaAs dual-line array detector (Hamamatsu G11608-
428 512DA), driven and read out by a custom-built board from Stresing Entwicklungsbüro. The
429 probe beam was split into two identical beams by a 50/50 beamsplitter. This allowed for the
430 use of a second reference beam which also passes through the sample but does not interact with
431 the pump. The role of the reference was to correct for any shot-to-shot fluctuations in the probe
432 that would otherwise greatly increase the structured noise in our experiments. Through this
433 arrangement, very small signals with a $\frac{\Delta T}{T}$ =1x10^{-5} could be measured.

For the 500 – 950 nm continuous probe region TA, a Yb amplifier (PHAROS, Light Conversion), operating at 38 kHz and generating 200 fs pulses centred at 1030 nm with an output of 14.5 W was used. The ~200 fs pump pulse was provided by a TOPAS OPA. The probe is provided by a white light supercontinuum generated in a YAG crystal from a small amount of the 1030 nm fundamental. After passing through the sample, the probe is imaged using a Si photodiode array (Stresing S11490). This setup provided additional flexibility by allowing for broadband spectrum acquisition in one measurement, as well good signal to noise in the 750 – 850 nm region, which is difficult to obtain on the other setup due to large fluctuations in the NOPA probes around the 800 nm fundamental of the Ti:sapphire laser.

In our TA measurements on the PM6:Y6 blend, the excitation densities created by our 1.8 μJ cm^{-2} pulse at 532 nm is equivalent to "3 sun" operation conditions for PM6:Y6 (~$3x10^{17}$ cm^{-3})[42]. In contrast, the 9.0 μJ cm^{-2} pulse at 532 nm is equivalent to "15 sun" operation. We have intentionally performed our TA measurements at excitation densities in excess of those at "1 sun", as the increased rate of non-geminate recombination enables us to identify and model the triplet recombination pathways present in the OSC blends studied here. We note that under "1 sun" conditions, the lower excitation densities will increase the time taken to the onset of non-geminate recombination processes that result in T_1 formation, enabling charge carriers to be extracted before significant recombination losses to T_1 occur. This can explain why the PM6:Y6 devices investigated here (which have shown particularly efficient charge extraction[42]) can demonstrate excellent performance, despite 90% of recombination proceeding *via* the Y6 T_1 under open-circuit conditions.

trEPR spectroscopy

Triplet states can also be investigated using trEPR measurements, which allows for the detection of only spin-polarised triplets i.e. those where the spin sublevels T_+, T_0 and T_- have non-thermal occupancies[44]. As a result, we observe enhanced absorptive (*a*) and emissive (*e*) characters of the EPR transitions, from which the generation mechanism of the triplet can be determined[44]. Triplets produced via non-geminate recombination from FC have thermal sublevel occupancies and are thus not detectable[20]. Conversely, triplets produced from geminate processes result in sublevel occupancies far from thermal equilibrium and can be readily observed[23,44,45,55–57]. T_1 formation via geminate BCT can be understood in the framework of the spin-correlated radical pair mechanism[58–61], where spin-mixing first occurs between $^1CTE_0$ and $^3CTE_0$, followed by BCT to the molecular triplet sublevels. Depending on the sign of the zero-field splitting D-parameter, the overpopulation of either T_0 or T_+/T_- results in an *aeeaae* or *eaaeea* spin-polarization pattern of the T_1 trEPR signal; a clear and unique fingerprint of the geminate pathway[23,44,45]. Though performed at 80 K, we expect that these measurements are of relevance to the blend behaviour at 293 K; detailed discussions of the influence of temperature and an in-depth review of EPR theory are available in the SI.

EPR samples were fabricated by spin-coating solutions under identical conditions to the optimised devices onto Mylar substrates, which were subsequently cut into strips with a width of 3 mm. To ensure the flexible Mylar substrates did not bend during the spin coating process, they were mounted onto rigid glass substrates using adhesive tape. The strips were placed in quartz EPR tubes which were sealed in a nitrogen glovebox with a bi-component resin (Devcon 5-Minute Epoxy), ensuring that all EPR measurements were performed without oxygen exposure.

All trEPR spectra were recorded on a Bruker Elexsys E580 X-band spectrometer, equipped with a nitrogen gas-flow cryostat for sample temperature control. The sample temperature was maintained with an Oxford Instruments CF935O cryostat and controlled with an Oxford Instruments ITC503. Laser pulses for trEPR were collimated into the cryostat and resonator windows from a multi-mode optical fibre, ThorLabs FT600UMT. Sample excitation at 532 nm with an energy of 2 mJ per pulse and a duration of 7 ns was provided by the residual 2nd harmonic output of a Newport/Spectra Physics Lab 170 Quanta Ray Nd:YAG pulsed laser, operating at 20 Hz. The trEPR signal was recorded through a Bruker SpecJet II transient recorder with timing synchronisation by a Stanford Research Systems DG645 delay generator. The instrument response time was about 200 ns. The spectra were acquired with 2 mW microwave power and averaging 400 transient signals at each field position.

The trEPR spectra were recorded by adopting a direct-detection scheme[62]. Specifically, the EPR intensity was recorded as a function of time following laser excitation, with constant applied X-band microwave radiation, for each magnetic field position. We employed this configuration since it possesses better signal-to-noise ratio compared to the delay after flash (DAF) echo-detected experiments at 80 K. Indeed, most triplet states have relaxation times too short to be detectable with pulsed-detection scheme at 80 K. At lower temperatures (usually 20 K), pulsed detection usually becomes feasible, but the spectra may become quite complicated due to several paramagnetic species being present, including thermally populated triplets produced via non-geminate recombination from free charge carriers and stable states that are not usually observable using direct detection. From the data set obtained, the transient EPR spectrum at different time delays after the laser pulse has been extracted. The reported trEPR spectra have been averaged over a time window of 1 μs. The acquired trEPR spectra have been simulated by using the core functions *pepper* and *esfit* of the open-source MATLAB toolbox

EasySpin[63]. The parameters included in our best-fit simulations are the ZFS parameters (D and E), the triplet population sublevels (p_1, p_2, p_3) and the line broadening (assumed as only Lorentzian to not over-parametrize the fitting). For the calculation of spin polarization, the populations of the spin-triplet sublevels at zero field were calculated (T_x, T_y, T_z) in the fitting program and used by EasySpin to simulate the trEPR spectrum at resonant fields. For all the simulations, the *g* tensor was assumed isotropic with g_{iso}=2.002. To carry out our least-square fittings, a user-defined simulation function has been developed which allowed the fitting of "non-spin system" parameters, such as the spin populations of the triplet sublevels. All the fits were carried out using a Nelder/Mead downhill simplex optimisation algorithm.

Acknowledgements

A.J.G. and R.H.F. acknowledge support from the Simons Foundation (grant no. 601946) and the EPSRC (EP/M01083X/1 and EP/M005143/1). This project has received funding from the ERC under the European Union's Horizon 2020 research and innovation programme (grant agreement no. 670405). A.K. and T.-Q.N. were supported by the Department of the Navy, Office of Naval Research Award No. N00014-14-1-0580. A.K. acknowledges funding by the Schlumberger foundation. A.Privitera, R.D., A.Pershin, G.L., M.K.R. and D.B. were supported by the European Union's Horizon 2020 research and innovation programme under Marie Sklodowska Curie Grant agreement No.722651 (SEPOMO project). Computational resources in Mons were provided by the Consortium des Équipements de Calcul Intensif (CÉCI), funded by the Fonds de la Recherche Scientifiques de Belgique (F.R.S.-FNRS) under Grant No. 2.5020.11, as well as the Tier-1 supercomputer of the Fedération Wallonie-Bruxelles, infrastructure funded by the Walloon Region under Grant Agreement No. 1117545. D.B. is a FNRS Research Director. F.G. acknowledges the Stiftelsen för Strategisk Forskning through a Future Research Leader program (FFL18-0322). trEPR measurements were performed in the

Centre for Advanced ESR (CAESR) located in the Department of Chemistry of the University of Oxford, and this work was supported by the EPSRC (EP/L011972/1). We thank Till Biskup and Andreas Sperlich for their assistance with the simulation and interpretation of the trEPR data presented in this work.

Author contributions

A.J.G., T.-Q.N. and R.H.F. conceived the work. A.J.G. performed the TA measurements. A.Privitera and W.K.M. conducted the trEPR measurements. R.D., A.Pershin and G.L. carried out the quantum chemical calculations. A.K., D.Q., J.Y. and S.-J.K. fabricated and tested the OSC devices. A.J.G. and J.Y. performed the PLQE measurements. J.L. synthesised SiOTIC-4F and the IEICO derivatives. M.K.R., F.G., G.C.B., T.-Q.N, D.B. and R.H.F. supervised their group members involved in the project. A.J.G., A.R. and R.H.F. wrote the manuscript with input from all authors.

Competing financial interests

The authors declare no competing interests.

Additional information

Supplementary information accompanies this paper at [to be completed in proofs].

Correspondence and requests for materials should be addressed to R.H.F. (rhf10@cam.ac.uk), A.J.G. (ajg216@cam.ac.uk), D.B. (david.beljonne@umons.ac.be) and T.-Q.N. (quyen@chem.ucsb.edu).

Reprints and permissions information is available at www.nature.com/reprints.

Data availability

The data that supports the findings of this study are available from the corresponding authors upon reasonable request.

Bibliography

1. Liu, Q. *et al.* 18% Efficiency organic solar cells. *Sci. Bull.* **65**, 272–275 (2020).

2. Green, M. A. *et al.* Solar cell efficiency tables (Version 55). *Prog. Photovoltaics Res. Appl.* **28**, 3–15 (2020).

3. Liu, S. *et al.* High-efficiency organic solar cells with low non-radiative recombination loss and low energetic disorder. *Nat. Photonics* **14**, 300–305 (2020).

4. Menke, S. M., Ran, N. A., Bazan, G. C. & Friend, R. H. Understanding Energy Loss in Organic Solar Cells: Toward a New Efficiency Regime. *Joule* **2**, 25–35 (2018).

5. Yuan, J. *et al.* Single-Junction Organic Solar Cell with over 15% Efficiency Using Fused-Ring Acceptor with Electron-Deficient Core. *Joule* **3**, 1140–1151 (2019).

6. Shockley, W. & Queisser, H. J. Detailed Balance Limit of Efficiency of p-n Junction Solar Cells. *J. Appl. Phys.* **32**, 510–519 (1961).

7. Ross, R. T. Some Thermodynamics of Photochemical Systems. *J. Chem. Phys.* **46**, 4590–4593 (1967).

8. Rau, U. Reciprocity relation between photovoltaic quantum efficiency and electroluminescent emission of solar cells. *Phys. Rev. B* **76**, 085303 (2007).

9. Lee, J. *et al.* Design of Nonfullerene Acceptors with Near-Infrared Light Absorption Capabilities. *Adv. Energy Mater.* **8**, 1801209 (2018).

10. Cui, Y. *et al.* Over 16% efficiency organic photovoltaic cells enabled by a chlorinated acceptor with increased open-circuit voltages. *Nat. Commun.* **10**, 2515 (2019).

11. Qian, D. *et al.* Design rules for minimizing voltage losses in high-efficiency organic solar cells. *Nat. Mater.* **17**, 703–709 (2018).

12. Zhou, Z. *et al.* Subtle Molecular Tailoring Induces Significant Morphology Optimization Enabling over 16% Efficiency Organic Solar Cells with Efficient Charge Generation. *Adv. Mater.* **32**, 1906324 (2020).

13. Li, S., Li, C., Shi, M. & Chen, H. New Phase for Organic Solar Cell Research: Emergence of Y-Series Electron Acceptors and Their Perspectives. *ACS Energy Lett.* **5**, 1554–1567 (2020).

14. Yuan, J. *et al.* Reducing Voltage Losses in the A-DA′D-A Acceptor-Based Organic Solar Cells. *Chem* **6**, 2147–2161 (2020).

15. Vandewal, K., Mertens, S., Benduhn, J. & Liu, Q. The Cost of Converting Excitons into Free Charge Carriers in Organic Solar Cells. *J. Phys. Chem. Lett.* **11**, 129–135 (2020).

16. Geffroy, B., le Roy, P. & Prat, C. Organic light-emitting diode (OLED) technology: Materials, devices and display technologies. *Polym. Int.* **55**, 572–582 (2006).

17. Classen, A. *et al.* The role of exciton lifetime for charge generation in organic solar cells at negligible energy-level offsets. *Nat. Energy* **5**, 711–719 (2020).

18. Eisner, F. D. *et al.* Hybridization of Local Exciton and Charge-Transfer States Reduces Nonradiative Voltage Losses in Organic Solar Cells. *J. Am. Chem. Soc.* **141**, 6362–

6374 (2019).

19. Chen, X.-K., Coropceanu, V. & Brédas, J.-L. Assessing the nature of the charge-transfer electronic states in organic solar cells. *Nat. Commun.* **9**, 5295 (2018).

20. Wang, J., Chepelianskii, A., Gao, F. & Greenham, N. C. Control of exciton spin statistics through spin polarization in organic optoelectronic devices. *Nat. Commun.* **3**, 1191 (2012).

21. Chen, X.-K., Wang, T. & Brédas, J.-L. Suppressing Energy Loss due to Triplet Exciton Formation in Organic Solar Cells: The Role of Chemical Structures and Molecular Packing. *Adv. Energy Mater.* **7**, 1602713 (2017).

22. Rao, A. *et al.* The role of spin in the kinetic control of recombination in organic photovoltaics. *Nature* **500**, 435–439 (2013).

23. Kraffert, F. *et al.* Charge Separation in PCPDTBT:PCBM Blends from an EPR Perspective. *J. Phys. Chem. C* **118**, 28482–28493 (2014).

24. Köhler, A. & Beljonne, D. The Singlet–Triplet Exchange Energy in Conjugated Polymers. *Adv. Funct. Mater.* **14**, 11–18 (2004).

25. Hodgkiss, J. M. *et al.* Exciton-Charge Annihilation in Organic Semiconductor Films. *Adv. Funct. Mater.* **22**, 1567–1577 (2012).

26. Benduhn, J. *et al.* Impact of Triplet Excited States on the Open-Circuit Voltage of Organic Solar Cells. *Adv. Energy Mater.* **8**, 1800451 (2018).

27. Cohen, A. E. Nanomagnetic Control of Intersystem Crossing. *J. Phys. Chem. A* **113**, 11084–11092 (2009).

28. Shoaee, S. *et al.* Decoding Charge Recombination through Charge Generation in

Organic Solar Cells. *Sol. RRL* **3**, 1900184 (2019).

29. Dimitrov, S. D. *et al.* Polaron pair mediated triplet generation in polymer/fullerene blends. *Nat. Commun.* **6**, 6501 (2015).

30. Salvadori, E. *et al.* Ultra-fast spin-mixing in a diketopyrrolopyrrole monomer/fullerene blend charge transfer state. *J. Mater. Chem. A* **5**, 24335–24343 (2017).

31. Menke, S. M. *et al.* Limits for Recombination in a Low Energy Loss Organic Heterojunction. *ACS Nano* **10**, 10736–10744 (2016).

32. Xue, L. *et al.* Side Chain Engineering on Medium Bandgap Copolymers to Suppress Triplet Formation for High-Efficiency Polymer Solar Cells. *Adv. Mater.* **29**, 1703344 (2017).

33. Chow, P. C. Y., Gélinas, S., Rao, A. & Friend, R. H. Quantitative bimolecular recombination in organic photovoltaics through triplet exciton formation. *J. Am. Chem. Soc.* **136**, 3424–3429 (2014).

34. Di Nuzzo, D. *et al.* Improved Film Morphology Reduces Charge Carrier Recombination into the Triplet Excited State in a Small Bandgap Polymer-Fullerene Photovoltaic Cell. *Adv. Mater.* **22**, 4321–4324 (2010).

35. Karuthedath, S. *et al.* Buildup of Triplet-State Population in Operating TQ1:PC 71 BM Devices Does Not Limit Their Performance. *J. Phys. Chem. Lett.* **11**, 2838–2845 (2020).

36. Wang, R. *et al.* Charge Separation from an Intra-Moiety Intermediate State in the High-Performance PM6:Y6 Organic Photovoltaic Blend. *J. Am. Chem. Soc.* **142**, 12751–12759 (2020).

37. Gelinas, S. *et al.* Ultrafast Long-Range Charge Separation in Organic Semiconductor

Photovoltaic Diodes. *Science (80-.).* **343**, 512–516 (2014).

38. Jakowetz, A. C. *et al.* Visualizing excitations at buried heterojunctions in organic semiconductor blends. *Nat. Mater.* **16**, 551–557 (2017).

39. Menke, S. M. *et al.* Order enables efficient electron-hole separation at an organic heterojunction with a small energy loss. *Nat. Commun.* **9**, 277 (2018).

40. Burke, T. M., Sweetnam, S., Vandewal, K. & McGehee, M. D. Beyond Langevin Recombination: How Equilibrium Between Free Carriers and Charge Transfer States Determines the Open-Circuit Voltage of Organic Solar Cells. *Adv. Energy Mater.* **5**, 1500123 (2015).

41. Hosseini, S. M. *et al.* Putting Order into PM6:Y6 Solar Cells to Reduce the Langevin Recombination in 400 nm Thick Junction. *Sol. RRL* **4**, 2000498 (2020).

42. Karki, A. *et al.* Understanding the High Performance of over 15% Efficiency in Single-Junction Bulk Heterojunction Organic Solar Cells. *Adv. Mater.* **31**, 1903868 (2019).

43. Niklas, J. *et al.* Highly-efficient charge separation and polaron delocalization in polymer–fullerene bulk-heterojunctions: a comparative multi-frequency EPR and DFT study. *Phys. Chem. Chem. Phys.* **15**, 9562 (2013).

44. Richert, S., Tait, C. E. & Timmel, C. R. Delocalisation of photoexcited triplet states probed by transient EPR and hyperfine spectroscopy. *J. Magn. Reson.* **280**, 103–116 (2017).

45. Thomson, S. A. J. *et al.* Charge Separation and Triplet Exciton Formation Pathways in Small-Molecule Solar Cells as Studied by Time-Resolved EPR Spectroscopy. *J. Phys. Chem. C* **121**, 22707–22719 (2017).

671 46. Hintze, C., Steiner, U. E. & Drescher, M. Photoexcited Triplet State Kinetics Studied
672 by Electron Paramagnetic Resonance Spectroscopy. *ChemPhysChem* **18**, 6–16 (2017).

673 47. Benduhn, J. *et al.* Intrinsic non-radiative voltage losses in fullerene-based organic solar
674 cells. *Nat. Energy* **2**, 17053 (2017).

675 48. Kubas, A. *et al.* Electronic couplings for molecular charge transfer: benchmarking
676 CDFT, FODFT and FODFTB against high-level ab initio calculations. II. *Phys. Chem.*
677 *Chem. Phys.* **17**, 14342–14354 (2015).

678 49. Chang, W. *et al.* Spin-dependent charge transfer state design rules in organic
679 photovoltaics. *Nat. Commun.* **6**, 6415 (2015).

680 50. Street, R. A., Song, K. W., Northrup, J. E. & Cowan, S. Photoconductivity
681 measurements of the electronic structure of organic solar cells. *Phys. Rev. B* **83**,
682 165207 (2011).

683 51. Rasaiah, J. C., Hubbard, J. B., Rubin, R. J. & Lee, S. H. Kinetics of bimolecular
684 recombination processes with trapping. *J. Phys. Chem.* **94**, 652–662 (1990).

685 52. Lee, J. *et al.* Bandgap Narrowing in Non-Fullerene Acceptors: Single Atom
686 Substitution Leads to High Optoelectronic Response Beyond 1000 nm. *Adv. Energy*
687 *Mater.* **8**, 1801212 (2018).

688 53. de Mello, J. C., Wittmann, H. F. & Friend, R. H. An improved experimental
689 determination of external photoluminescence quantum efficiency. *Adv. Mater.* **9**, 230–
690 232 (1997).

691 54. Lee, C.-L., Yang, X. & Greenham, N. C. Determination of the triplet excited-state
692 absorption cross section in a polyfluorene by energy transfer from a phosphorescent
693 metal complex. *Phys. Rev. B* **76**, 245201 (2007).

55. Biskup, T. Structure–Function Relationship of Organic Semiconductors: Detailed Insights From Time-Resolved EPR Spectroscopy. *Front. Chem.* **7**, (2019).

56. Weber, S. Transient EPR. in *eMagRes* 255–270 (John Wiley & Sons, Ltd, 2017). doi:10.1002/9780470034590.emrstm1509

57. Niklas, J. & Poluektov, O. G. Charge Transfer Processes in OPV Materials as Revealed by EPR Spectroscopy. *Adv. Energy Mater.* **7**, 1602226 (2017).

58. Righetto, M. *et al.* Engineering interactions in QDs–PCBM blends: a surface chemistry approach. *Nanoscale* **10**, 11913–11922 (2018).

59. Franco, L. *et al.* Time-Resolved EPR of Photoinduced Excited States in a Semiconducting Polymer/PCBM Blend. *J. Phys. Chem. C* **117**, 1554–1560 (2013).

60. Buckley, C. D., Hunter, D. A., Hore, P. J. & McLauchlan, K. A. Electron spin resonance of spin-correlated radical pairs. *Chem. Phys. Lett.* **135**, 307–312 (1987).

61. Hore, P. J., Hunter, D. A., McKie, C. D. & Hoff, A. J. Electron paramagnetic resonance of spin-correlated radical pairs in photosynthetic reactions. *Chem. Phys. Lett.* **137**, 495–500 (1987).

62. Biskup, T. Structure–Function Relationship of Organic Semiconductors: Detailed Insights From Time-Resolved EPR Spectroscopy. *Front. Chem.* **7**, 1–22 (2019).

63. Stoll, S. & Schweiger, A. EasySpin, a comprehensive software package for spectral simulation and analysis in EPR. *J. Magn. Reson.* **178**, 42–55 (2006).

Figure Legends

Figure 1: The triplet formation pathways and organic solar cell materials investigated in this study. (a) A diagram to illustrate the geminate pathway for T_1 formation in OSCs. After optical excitation (1), charge transfer from the S_1 to ^{1}CTE occurs (2). However, the ^{1}CTE does not manage to separate into FC before spin-mixing with the ^{3}CTE occurs on ns timescales (3). From the ^{3}CTE, BCT to a lower energy T_1 on either the D or A can occur. **(b)** A diagram to illustrate the non-geminate pathway for T_1 formation in OSCs. After optical excitation (1), charge transfer from the S_1 to ^{1}CTE occurs (2). The ^{1}CTE then successfully dissociates in FC (4). The FC then undergo non-geminate recombination, forming a 3:1 ratio of ^{3}CTE to ^{1}CTE (5). From the ^{3}CTE, BCT to a lower energy T_1 on either the D or A can occur. **(c)** The molecular structures of the four polymer donors and seven NFA materials used in this study.

Table 1: A summary of the key parameters for the OSC blends investigated in this study. Φ_{PL} was measured for a neat film of the NFA used in the blend. The error in the Φ_{PL} is ±0.1%. *Φ_{PL} of SiOTIC-4F was too low to be measured and is therefore quoted as less than the smallest value reliably resolvable on our setup (0.1%). For the determination of ΔV_{nr}, the EQE_{EL} at 293 K was taken at $-J_{SC}$ to ensure that carrier densities were relevant to device operating conditions. Additionally, it is stated whether the blend forms triplet excitons resulting from either geminate or non-geminate recombination pathways.

Figure 2: Spectroscopic investigations of triplet formation in model non-fullerene acceptor blends. (a) The IR region TA spectra of the PM6:Y6 blend (293 K), excited with a moderate fluence of 5.4 μJ cm^{-2} at 532 nm for preferential PM6 excitation. The Y6 T_1 PIA forms at 1450 nm, as confirmed by triplet sensitisation experiments. **(b)** The normalised TA

kinetics of the PM6:Y6 blend, taken around the maximum of the Y6 T_1 feature between 1425 – 1475 nm. The clear fluence dependence of T_1 formation is indicative of a bimolecular generation pathway. **(c)** The trEPR spectra of the PM6:Y6 blend (80 K) after excitation at 532 nm, taken at 1 and 5 μs. The inset shows a magnification and simulation of the weak ISC triplet signal. The field positions of the absorption (*a*) and emission (*e*) EPR transitions of the ISC triplet are overlaid on the plot for clarity. **(d)** The IR region TA spectra of the PTB7-Th:IEICO-2F blend (293 K), excited with a moderate fluence of 3.8 μJ cm^{-2} at 620 nm for preferential PTB7-Th excitation. The IEICO-2F T_1 PIA at 1350 nm does not form in the blend. **(e)** The normalised TA kinetics of the PTB7-Th:IEICO-2F blend, taken around the maximum of the IEICO-2F T_1 PIA at 1350 – 1370 nm. No fluence dependence in the IEICO-2F T_1 region is observed. **(f)** The trEPR spectra of the PTB7-Th:IEICO-2F blend (80 K) after excitation at 532 nm, taken at 1 and 5 μs. The field positions of the absorption (*a*) and emission (*e*) EPR transitions of the ISC triplet are overlaid on the plot for clarity.

Figure 3: The role of hybridisation in organic solar cell blends. (a) The results of a rigid scan of the ^{1}CTE and ^{3}CTE energies for a representative PTB7-Th:IEICO-2F supramolecular configuration as a function of D:A separation. At each D:A separation, k_{BCT} from ^{3}CTE to T_1 of the NFA has also been calculated. The solid lines provide polynomial guides to the eye. **(b)** The results of a rigid scan of the ^{1}CTE and ^{3}CTE energies for a representative PM6:Y6 supramolecular configuration. At each D:A separation, k_{BCT} from ^{3}CTE to T_1 of the NFA has also been calculated. The solid lines provide polynomial guides to the eye. **(c)** A schematic to represent the effect of CTE-LE hybridisation on the energetic ordering of the ^{1}CTE and ^{3}CTE. **(d)** An image showing the same optimised supramolecular configuration between PTB7-Th (beige) IEICO-2F (purple) used for the calculations in Fig. 3a. The lobes represent regions of constructive overlap between the highest-occupied molecular orbitals (HOMOs) of D and A.

765 The HOMO overlap that controls the size of the electronic coupling and thus mediates
766 hybridisation between the NFA LE and the CTEs; for hybridisation between the LE states of
767 the D polymer and the CTEs, the lowest occupied molecular orbital overlap is the relevant
768 interaction.
769

Supplementary Information for

The role of charge recombination to triplet excitons in organic solar cells

Alexander J. Gillett[1], Alberto Privitera[2], Rishat Dilmurat[3], Akchheta Karki[4], Deping Qian[5], Anton Pershin[3,6], Giacomo Londi[3], William K. Myers[7], Jaewon Lee[4,8], Jun Yuan[5,9], Seo-Jin Ko[4,10], Moritz K. Riede[2], Feng Gao[5], Guillermo C. Bazan[4], Akshay Rao[1], Thuc-Quyen Nguyen[4]*, David Beljonne[3]* and Richard H. Friend[1]*.*

[1]Cavendish Laboratory, University of Cambridge, JJ Thomson Avenue, Cambridge, CB3 0HE, UK.

[2]Clarendon Laboratory, University of Oxford, Parks Road, Oxford, OX1 3PU, UK.

[3]Laboratory for Chemistry of Novel Materials, Université de Mons, Place du Parc 20, 7000 Mons, Belgium.

[4]Centre for Polymers and Organic Solids, Department of Chemistry and Biochemistry, University of California at Santa Barbara, CA 93106, USA.

[5]Department of Physics, Chemistry and Biology (IFM), Linköping University, Linköping, 58183, Sweden.

[6]Wigner Research Centre for Physics, PO Box 49, H-1525, Budapest, Hungary.

[7]Centre for Advanced ESR, Inorganic Chemistry Laboratory, University of Oxford, South Parks Road, Oxford, OX1 3QR, UK.

[8]Department of Chemical Engineering and Applied Chemistry, Chungnam National University, 99, Daehak-ro, Yuseong-gu, Daejeon, 34134, Republic of Korea.

[9]College of Chemistry and Chemical Engineering, Central South University, Changsha, 410083, P.R. China.

[10]Division of Advanced Materials, Korea Research Institute of Chemical Technology, Daejeon 34114, Republic of Korea.

*Corresponding authors: Alexander J. Gillett: E-mail: ajg216@cam.ac.uk; Thuc-Quyen Nguyen: E-mail: quyen@chem.ucsb.edu; David Beljonne: E-mail: david.beljonne@umons.ac.be; Richard H. Friend: E-mail: rhf10@cam.ac.uk.

Table of Contents

Material properties **3**
Absorption spectra 3
Energy levels 4
OSC device performance **5**
J-V curves 5
EQE_{EL} curves 6
Transient absorption **7**
Triplet sensitization experiments 7
TA of neat materials 8
TA of OSC blends 11
Electro-absorption analysis of NFA blends to determine $k_{dissociation}$ 31
Investigation of fast ISC in IEICO derivatives 38
Quantifying T_1 formation from TA **40**
Transient EPR **51**
trEPR theory 51
Partial preferential order of triplet states 53
The impact of temperature on the trEPR results 54
trEPR experimental details 54
trEPR simulation procedure 56
trEPR results summary 57
trEPR simulation summary table 60
Full trEPR results and discussion 63
Full 2D trEPR spectra 87
***E_g and E_{CT}* determination for NFA blends** **91**
Quantum chemical calculations **93**
TD-DFT calculation details 93
Back charge transfer rate calculations 95
Singlet and triplet CTE-LE hybridisation 98
Bibliography **105**

Material properties

Absorption spectra

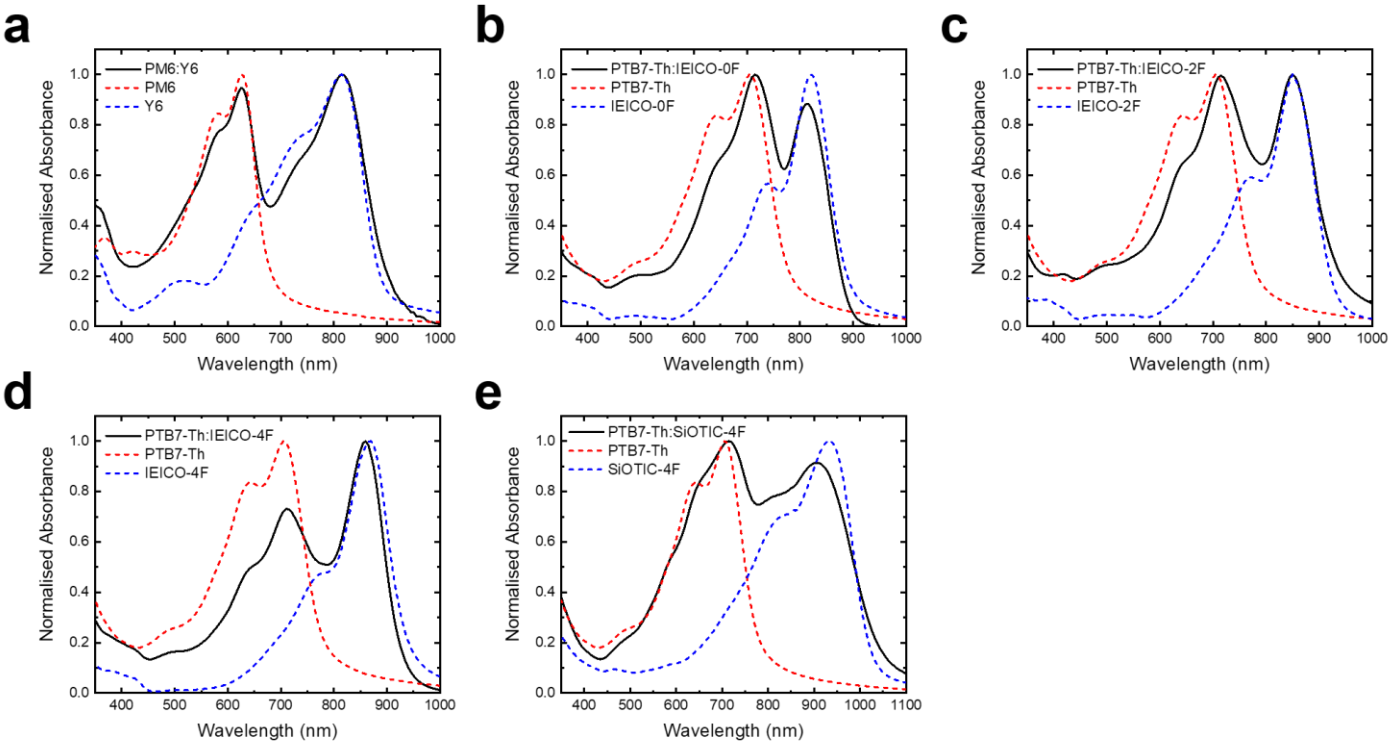

Figure S1: The normalised absorption spectra of the key blends examined in this study. The normalised absorption spectra of the neat materials are also overlaid for reference.

Energy levels

Material	HOMO (ev)	LUMO (ev)
PM6	-5.56	-3.50
PTB7-Th	-5.20	-3.46
PBDB-T	-5.33	-3.29
J51	-5.29	-3.30
Y6	-5.65	-4.10
ITIC	-5.60	-3.85
IT-4F	-5.71	-4.15
IEICO-0F	-5.24	-3.80
IEICO-2F	-5.34	-4.10
IEICO-4F	-5.44	-4.25
SiOTIC-4F	-5.28	-4.12

Table S1: The tabulated highest occupied molecular orbital (HOMO) and lowest unoccupied molecular orbital (LUMO) energy levels of the materials used in this study, as determined by cyclic voltammetry.

OSC device performance

J-V curves

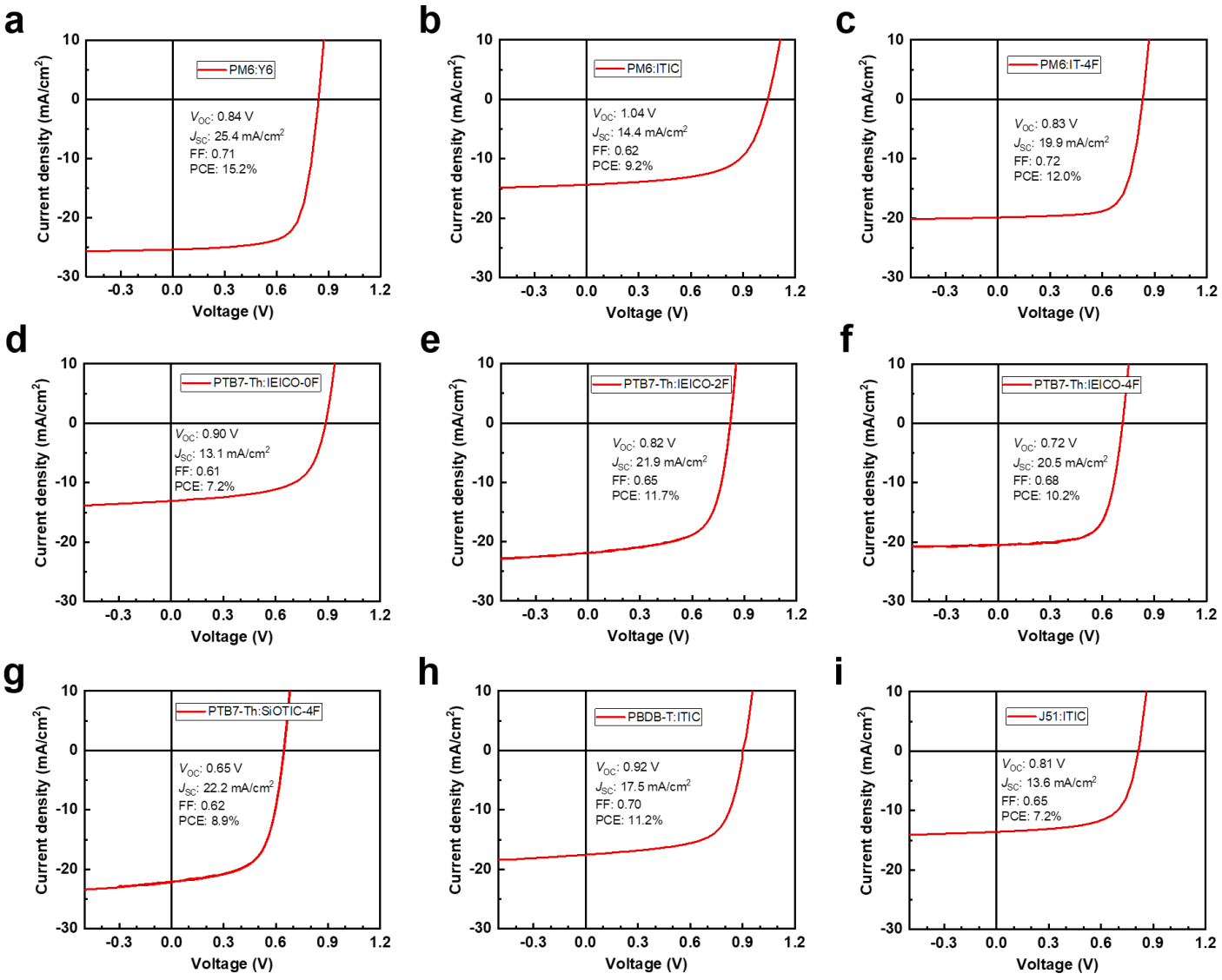

Figure S2: The current density-voltage (JV) curves of the OSCs investigated in this study.

EQE_{EL} curves

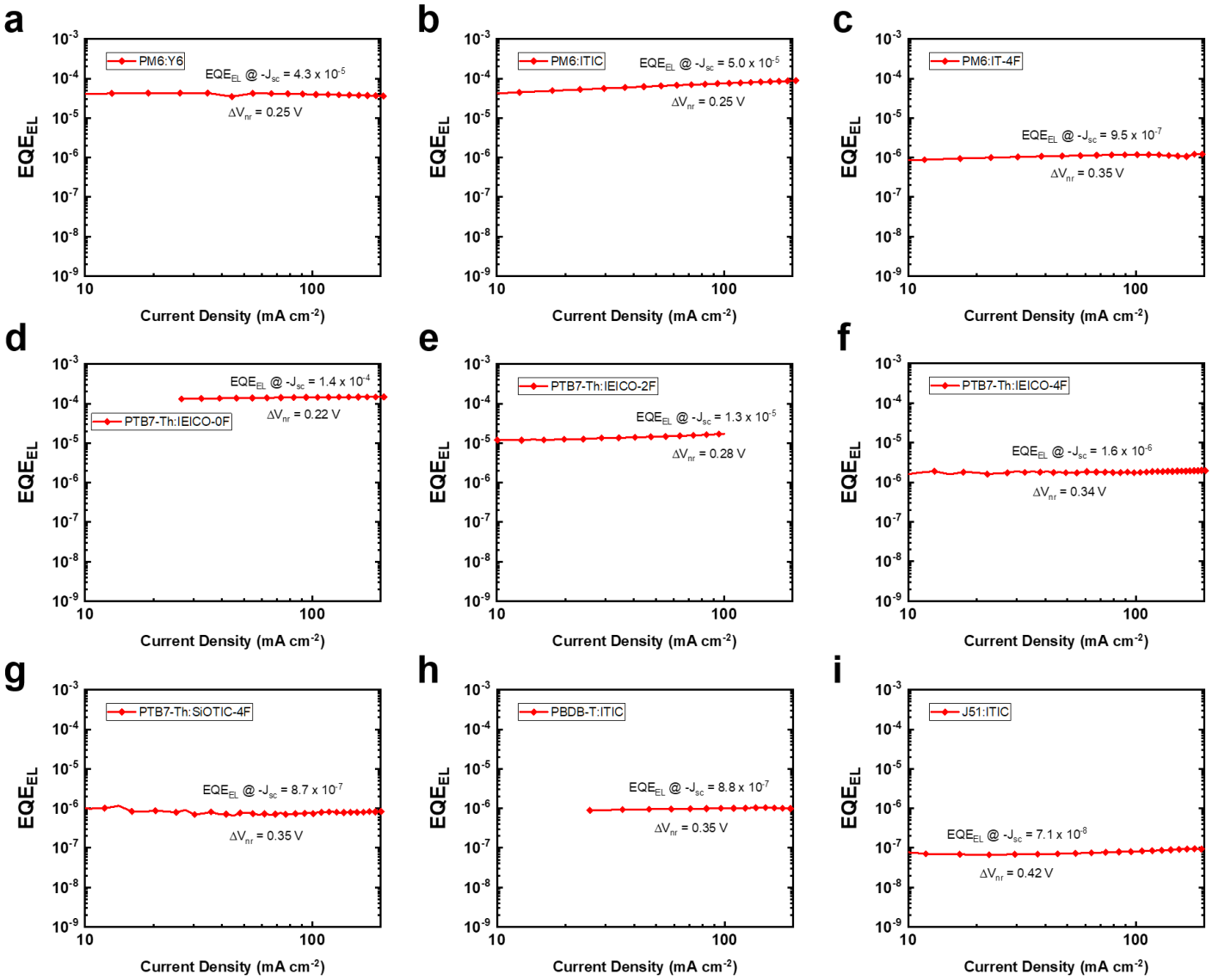

Figure S3: The electroluminescence external quantum efficiency (EQE_{EL}) of the OSCs investigated in this study.

Transient absorption

Triplet sensitisation measurements

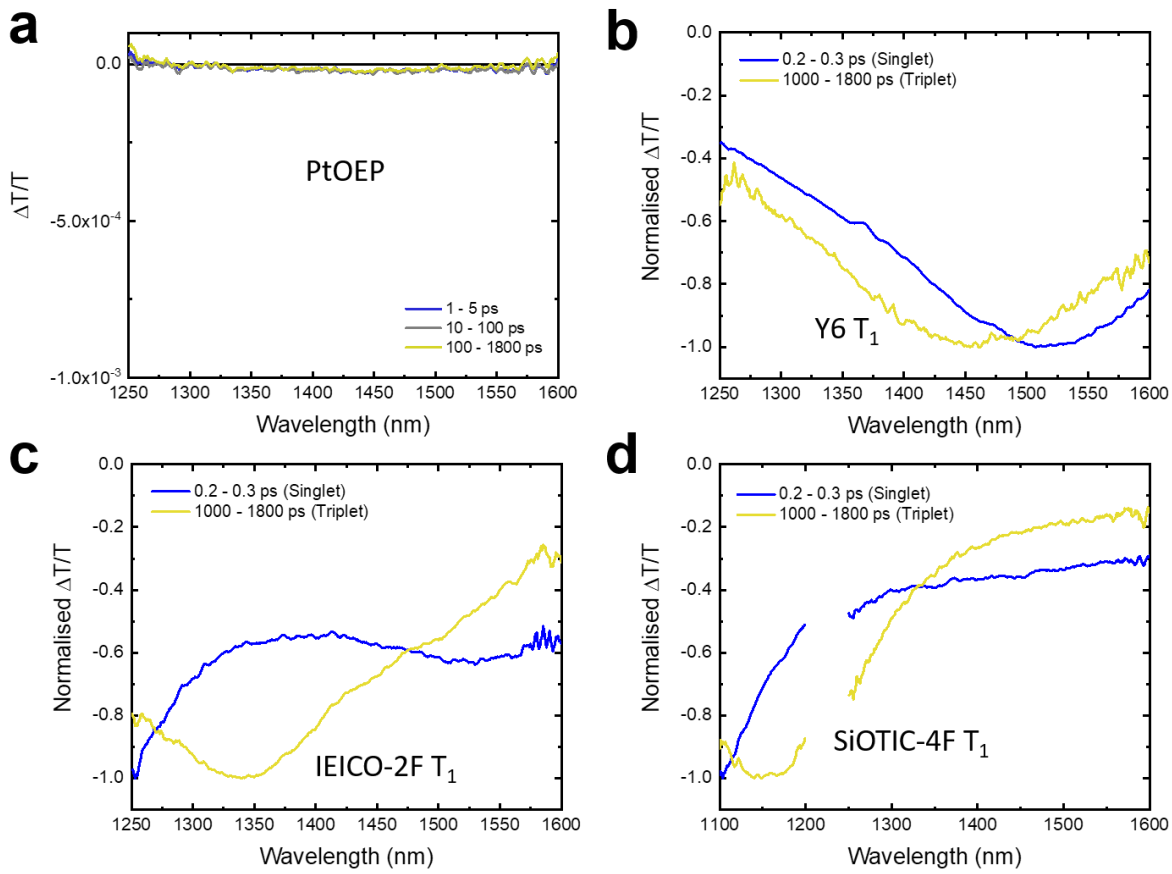

Figure S4: Triplet sensitisation experiments of the non-fullerene acceptors (NFA) used in this study. PtOEP was used as the triplet sensitizer. Dilute blends comprised of polystyrene (PS):PtOEP:NFA 0.94:0.03:0.03 were used to ensure that intersystem crossing (ISC) could occur on PtOEP, followed by triplet energy transfer to the NFA, before charge transfer to the NFA. All films were excited at 532 nm for preferential PtOEP excitation, though some unavoidable excitation of the NFA occurred in all blends, as evidenced by the presence of the singlet (S_1) PIAs at 0.2 – 0.3 ps. By 1000 – 1800 ps, triplet energy transfer from PtOEP to the NFA had taken place, leaving behind a long-lived photo-induced absorption (PIA), belonging to the T_1 of the NFA. **(a)** The TA spectra of a PS:PtOEP 0.94:0.06 film. There are no significant PtOEP PIA features in the IR region probed, confirming that any new PIAs in this region must belong to excited states on the NFAs. **(b)** The TA spectra of a PS:PtOEP:Y6 0.94:0.03:0.03 film. A new PIA belonging to the Y6 T_1 is peaked at 1450 nm. **(c)** The TA spectra of a

PS:PtOEP:IEICO-2F 0.94:0.03:0.03 film. A new PIA belonging to the IEICO-2F T_1 is peaked at 1350 nm. **(d)** The TA spectra of a PS:PtOEP:SiOTIC-4F 0.94:0.03:0.03 film. A new PIA belonging to the SiOTIC-4F T_1 is peaked at 1150 nm. For ITIC and IT-4F, we note that previous works have already reported in detail the sensitisation of ITIC derivatives by PtOEP[1], confirming that the T_1 PIA of ITIC derivatives is peaked at 1220 nm.

TA of neat materials

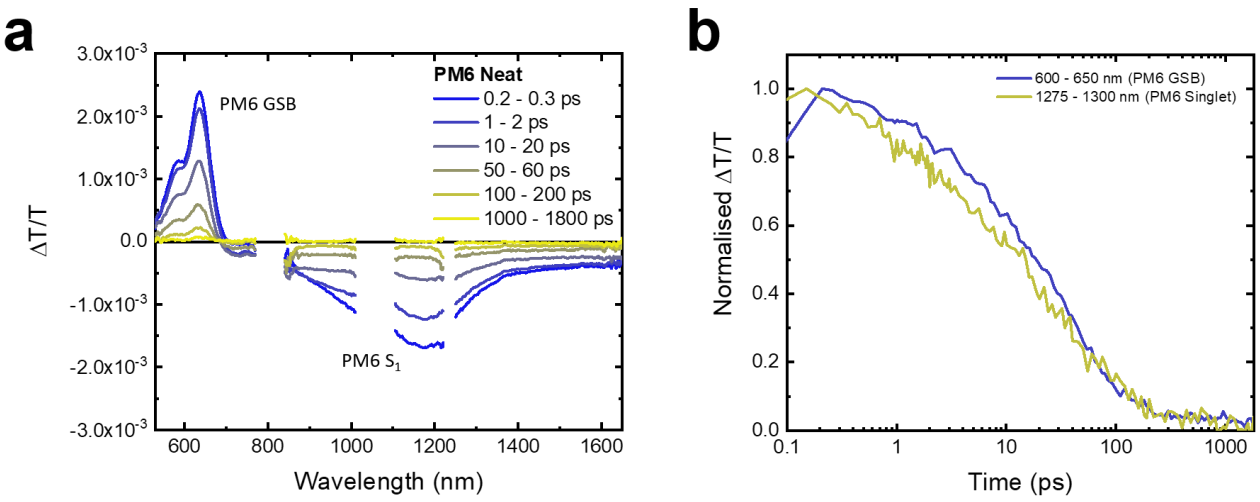

Figure S5: (a) The TA spectra of a neat PM6 film, excited at 532 nm with a fluence of 3.1 μJ cm^{-2}. The PM6 ground state bleach (GSB) is visible between 530 – 670 nm. The PM6 S_1 PIA is broad and spans the near infrared (NIR) region, peaked at 1150 nm. **(b)** The kinetics of the PM6 GSB and S_1 regions. As expected, the decay of the GSB and S_1 mirror each other, with most excited states decayed after a few hundred ps.

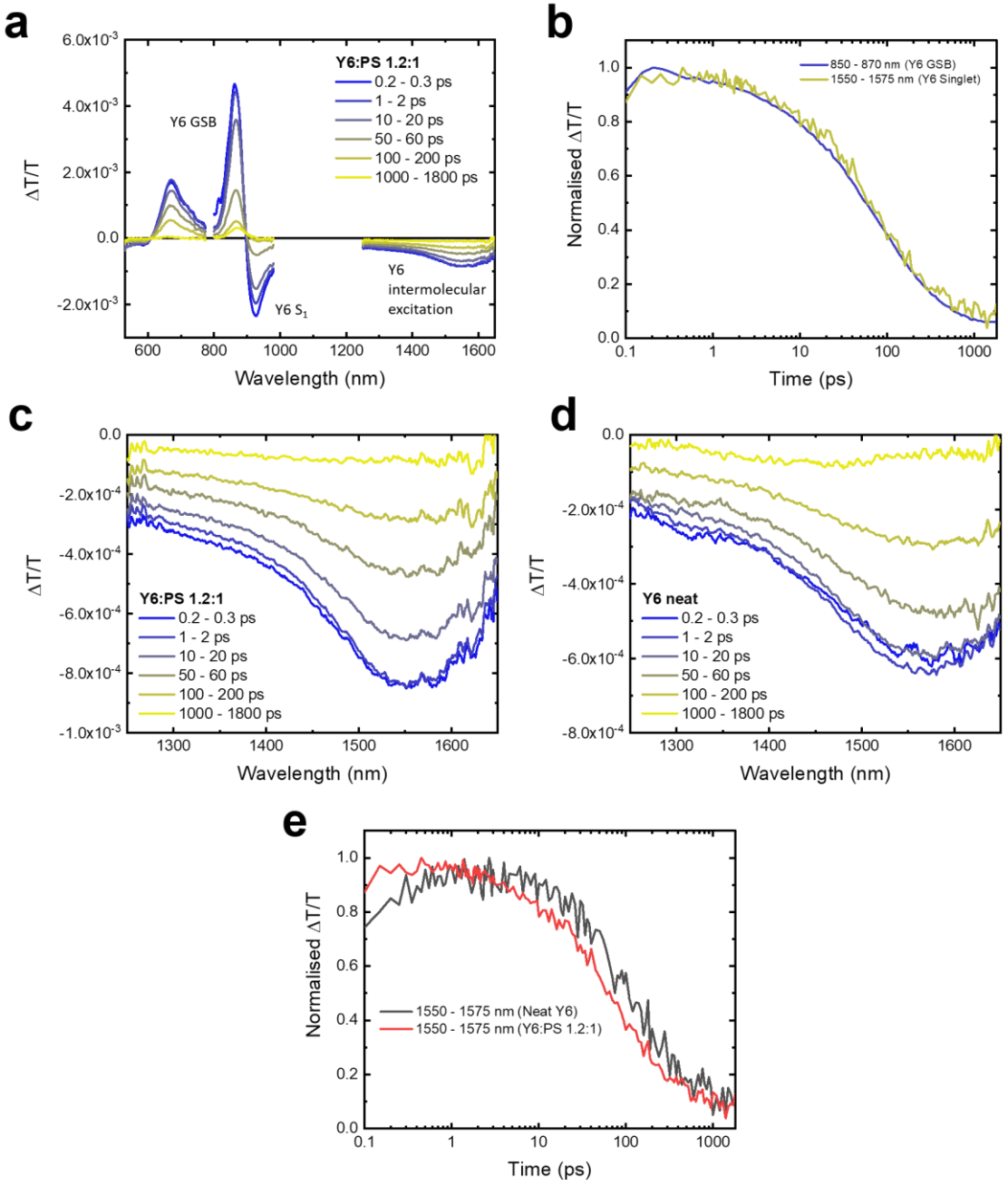

Figure S6: (a) The TA spectra of a Y6:PS 1.2:1 film, excited at 800 nm with a fluence of 1.8 μJ cm^{-2}. The Y6 GSB is visible between 600 – 900 nm, with two distinct vibronic peaks. There are two Y6 PIAs in the NIR region: one sharp peak adjacent to the Y6 GSB at 910 nm and a weaker, broad feature peaked at 1550 nm. The former is assigned to the S_1 of Y6 and the latter an intermolecular excitation (inter-CT) between neighbouring Y6 molecules[2]. **(b)** The kinetics of the Y6 GSB and inter-CT regions. **(c)** The IR probe region (1250 – 1650 nm) of the Y6:PS 1.2:1 film. **(d)** The IR probe region (1250 – 1650 nm) of a neat Y6 film for comparison. Both the neat and PS blend films have quantitatively the same spectral features, meaning that it is appropriate to use the Y6:PS blend for assignment of Y6 spectral features. **(e)** A comparison between the kinetics from the inter-CT PIA in neat Y6 and the Y6:PS 1.2:1 film.

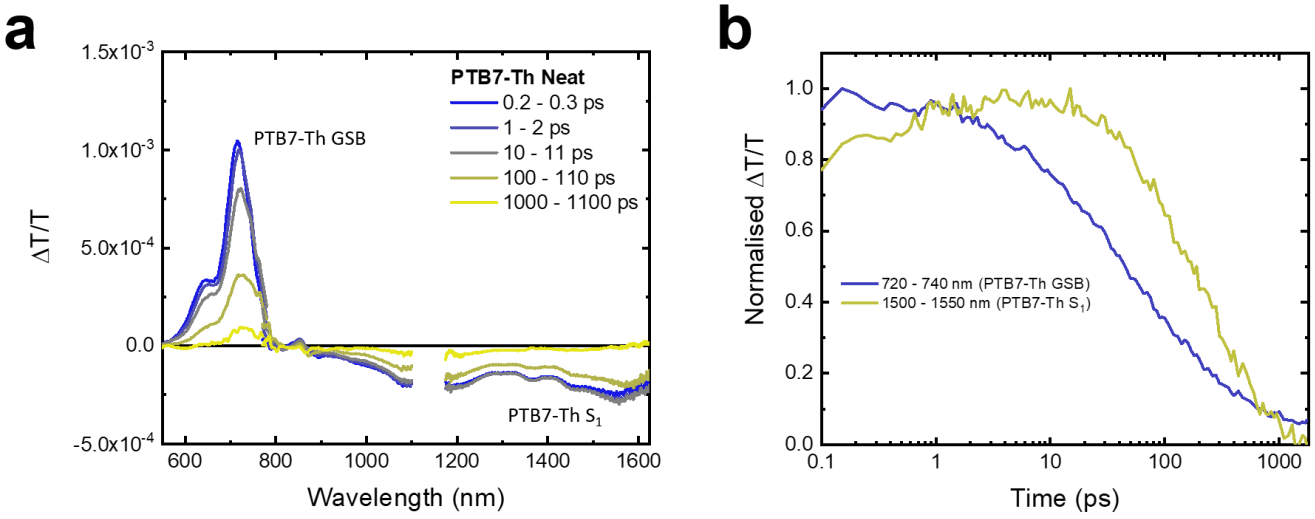

Figure S7: (a) The TA spectra of a neat PTB7-Th film, excited at 620 nm with a fluence of 2.1 μJ cm^{-2}. The PTB7-Th GSB is visible between 600 – 770 nm, with two distinct vibronic peaks. There are two PTB7-Th S_1 PIAs in the NIR region: one at 1150 nm and the other at 1550 nm. **(b)** The kinetics of the PTB7-Th GSB and S_1 regions. Interestingly, the GSB appears to decay more quickly than the S_1 PIA. The reasons for this are unclear and beyond the scope of this work, where we are simply interested in the spectral features of PTB7-Th.

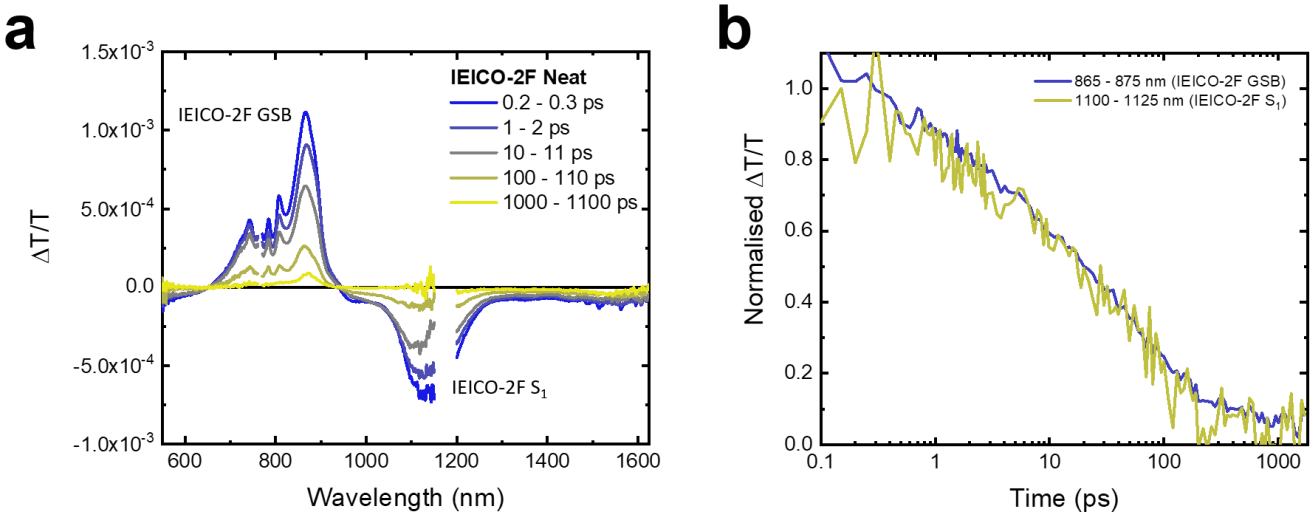

Figure S8: (a) The TA spectra of a neat IEICO-2F film, excited at 850 nm with a fluence of 2.1 μJ cm^{-2}. The IEICO-2F GSB is visible between 650 – 900 nm, with two distinct vibronic peaks. A singlet IEICO-2F S_1 PIAs in apparent in the NIR region, peaked at 1120 nm. **(b)** The kinetics of the IEICO-2F GSB and S_1 regions. As expected, the decay of the GSB and S_1 mirror each other, with most excited states decayed after a few hundred ps.

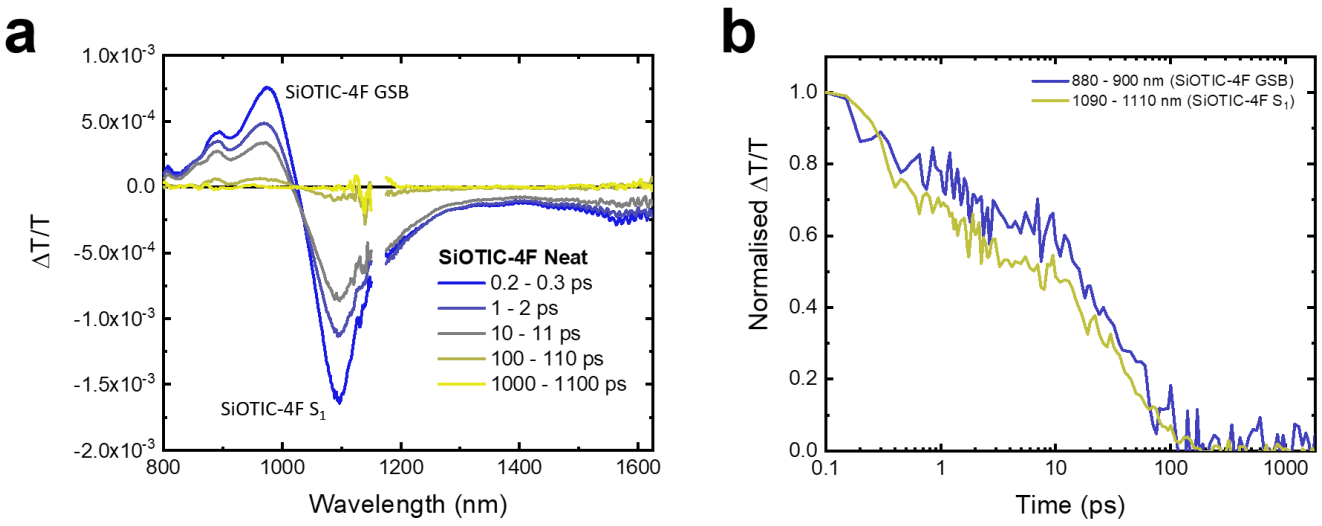

Figure S9: (a) The TA spectra of a neat SiOTIC-4F film, excited at 975 nm with a fluence of 3.8 μJ cm^{-2}. The PTB7-Th GSB is visible between 800 – 1030 nm, with two distinct vibronic peaks. There are two SiOTIC-4F S_1 PIAs in the NIR region: an intense peak at 1090 nm and weak band at 1550 nm. **(b)** The kinetics of the SiOTIC-4F GSB and S_1 regions. Interestingly, the GSB appears to decay more quickly than the S_1 PIA. As expected, the decay of the GSB and S_1 mirror each other, with most excited states decayed after 100 ps.

TA of OSC blends

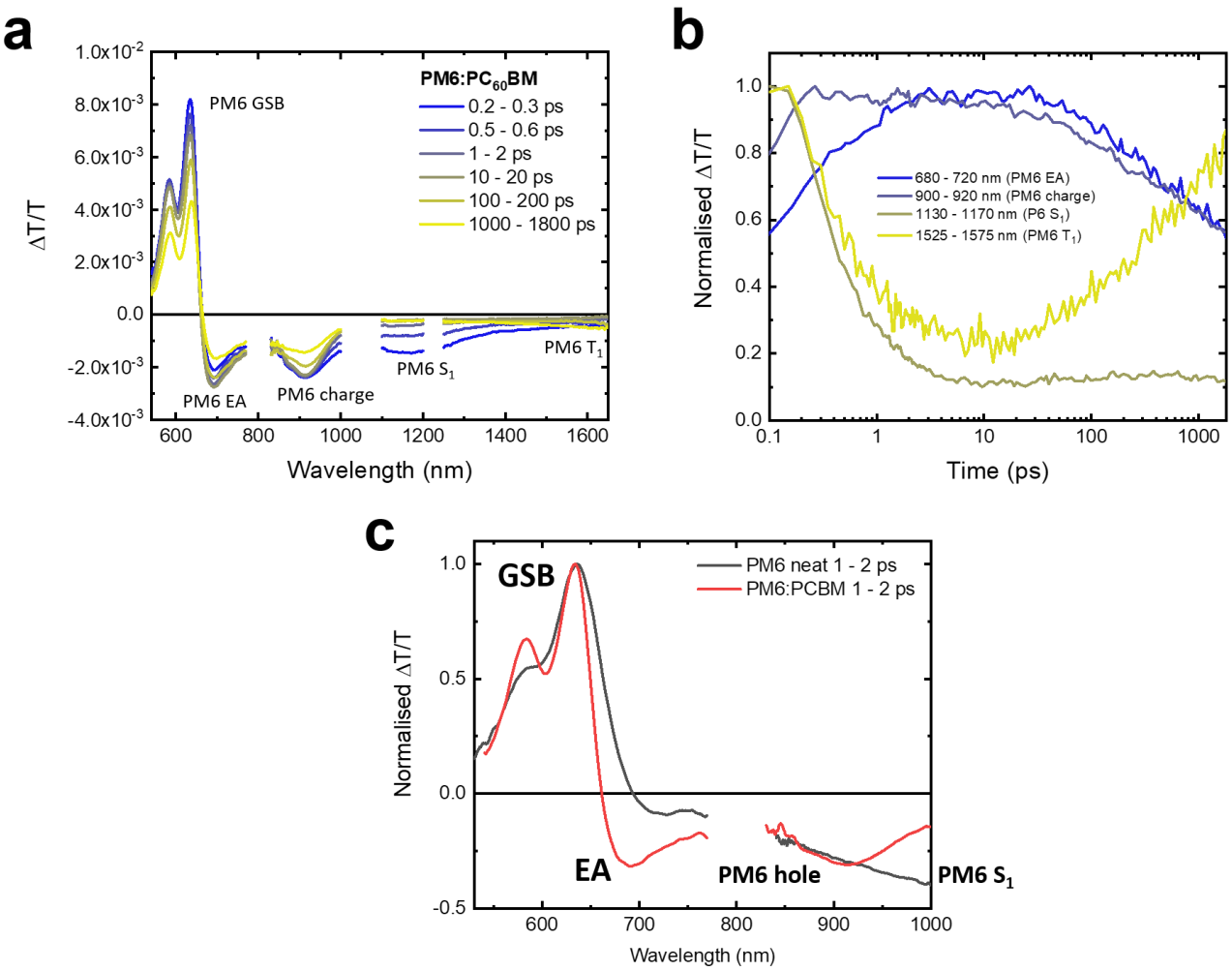

Figure S10: The TA spectra of a PM6:$PC_{60}BM$ film, excited at 532 nm with a fluence of 5.1 μJ cm^{-2}. The purpose of this experiment is to identify features associated with the PM6 after electron transfer to $PC_{60}BM$. As well as the PM6 GSB between 540 – 650 nm and the S_1 at 1150 nm, we also notice negative features present at 690 and 920 nm, which are not present in the neat PM6 film. The feature at 920 nm is peaked almost immediately, indicating it is the PM6 hole PIA formed after ultrafast electron transfer to $PC_{60}BM$. Ultrafast electron transfer is confirmed from the loss of the PM6 S_1 PIA within a few ps. Interestingly, the feature at 690 nm takes until 3 ps to reach its maximum intensity. Because of this time evolution and the spectral position right at the absorption edge of PM6, we assign this band to the electro-absorption (EA) of PM6: this represents the Stark-shift of the PM6 absorption spectrum by the electric field of the separating charges[3]. The maximum EA intensity is reached when the CT states have dissociated into free charges (FC)[3–6]. Thus, tracking the EA response provides an insight into the charge separation process. At longer times, a new PIA band at 1600 nm begins to grow in. We note that this is associated with the loss of the PM6 charge PIA. Thus, we assign this new band to the PM6 T_1.

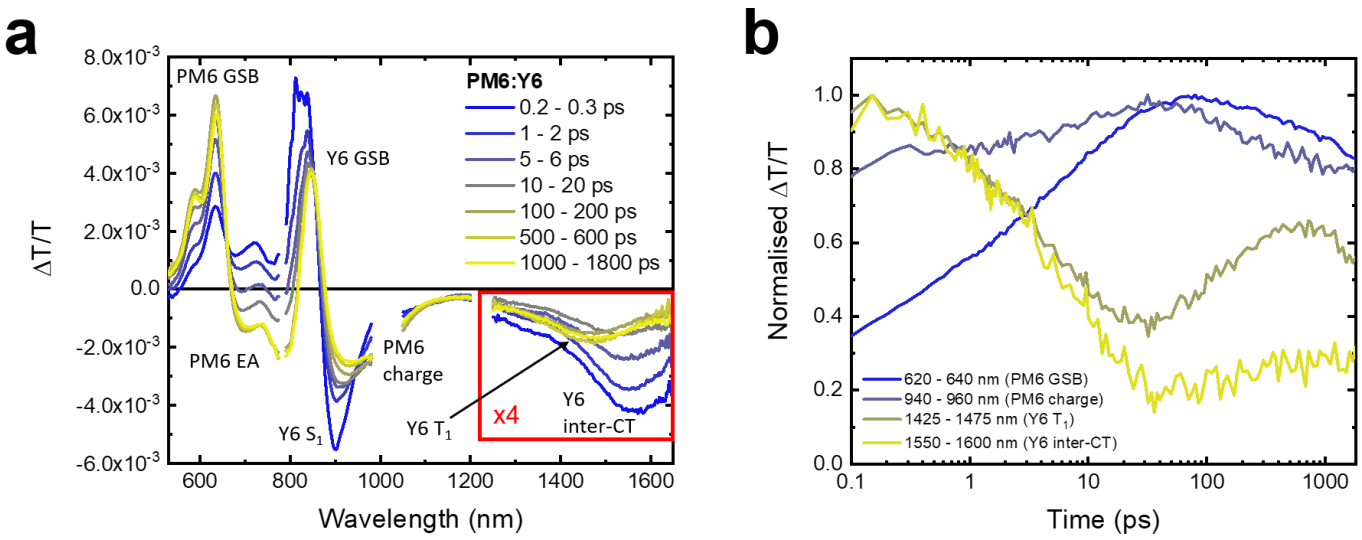

Figure S11: (a) The TA spectra of a PM6:Y6 film, pumped at 800 nm for selective Y6 excitation with a moderate fluence of 3.0 μJ cm^{-2}. At early times, features associated with Y6, including the GSB at 840 nm, S_1 PIA at 900 nm, and the Y6 intermolecular excitation (inter-CT) at 1550 nm can be seen. Additionally, the PM6 GSB is already present by 200 fs, suggesting that some of the hole transfer in this blend can occur on ultrafast timescales. As time progresses, the PM6 GSB grows more intense and the Y6 S_1 PIAs are lost, indicating that additional hole transfer is occurring. We also notice new negative bands forming at 750 and 930 nm on the same timescales. Fig. S9 allows for the assignment of the band around 750 nm to the EA of PM6 and the PIA at 930 nm to charges on PM6. After 50 – 100 ps, the PM6 GSB and PM6 charge PIA begin to decrease in intensity, with a new PIA at 1450 nm forming. From triplet sensitisation measurements with PtOEP (Fig. S4b), we know this is the Y6 T_1 PIA. Therefore, it is clear that the loss of charges is associated with the formation of T_1 on Y6. **(b)** The kinetics of the PM6:Y6 film in relevant spectral regions. To clarify the discussion of the spectra, we clearly see the growth of the PM6 GSB and charge PIA on ps timescales, followed by their fall from ~50 ps onwards. The kinetic of the Y6 T_1 region exhibits an obvious growth on the same timescales the PM6 GSB and charge PIAs are lost.

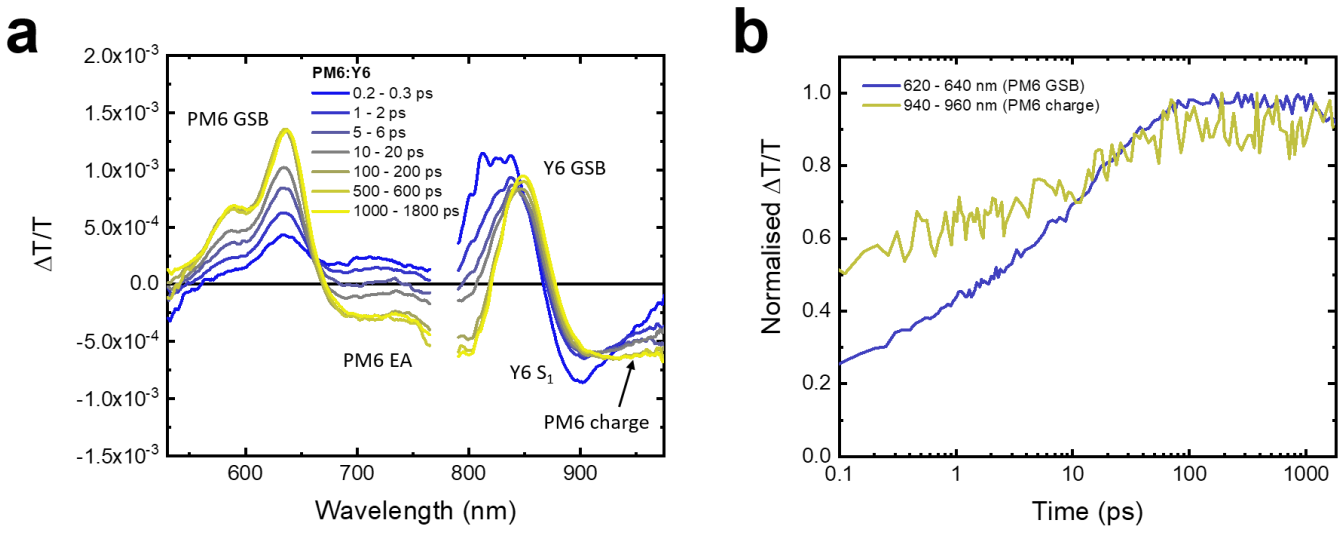

Figure S12: (a) The TA spectra of a PM6:Y6 film, pumped at 800 nm for selective Y6 excitation. A very low fluence of 0.5 μJ cm^{-2} was used to minimise any non-geminate recombination processes on the timescales of the experiment. The evolution of the TA spectra with time follows the same path as the previous discussions in Fig. S11. **(b)** The kinetics of the PM6 GSB and charge PIA regions. An increase in intensity of these features indicates that hole transfer from Y6 to PM6 is occurring. By 100 ps, there is no further change in magnitude of the signal in these regions, signifying hole transfer has been completed. Importantly, there is no decrease in intensity of the GSB or PIA on the timescales of the TA up to 1.8 ns. This confirms that there is no excess non-geminate recombination taking place, meaning our assertion that hole transfer is completed by 100 ps is accurate. Additionally, the lack of excited state decay by 1.8 ns also suggests that geminate recombination is not a significant loss pathway, as this form of recombination is expected to be fluence-independent and typically takes place on timescales <2 ns[5,7].

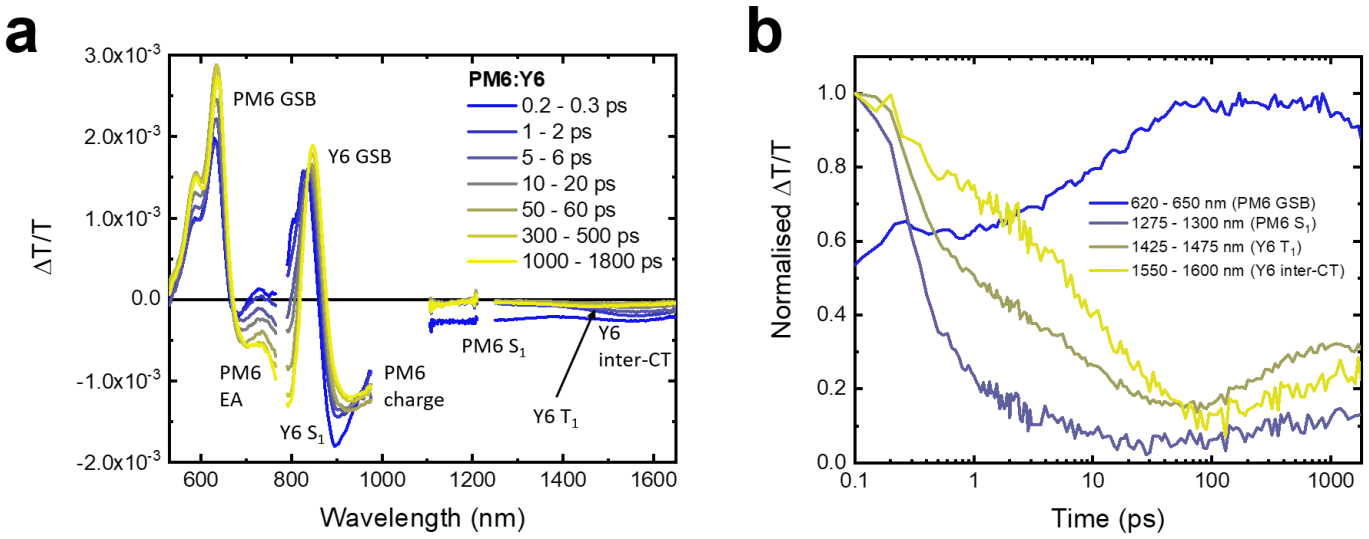

Figure S13: (a) The TA spectra of a PM6:Y6 film, pumped at 532 nm for preferential PM6 excitation with a low fluence of 1.8 μJ cm^{-2}. At the earliest times, the PM6 S_1 around 1150 nm is already heavily quenched and has largely disappeared by 1 ps. This confirms that the electron transfer in this blend takes place on ultrafast timescales, comparable to that of polymer:fullerene blends. From 1 ps onwards, the behaviour mimics that of the PM6:Y6 film excited at 800 nm for selective Y6 excitation. We note that whilst PM6 is preferentially excited at 532 nm, some inadvertent excitation of Y6 also occurs. This is evidenced by the presence at 0.2 ps of the Y6 S_1 PIA at 900 nm and inter-CT PIA at 1550 nm. These Y6 excitons then follow the previously observed hole transfer dynamics from Fig. S12. Additionally, the Y6 T_1 PIA is noticeable on the timescales of 100's ps, formed by back charge transfer (BCT) from the triplet charge transfer state (^{3}CT). **(b)** The kinetics of the PM6:Y6 film in relevant spectral regions. Immediately obvious is the rapid rate at which the PM6 S_1 PIA decays, confirming the presence of ultrafast electron transfer. Additionally, the PM6 GSB region clearly grows towards 100 ps, consistent with the timescale of the previously-observed hole transfer (Fig. S12).

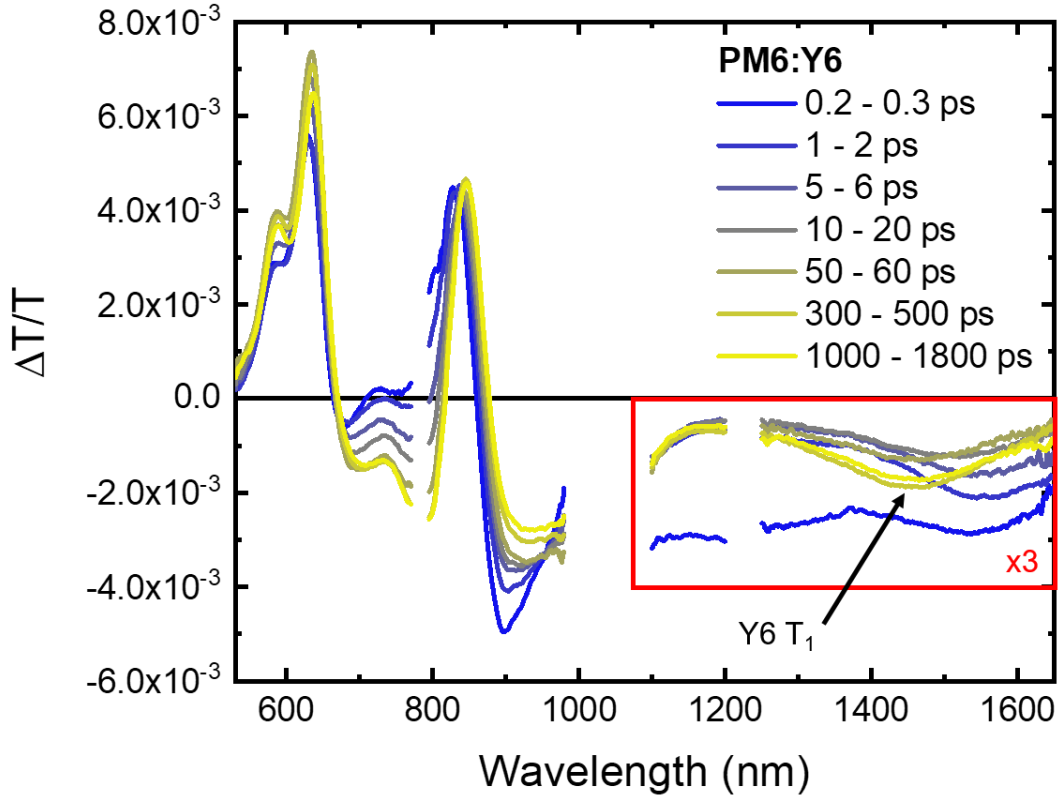

Figure S14: The full TA spectra of Fig. 2a: a PM6:Y6 film, pumped at 532 nm for preferential PM6 excitation with a moderate fluence of 5.4 μJ cm^{-2}. The rise of the Y6 T_1 PIA at 1450 nm is clearly correlated with the decrease in the PM6 charge PIA around 950 nm.

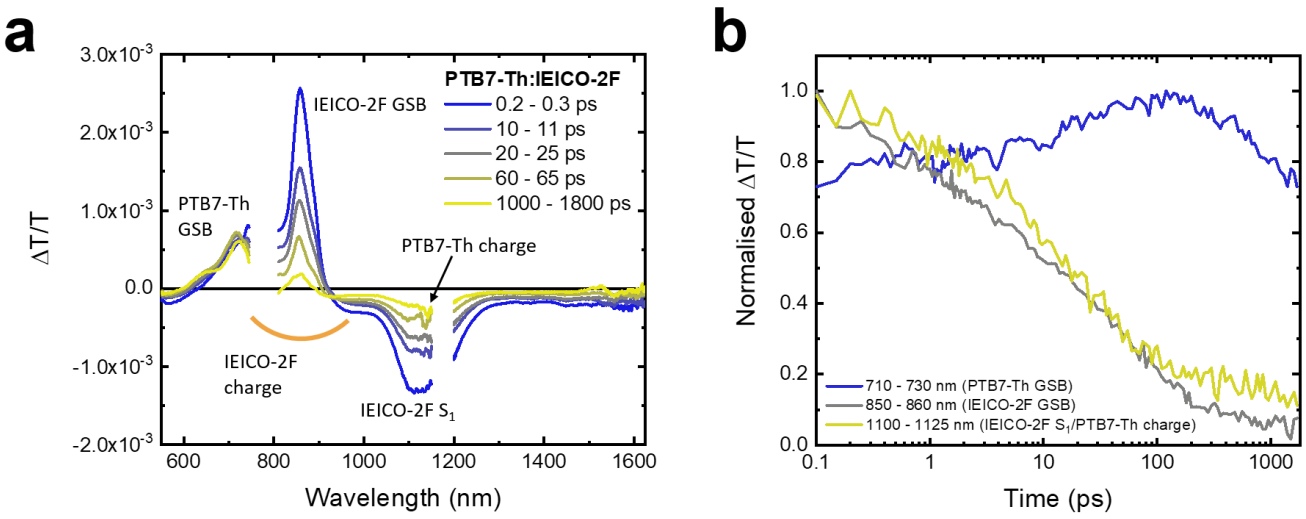

Figure S15: (a) The TA spectra of a PTB7-Th:IEICO-2F film, pumped at 850 nm for selective IEICO-2F excitation with a low fluence of 2.1 μJ cm^{-2}. At the earliest times, the spectrum resembles that of the neat IEICO-2F film, with the IEICO-2F GSB and S_1 PIA visible between 600 – 920 nm and at 1120 nm, respectively. As time progresses, we begin to notice the PTB7-Th GSB appearing, with a characteristic vibronic peak at 650 nm. This is the result of hole transfer from IEICO-2F. Interestingly, the IEICO-2F GSB also falls rapidly on the timescales of hole transfer. Furthermore, there is only a muted increase in the intensity of the PTB7-Th GSB region. This is unusual as if hole transfer is efficient, as suggested by the good OSC device performance, one may expect the NFA GSB to remain at roughly the same intensity and the polymer GSB to rise markedly. Indeed, this is the case in PM6:Y6. Thus, we expect that there is a new PIA forming underneath the GSB region as a result of the hole transfer process that is dragging the IEICO-2F GSB down and counteracting the expect rise in the PTB7-Th GSB. As the PTB7-Th hole PIA is widely reported to lie at 1150 nm[8–10], we assign this new PIA to the charge on IEICO-2F. Importantly, there is no new PIA formed around 1350 nm, where the IEICO-2F T_1 is found. **(b)** The kinetics of the PTB7-Th:IEICO-2F film in relevant spectral regions. From the rise in the PTB7-Th GSB region, we can see that hole transfer is completed by around 100 ps, which seems to be a common timescale for almost all low-offset NFA blends. The kinetics of the IEICO-2F GSB region and the IEICO-2F S_1 PIA almost perfectly mirror each other, suggesting that the process that is quenching singlets (hole transfer), is also responsible for the formation of the new PIA underneath the IEICO-2F GSB that is pulling it down. This provides more evidence for the formation of a new PIA band, corresponding to the IEICO-2F charge, underneath the GSB.

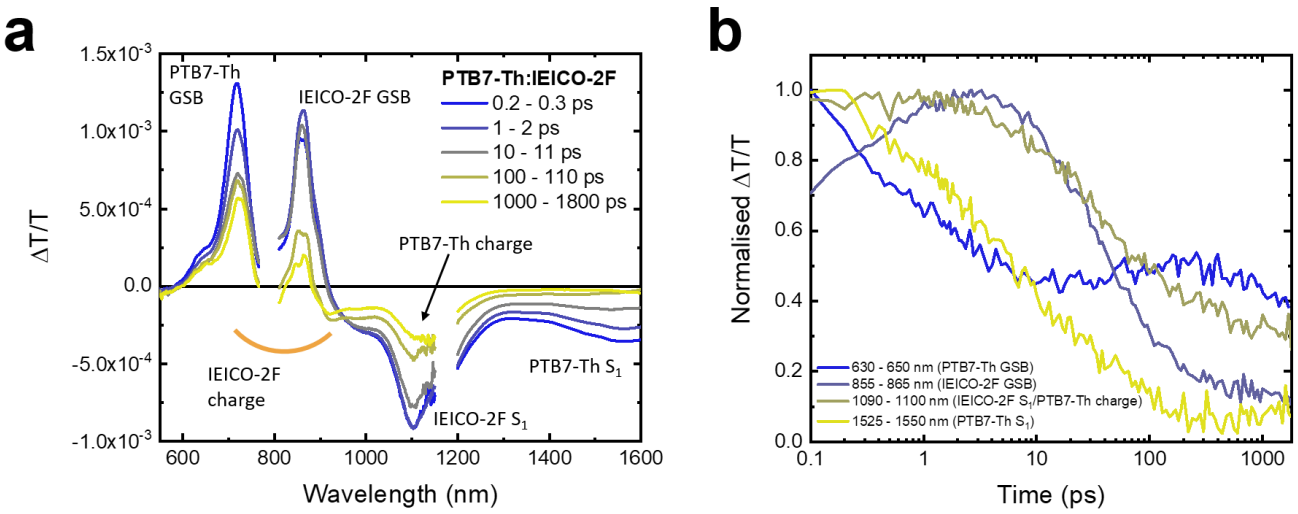

Figure S16: (a) The TA spectra of a PTB7-Th:IEICO-2F film, pumped at 620 nm for preferential PTB7-Th excitation with a low fluence of 1.3 μJ cm^{-2}. At the earliest times, the PTB7-Th GSB and S_1 PIA are present, as expected. However, the IEICO-2F GSB and S_1 PIA are also observable, suggesting that a significant amount of direct NFA excitation has occurred. Interestingly, the PTB7-Th S_1 PIA then decays on ps timescales, with a corresponding rise of the IOTIC-2F GSB. What is interesting is the simultaneous decrease in the PTB7-Th GSB in-line with the S_1 decay: if solely electron transfer was occurring, such a decrease would not be expected. Therefore, we suggest that energy transfer is occurring simultaneously with charge transfer from D to A in this blend. After ~10 ps, the IEICO-2F GSB begins to fall again, with a corresponding decrease in the PTB7-Th GSB peak and the IEICO-2F S_1 PIA. This is in-line with the timescales observed for the hole transfer from IEICO-2F to PTB7-Th in Fig. S12. As before, there is no evidence for the formation of the IEICO-2F T_1 PIA at 1350 nm. **(b)** The kinetics of the PTB7-Th:IEICO-2F film in relevant spectral regions. To support the assignments discussed above, we note that there is a clear rise in the IEICO-2F GSB towards 3 ps, suggesting a population transfer from PTB7-Th, before the back hole transfer takes place. Additionally, in the kinetic taken from the edge of the PTB7-Th GSB shows a re-bleaching of PTB7-Th chains occurs due to this back hole transfer process.

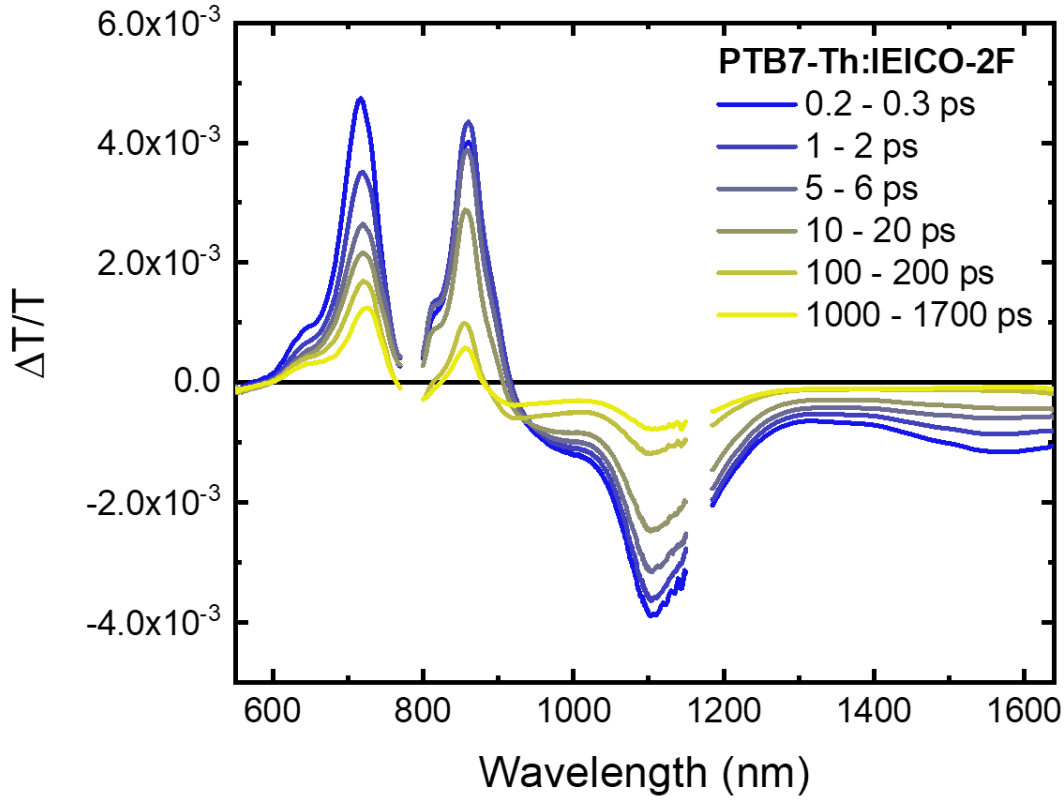

Figure S17: The full TA spectra of Fig. 2d: a PTB7-Th:IEICO-2F film, pumped at 620 nm for preferential PTB7-Th excitation with a moderate fluence of 3.8 μJ cm^{-2}.

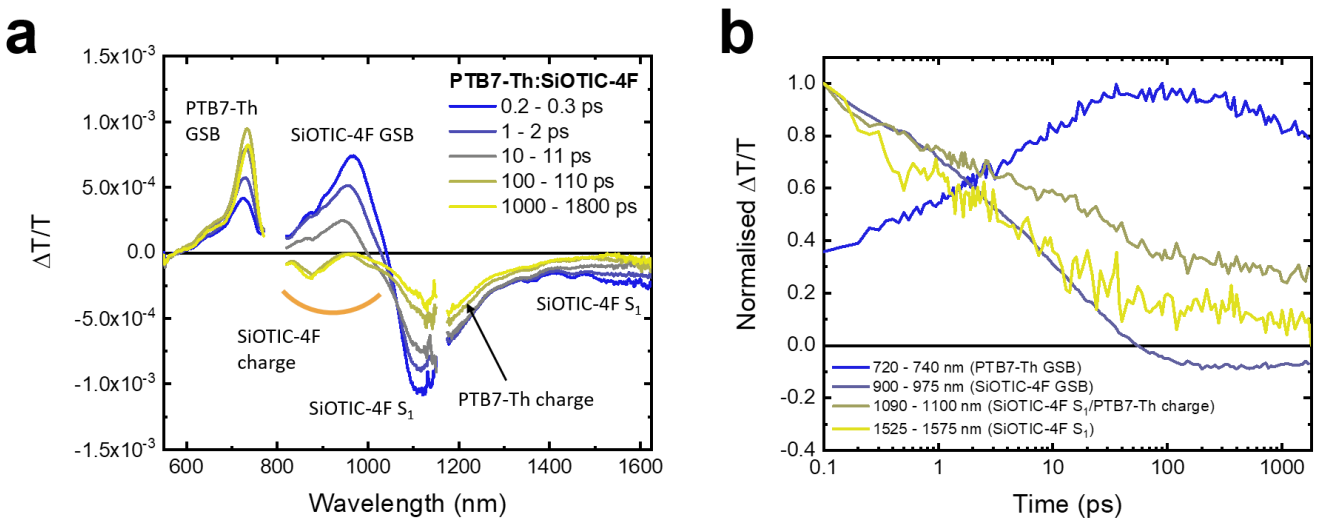

Figure S18: (a) The TA spectra of a PTB7-Th:SiOTIC-4F film, pumped at 975 nm for selective SiOTIC-4F excitation with a low fluence of 1.6 μJ cm^{-2}. At the earliest times, we can clearly see the SiOTIC-4F GSB and sharp S_1 PIA at 1100 nm. Additionally, the PTB7-Th GSB is also present at 0.2 ps, suggesting that some of the hole transfer occurs on ultrafast timescales. As time progresses, the PTB7-Th GSB continues to rise, with a concomitant fall in the SiOTIC-4F S_1 PIA at 1100 nm. The PTB7-Th hole PIA at 1150 nm is also clearly visible by 100 ps, more obvious than in the PTB7-Th:IEICO-2F blend as it is a little red-shifted from the NFA S_1 PIA. Additionally, this blend also exhibits similar behaviour to PTB7-Th:IEICO-2F, where upon charge transfer occurring, the GSB of the NFA falls sharply. Thus, as no other PIAs that could be attributed to charges on SiOTIC-4F are visible elsewhere, we suggest that the SiOTIC-4F charge PIA lies under the GSB. Unfortunately, the SiOTIC-4F T_1 PIA overlaps almost perfectly with the PTB7-Th hole PIA (Fig. S4d), meaning it is not immediately obvious to determine whether triplet formation occurs. This will be revisited shortly. **(b)** The kinetics of the PTB7-Th:SiOTIC-4F film in relevant spectral regions. We note that the PTB7-Th GSB peaks at around 30 ps, suggesting hole transfer is completed by this time.

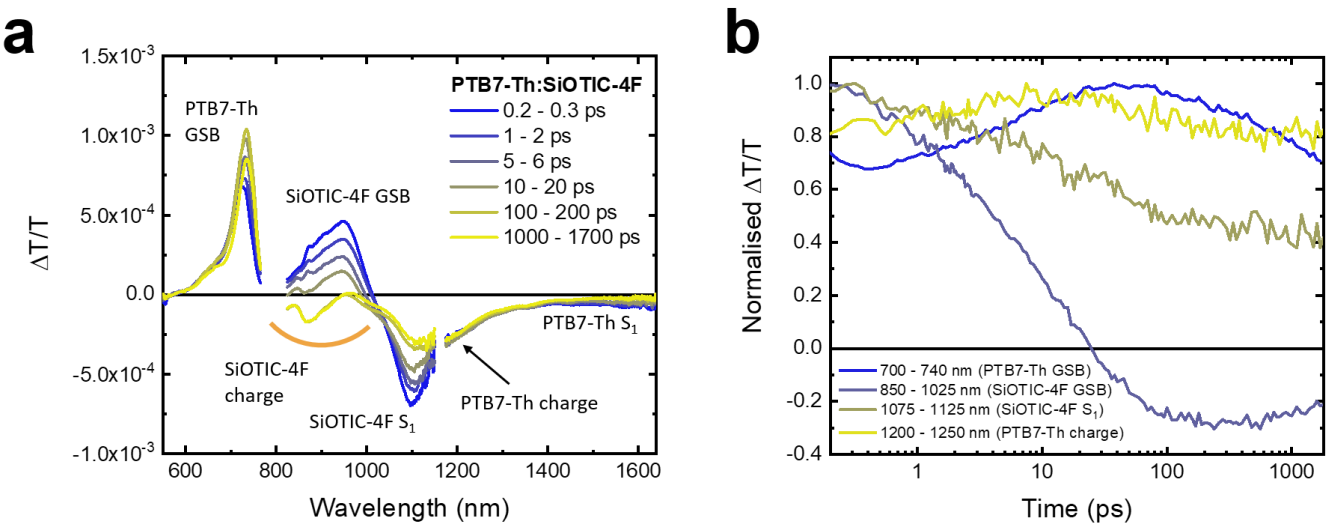

Figure S19: (a) The TA spectra of a PTB7-Th:SiOTIC-4F film, pumped at 620 nm for preferential PTB7-Th excitation with a low fluence of 2.1 μJ cm^{-2}. At the earliest times, the PTB7-Th GSB is present, as expected. However, the PTB7-Th S_1 PIA is not obvious and the SiOTIC-4F GSB, which would be expected to increase in intensity following electron transfer from the D, is also at a maximum at the earliest times resolvable. This suggests that the initial electron transfer process from PTB7-Th is ultrafast, occurring on sub-100 fs timescales. The SiOTIC-4F S1 PIA is also clearly visible at 1100 nm, suggesting some unintentional NFA excitation has also occurred. The spectrum then evolves in a very similar fashion to Fig. S17, when the SiOTIC-4F was selectively excited, confirming that what occurs over longer timescales is the hole transfer from SiOTIC-4F. **(b)** The kinetics of the PTB7-Th:SiOTIC-4F film in relevant spectral regions. We note that the PTB7-Th GSB peaks at around 30 ps, consistent with the hole transfer timescales observed previously when the blend was excited at 975 nm.

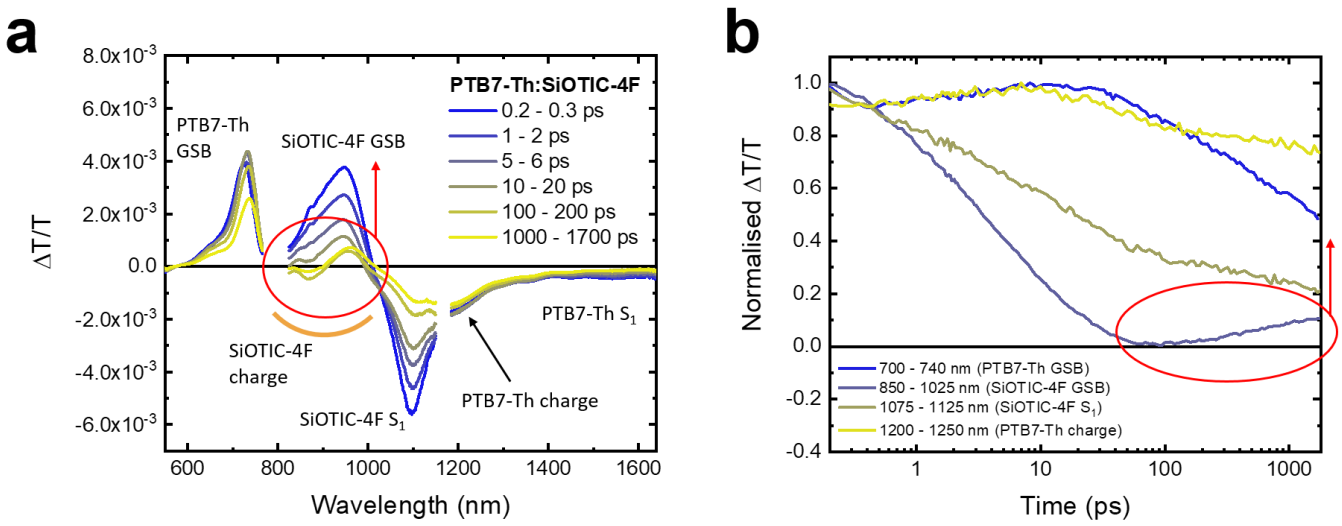

Figure S20: (a) The TA spectra of a PTB7-Th:SiOTIC-4F film, pumped at 620 nm for preferential PTB7-Th excitation with a high fluence of 10.5 μJ cm^{-2}. Compared to the low fluence measurement in Fig. S19, we note that the SiOTIC-4F GSB is substantially above zero by 100 ps, highlighted by the red circle. **(b)** The kinetics of the PTB7-Th:SiOTIC-4F film in relevant spectral regions. There are increased rates of non-geminate recombination in this higher fluence measurement, most obvious in the more rapid loss of the PTB7-Th GSB. The kinetic of the SiOTIC-4F GSB region in this measurement clearly differs from the low fluence measurement, where it doesn't dip below zero and actually increases from 100 ps onwards.

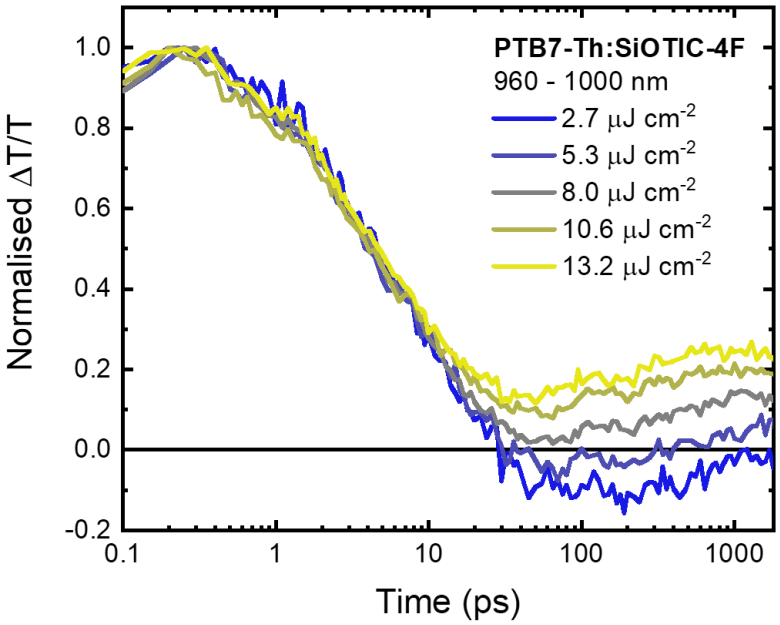

Figure S21: The kinetics taken from the SiOTIC-4F GSB region of a PTB7-Th:SiOTIC-4F film, pumped at 532 nm for preferential PTB7-Th excitation. In order to elucidate the dynamics of this unusual behaviour of the SiOTIC-4F, a detailed fluence series was performed. We note that with increasing fluence, the intensity of the region associated with the SiOTIC-4F GSB (960 – 1000 nm) increases more and more rapidly, reaching a higher proportion of the initial intensity at ever earlier times. This, combined with the loss of charges on PTB7-Th and the recovery of its GSB (Fig. S20), implies that a new species is being created on SiOTIC-4F from charge carriers. Given the strong fluence dependence of the creation of this new species, we assign this process to the formation of triplet excitons on SiOTIC-4F via a BCT from the ^{3}CT, which is formed more rapidly via increased levels of non-geminate recombination at higher fluences[11,12]. Importantly, the rise of the SiOTIC-4F GSB is not actually due to the presence of the triplets themselves increasing the number of NFA molecules being bleached. Rather, it is due to the loss of the charge PIA underneath the SiOTIC-4F GSB, coupled with a minimal change in the number of NFA molecules not in the ground state which results in the rise; the SiOTIC-4F molecules previously bleached by an electron will continue to be bleached by the presence of a triplet. Thus, as we cannot use the T_1 PIA to reliably determine whether triplets form due to its overlap with the PTB7-Th charge PIA, this detailed study of the GSB dynamics provides us an alternative route to investigate triplet formation.

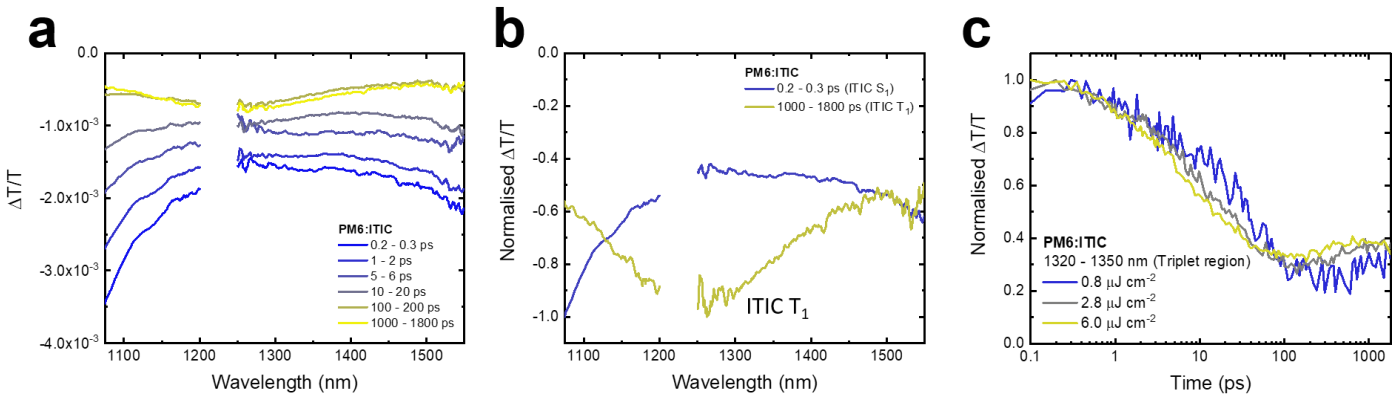

Figure S22: (a) The TA spectra in the NIR region of a PM6:ITIC film, pumped at 700 nm for selective ITIC excitation with a high fluence of 6.0 μJ cm^{-2}. Features associated with the ITIC S_1 at 1100 nm and 1550 nm decay away on ps timescales due to hole transfer to PM6. By 100 ps, a new PIA band centred at 1250 nm is visible. This feature is assigned to the ITIC T_1, due to the perfect spectral match with previous reports[1]. **(b)** The normalised spectra at 0.2 – 0.3 ps and 1000 – 1800 ps to more clearly show the ITIC T_1 PIA band. **(c)** TA kinetics of a fluence series taken from the spectral region associated with the ITIC T_1 PIA. More rapid decay can initially be seen at higher fluences, indicating bimolecular recombination processes are taking place (e.g. exciton-exciton annihilation or non-geminate recombination). However, from ~100 ps onwards, the region associated with the ITIC T_1 becomes increasingly more intense at earlier times with higher fluence. This is consistent with triplet formation via non-geminate recombination (NGR), as the greater charge density in the film increases the probability of NGR events that form the ^{3}CT feeder state[11–13]. Therefore, the fluence dependence of T_1 formation confirms PM6:ITIC forms triplets via NGR.

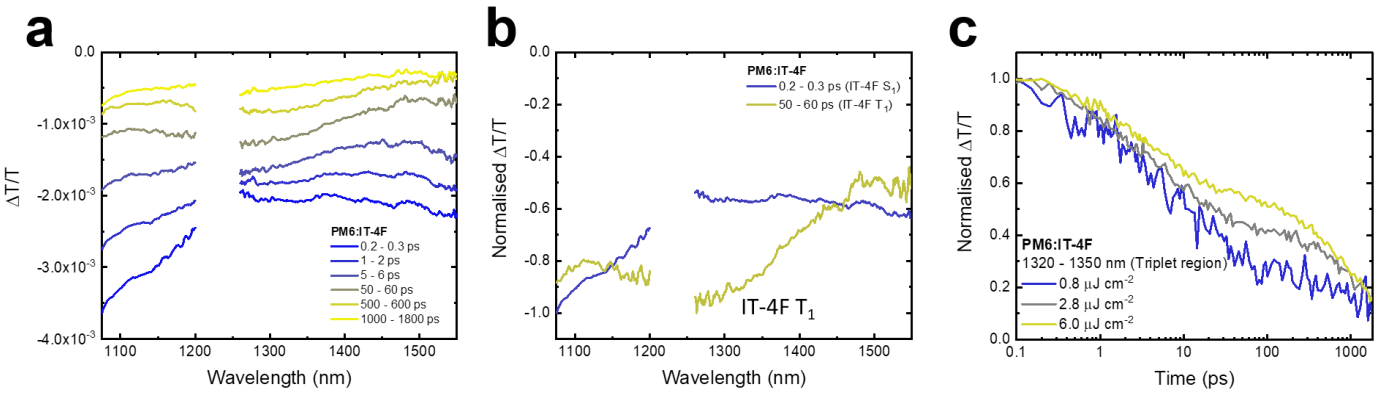

Figure S23: (a) The TA spectra in the NIR region of a PM6:IT-4F film, pumped at 700 nm for selective IT-4F excitation with a high fluence of 6.0 μJ cm^{-2}. Features associated with the IT-4F S_1 at 1100 nm and 1550 nm decay away on ps timescales due to hole transfer to PM6. By 100 ps, a new PIA band centred at 1250 nm is visible. This feature is assigned to the IT-4F T_1, due to the perfect spectral match with previous reports[1]. **(b)** The normalised spectra at 0.2 – 0.3 ps and 1000 – 1800 ps to more clearly show the IT-4F T_1 PIA band. **(c)** TA kinetics of a fluence series taken from the spectral region associated with the IT-4F T_1 PIA. From ~10 ps onwards, the region associated with the IT-4F T_1 becomes increasingly more intense at earlier times with higher fluence. This is consistent with triplet formation via NGR, as the greater charge density in the film increases the probability of NGR events that form the ^{3}CT feeder state[11–13]. Therefore, the fluence dependence of T_1 formation confirms PM6:IT-4F forms triplets via NGR.

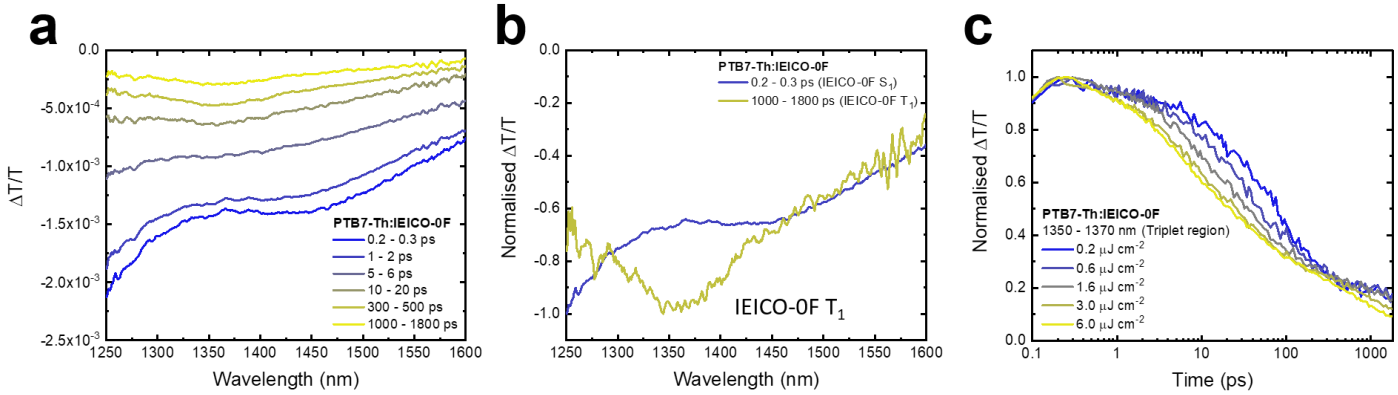

Figure S24: (a) The TA spectra in the NIR region of a PTB7-Th:IEICO-0F film, pumped at 800 nm for selective IEICO-0F excitation with a high fluence of 6.0 μJ cm^{-2}. The PIA associated with the IEICO-0F S_1 at 1250 nm decays away on ps timescales due to both decay back to the ground state and hole transfer to PTB7-Th. By 300 ps, a new PIA band centred at 1370 nm is visible. This feature is assigned to the IEICO-0F T_1, due to the perfect spectral match with Fig. S37b. **(b)** The normalised spectra at 0.2 – 0.3 ps and 1000 – 1800 ps to more clearly show the IEICO-0F T_1 PIA band. **(c)** TA kinetics of a fluence series taken from the 1350 – 1370 nm spectral region associated with the IEICO-0F T_1 PIA. Whilst triplets do indeed form in this blend, their dynamics are not what would be expected for triplets formed via NGR. A detailed fluence series reveals that <100 ps, there is a clear increase in the excited state decay rate. We attribute this to increased singlet exciton-exciton annihilation (the S_1 PIA also has significant intensity around 1350 – 1370 nm), not non-geminate recombination, as minimal hole transfer has occurred by 100 ps (Fig. S25). After 100 ps, when the T_1 PIA begins to become clearly visible, there is no fluence dependence in this region for lower fluences between 0.2 – 1.6 μJ cm^{-2}. A fluence dependence in the T_1 region only becomes apparent for higher fluences of 3.0 – 6.0 μJ cm^{-2}. However, the decay rate in the 1350 – 1370 nm region actually increases, which is not what would be expected if triplets were being formed via NGR. Therefore, this rules out NGR as a significant triplet formation mechanism in this blend, with the increased T_1 decay rate likely attributable to triplet-charge annihilation[12,14]. This leaves two possible routes for the triplet formation: ISC from the geminate ^{1}CT, or direct ISC from un-dissociated IEICO-0F singlets. From the trEPR (Fig. S60), we rule out the former as only ISC triplets are present. Further, we note that the kinetics of the T_1 region perfectly matches the kinetics taken from the same wavelength region in the PS:IEICO-0F film, which exhibits a relatively high (~5%) yield of ISC triplets (Fig. S35b). This confirms that the primary triplet formation route in PTB7-Th:IEICO-0F is the ISC of un-dissociated singlet excitons, facilitated by the slow hole transfer rate. This is consistent with the poor device performance observed in this blend, which is much worse than the PTB7-Th:IEICO-2F and -4F devices.

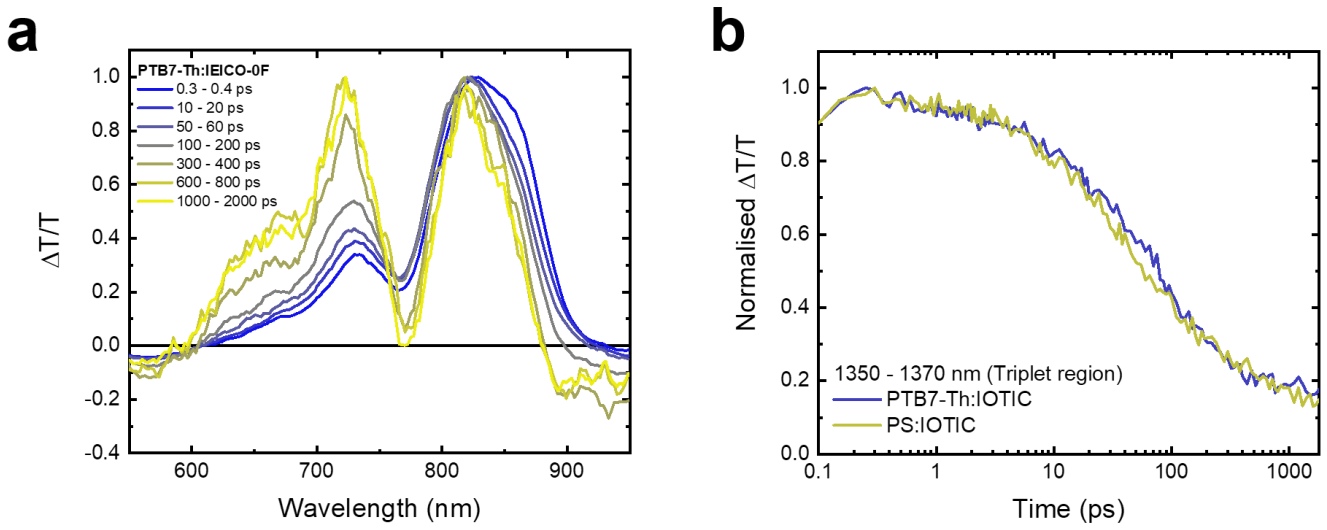

Figure S25: Additional data to assist with the understanding of the PTB7-Th:IEICO-0F triplet formation discussion. **(a)** The normalised TA spectra of a PTB7-Th:IEICO-0F film, excited at 860 nm for selective IEICO-0F excitation with a fluence of 0.5 μJ cm^{-2}. Initially, only the IEICO-0F GSB is visible, as expected. However, we note that the PTB7-Th GSB does not become readily apparent until 300 ps, by which time significant decay of IEICO-0F singlets to the ground state and to T_1 via ISC will have occurred. This can explain the inferior performance of the PTB7-Th:IEICO-0F blend compared to the -2F and -4F equivalents. **(b)** The normalised TA kinetics of PTB7-Th:IEICO-0F and PS:IEICO-0F 1:1.5 films taken around the maximum of the IEICO-0F T_1 PIA at 1350 – 1370 nm. The dynamics of this region overlap almost perfectly, strongly suggesting that the triplet formation mechanism in PTB7-Th:IEICO-0F is primarily via direct ISC of un-dissociated singlet excitons; this is consistent with the observation of an intense ISC triplet signal in the trEPR (Fig. S56).

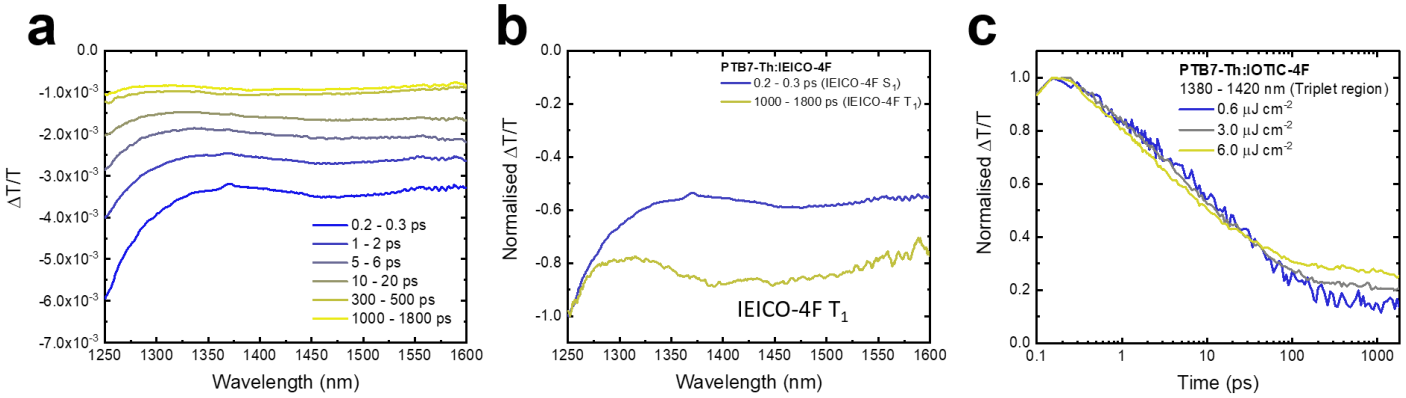

Figure S26: (a) The TA spectra in the NIR region of a PTB7-Th:IEICO-4F film, pumped at 800 nm for selective IEICO-4F excitation with a high fluence of 6.0 μJ cm^{-2}. The PIA associated with the IEICO-4F S_1 at 1250 nm decays away on ps timescales due to hole transfer to PTB7-Th. By 300 ps, a new broad new PIA band centred at 1400 nm is visible. This feature is assigned to the IEICO-4F T_1, due to the perfect spectral match with Fig. S39f. **(b)** The normalised spectra at 0.2 – 0.3 ps and 1000 – 1800 ps to more clearly show the IEICO-4F T_1 PIA band. **(c)** TA kinetics of a fluence series taken from the spectral region associated with the IEICO-4F T_1 PIA. More rapid decay can initially be seen at higher fluences, indicating bimolecular recombination processes are taking place (e.g. exciton-exciton annihilation or NGR). However, from ~50 ps onwards, the region associated with the IEICO-4F T_1 becomes increasingly more intense at earlier times with higher fluence. This is consistent with triplet formation via NGR, as the greater charge density in the film increases the probability of NGR events that form the ^{3}CT feeder state[11–13]. Therefore, the fluence dependence of T_1 formation confirms PTB7-Th:IEICO-4F forms triplets via NGR.

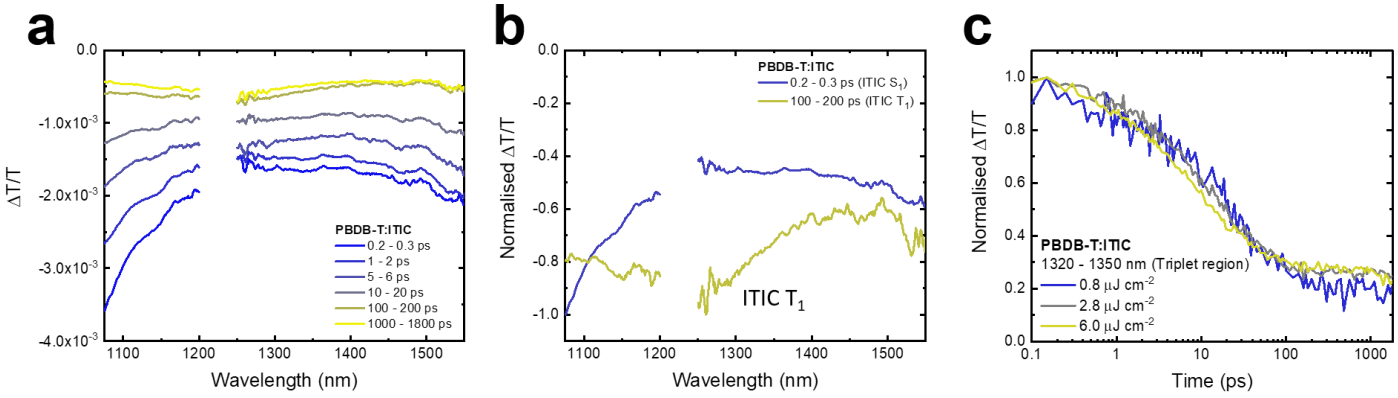

Figure S27: (a) The TA spectra in the NIR region of a PBDB-T:ITIC film, pumped at 700 nm for selective ITIC excitation with a high fluence of 6.0 μJ cm^{-2}. Features associated with the ITIC S_1 at 1100 nm and 1550 nm decay away on ps timescales due to hole transfer to PBDB-T. By 100 ps, a new PIA band centred at 1250 nm is visible. This feature is assigned to the ITIC T_1, due to the perfect spectral match with previous reports[1]. **(b)** The normalised spectra at 0.2 – 0.3 ps and 1000 – 1800 ps to more clearly show the ITIC T_1 PIA band. **(c)** TA kinetics of a fluence series taken from the spectral region associated with the ITIC T_1 PIA. More rapid decay can initially be seen at higher fluences, indicating bimolecular recombination processes are taking place (e.g. exciton-exciton annihilation or NGR). However, from ~100 ps onwards, the region associated with the ITIC T_1 becomes increasingly more intense at earlier times with higher fluence. This is consistent with triplet formation via NGR, as the greater charge density in the film increases the probability of NGR events that form the ^{3}CT feeder state[11–13]. Therefore, the fluence dependence of T_1 formation confirms PBDB-T:ITIC forms triplets via NGR.

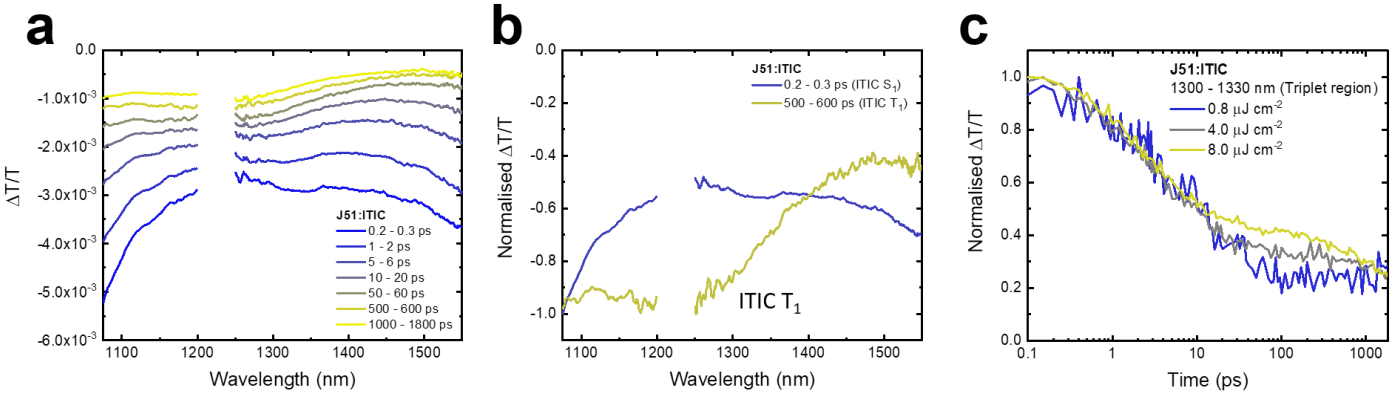

Figure S28: (a) The TA spectra in the NIR region of a J51:ITIC film, pumped at 680 nm for selective ITIC excitation with a high fluence of 8.0 μJ cm^{-2}. Features associated with the ITIC S_1 at 1100 nm and 1550 nm decay away on ps timescales due to hole transfer to J51. By 100 ps, a new PIA band centred at 1250 nm is visible. This feature is assigned to the ITIC T_1, due to the perfect spectral match with previous reports[1]. **(b)** The normalised spectra at 0.2 – 0.3 ps and 1000 – 1800 ps to more clearly show the ITIC T_1 PIA band. **(c)** TA kinetics of a fluence series taken from the spectral region associated with the ITIC T_1 PIA. From ~10 ps onwards, the region associated with the ITIC T_1 becomes increasingly more intense at earlier times with higher fluence. This is consistent with triplet formation via NGR, as the greater charge density in the film increases the probability of NGR events that form the ^{3}CT feeder state[11–13]. Therefore, the fluence dependence of T_1 formation confirms J51:ITIC forms triplets via NGR.

Electro-absorption analysis of NFA blends to determine $k_{dissociation}$

In OSC blends, the timescales of the CT state dissociation can be readily determined by evaluating the electro-absorption (EA) features in the TA[3]. The EA represents the Stark-shift of the material absorption spectrum by the electric field of the separating charges, with the maximum intensity reached when the CT states have dissociated into FC[3–6]. Thus, tracking the EA response provides an insight into the kinetics of charge separation. We note that the EA typically manifests as a sharp, negative signal in the TA at the steady-state absorption edge[3–6]. Here, we have investigated the kinetics of the EA formation in all NFA blends where the EA response of the D polymer is not obscured by the GSB of the NFA (i.e. those with sufficiently large offsets of the peak D and A absorption peaks). To obtain the dissociation rate, we have fitted the growth of the EA feature with a mono-exponential function; excellent agreement with the rise of the EA is found using this method. From this, we calculate $k_{dissociation}$ by taking the inverse of the time constant associated with the exponential EA growth. In all NFA blends analysed, we find the CT dissociation takes place with a time constant of tens of ps (reaching a maximum after ~100 – 200 ps), corresponding to a $k_{dissociation}$ of between 10^{10} – 10^{11} s^{-1}. Importantly, as the vibrational relaxation of CT states is much faster (<100 fs) than these observed dissociation timescales[15,16], the initial separation following charge transfer must occur from the same thermalized CT states as formed by NGR. Thus the dissociation timescales extracted here will be relevant when considering whether ^{3}CT state re-dissociation can out-compete BCT to T_1, the key factor controlling whether T_1 formation occurs. In contrast to the NFA systems, the EA response is already near-maximum in the PM6:PC_{60}BM blend by 1 ps (Fig. S10), consistent with the ultrafast long-range charge separation typically observed in fullerene systems with a net driving energy[3–5].

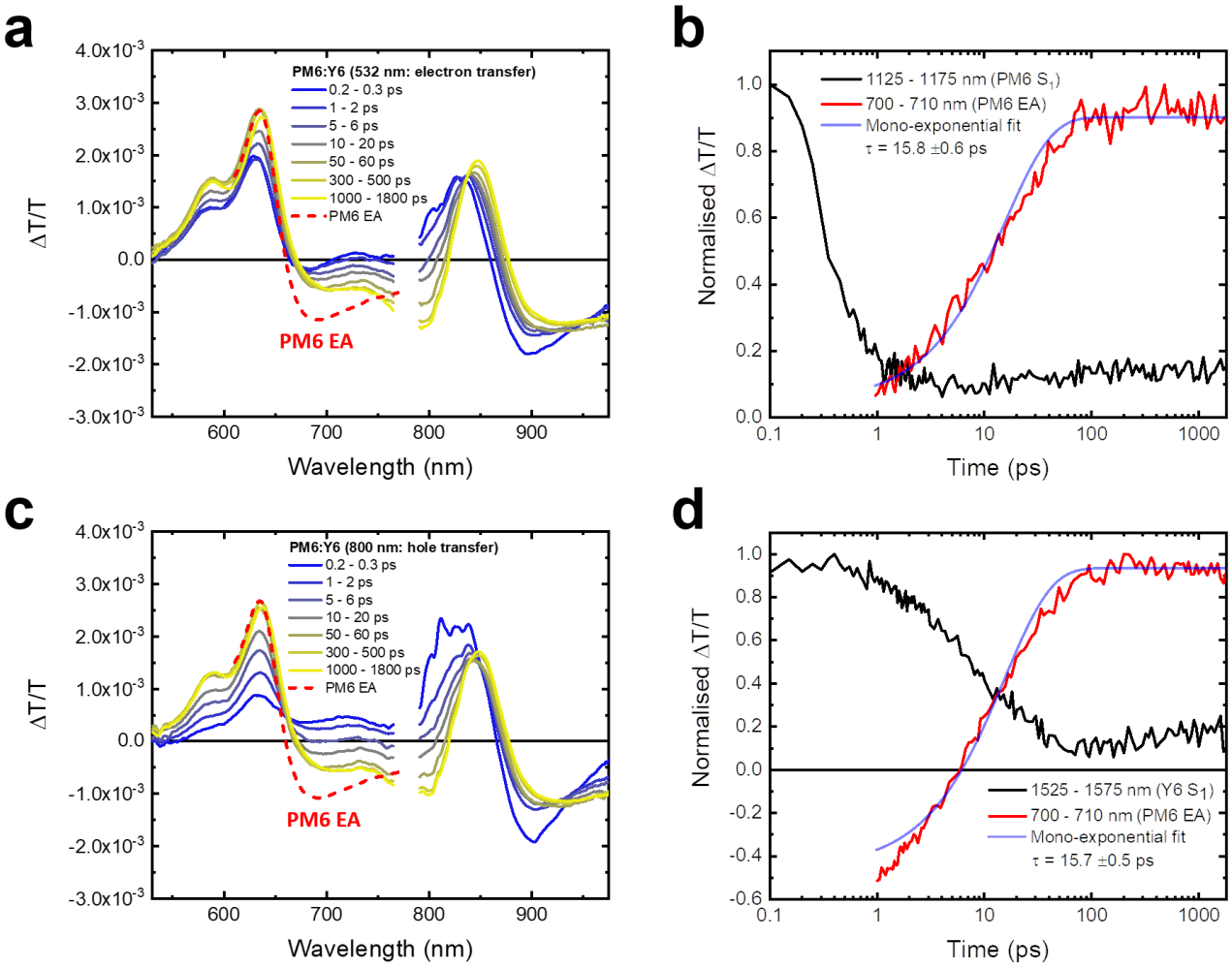

Figure S29: (a) The TA spectra of the PM6:Y6 blend, excited with a low fluence of 1.8 μJ cm^{-2} at 532 nm for preferential PM6 excitation. The primary process occurring in this blend is electron transfer from PM6 to Y6. A new negative band between 700 – 750 nm grows in over timescales up to 100 ps. Through comparison to the EA obtained from a PM6:$PC_{60}BM$ blend (dashed red line), this new feature is assigned to the EA of PM6 by the separating charges. The differences in spectral shape can be explained by the overlap with the vibronic shoulder of the Y6 GSB between 650 – 750 nm. **(b)** The TA kinetics of the PM6:Y6 blend following preferential excitation of PM6 at 532 nm. The decay of the PM6 S_1 shows the timescales of electron transfer in the blend, largely taking place <1 ps. The kinetic of the EA is also displayed, where it clearly grows in more slowly than the time taken for electron transfer. This represents CTE dissociation into FC in the blend, which takes up to 100 ps. The EA growth can be fitted with a mono-exponential function with a time constant of 15.8 ±0.6 ps, yielding $k_{dissociation}$ = 6.3 x 10^{10} s^{-1}. Critically, as the time taken for CTE dissociation is much slower than the vibrational relaxation of CTEs (<100 fs), it will take place from the same thermalized CTEs that are formed by NGR. **(c)** The TA spectra of the PM6:Y6 blend, excited with a low fluence

of 1.0 μJ cm^{-2} at 800 nm for selective Y6 excitation. The only process occurring in this blend is hole transfer from Y6 to PM6. Again, the PM6 EA feature between 700 – 750 nm can be seen to grow in over similar timescales as before, up to 100 ps. **(d)** The TA kinetics of the PM6:Y6 blend following preferential excitation of Y6 at 800 nm. The decay of the Y6 S_1 shows the timescales of hole transfer in the blend, largely taking place <100 ps. The kinetic of the EA is also displayed, where it grows in over identical timescales to the blend after electron transfer, with a time constant of 15.7 ±0.5 ps obtained from a mono-exponential fit. The consistency in timescales between electron and hole transfer confirms that charge separation proceeds in the same manner for both, despite the latter taking place more slowly and with a much smaller frontier molecular orbital energetic offset.

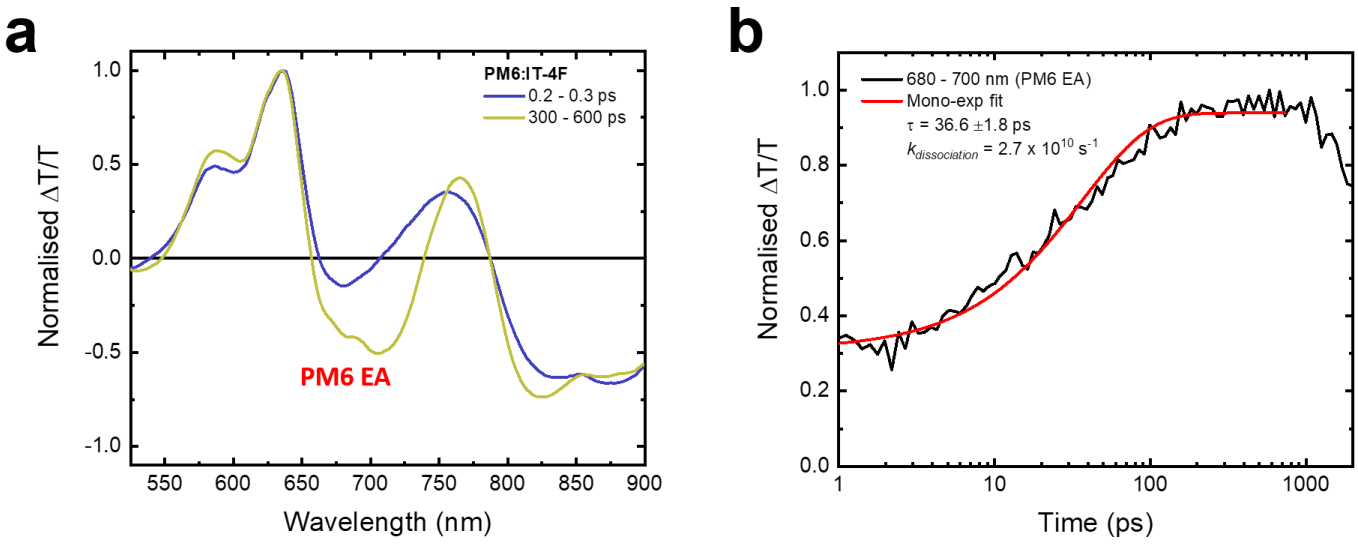

Figure S30: (a) The normalised TA spectra of a PM6:IT-4F film, pumped at 532 nm for preferential PM6 excitation with a fluence of 2.9 μJ cm^{-2}. At 0.2 ps, the PM6 and IT-4F GSBs are visible between 550 – 650 and 700 – 770 nm, respectively. By 300 – 600 ps, a new negative band has formed at the edge of the PM6 GSB at 680 nm. This feature is assigned to EA of PM6 (Fig. S10). **(b)** By tracking the kinetic from the EA region, we can visualise the separation of charge carriers, with the maximum intensity reached when they have fully separated. The EA peaks at 200 ps and can be well-described by a mono-exponential function with a time constant of 36.6 ±1.8 ps: this corresponds to a $k_{dissociation}$ =2.7x10^{10} s^{-1}.

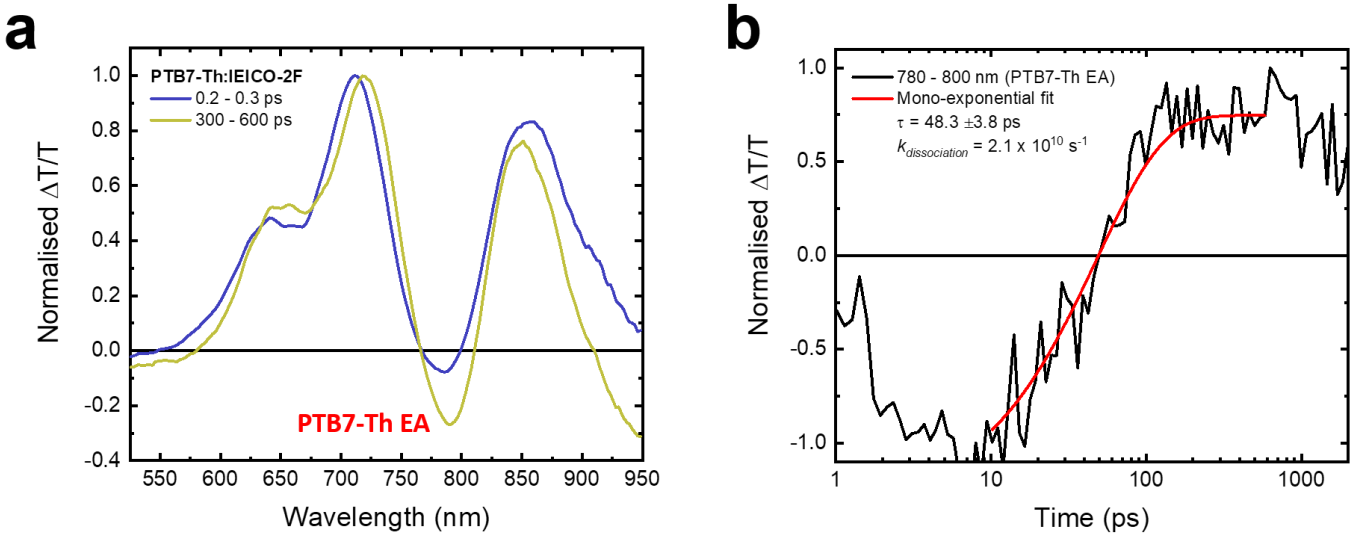

Figure S31: (a) The normalised TA spectra of a PTB7-Th:IEICO-2F film, pumped at 580 nm for preferential PTB7-Th excitation with a fluence of 2.1 μJ cm^{-2}. At 0.2 ps, the PTB7-Th and IEICO-2F GSBs are visible between 600 – 750 and 800 – 950 nm, respectively. By 300 – 600 ps, a new negative band has formed at the edge of the PTB7-Th GSB at 790 nm. This feature is assigned to EA of PTB7-Th. **(b)** By tracking the kinetic from the EA region, we can visualise the separation of charge carriers, with the maximum intensity reached when they have fully separated. The EA peaks at 150 ps and can be well-described by a mono-exponential function with a time constant of 48.3 ±3.8 ps: this corresponds to a $k_{dissociation}$ =2.1x10^{10} s^{-1}.

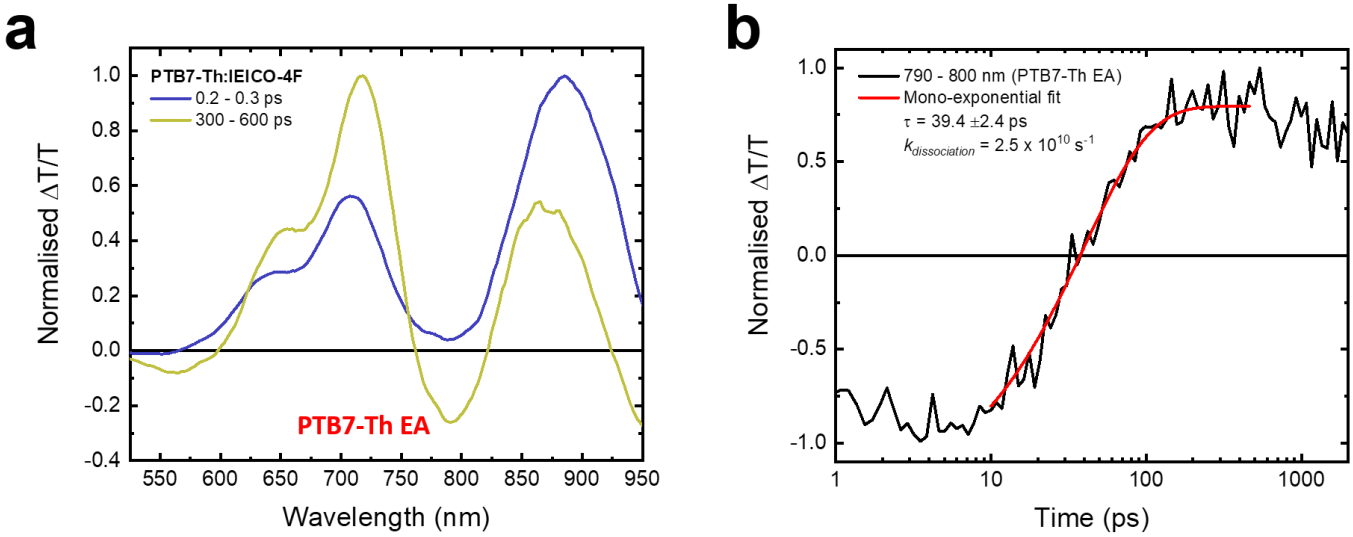

Figure S32: (a) The normalised TA spectra of a PTB7-Th:IEICO-4F film, pumped at 600 nm for preferential PTB7-Th excitation with a fluence of 0.5 μJ cm^{-2}. At 0.2 ps, the PTB7-Th and IEICO-4F GSBs are visible between 600 – 750 and 800 – 950 nm, respectively. By 300 – 600 ps, a new negative band has formed at the edge of the PTB7-Th GSB at 790 nm. This feature is assigned to EA of PTB7-Th. **(b)** By tracking the kinetic from the EA region, we can visualise the separation of charge carriers, with the maximum intensity reached when they have fully separated. The EA peaks at 150 ps and can be well-described by a mono-exponential function with a time constant of 39.4 ±2.4 ps: this corresponds to a $k_{dissociation}$ =2.5x10^{10} s^{-1}.

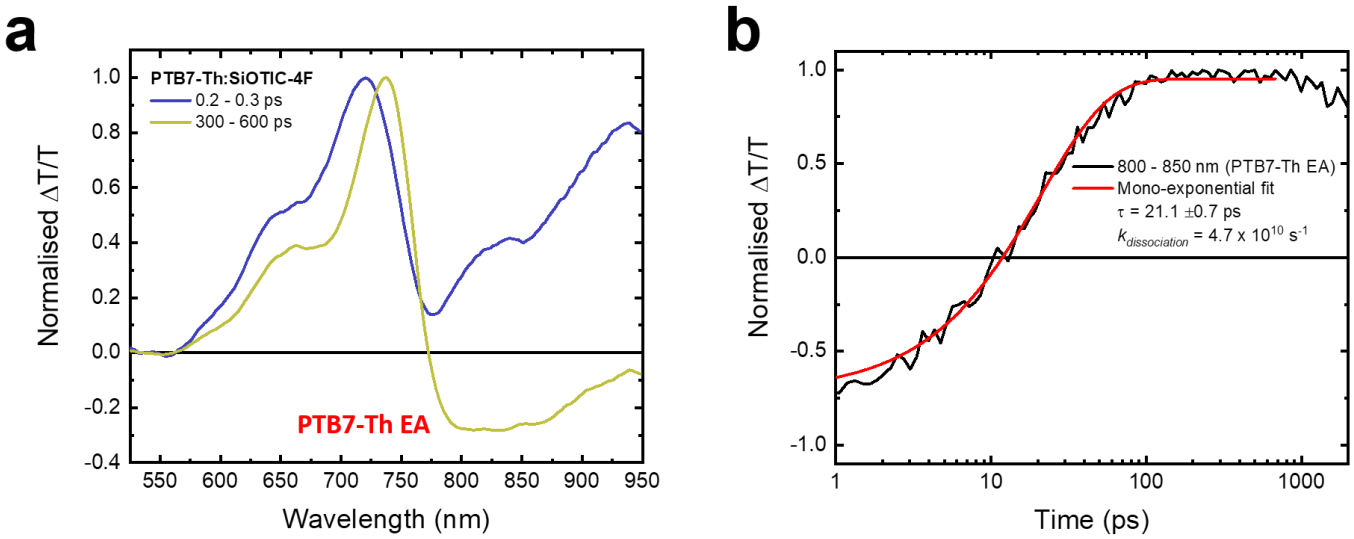

Figure S33: (a) The normalised TA spectra of a PTB7-Th:SiOTIC-4F film, pumped at 580 nm for preferential PTB7-Th excitation with a fluence of 2.1 μJ cm^{-2}. At 0.2 ps, the PTB7-Th and SiOTIC-4F GSBs are visible between 600 – 750 and 800 – 950 nm, respectively. By 300 – 600 ps, a new negative band has formed at the edge of the PTB7-Th GSB at 800 nm. This feature is assigned to EA of PTB7-Th. **(b)** By tracking the kinetic from the EA region, we can visualise the separation of charge carriers, with the maximum intensity reached when they have fully separated. The EA peaks at 100 ps and can be well-described by a mono-exponential function with a time constant of 21.1 ±0.7 ps: this corresponds to a $k_{dissociation}$ =4.7x10^{10} s^{-1}.

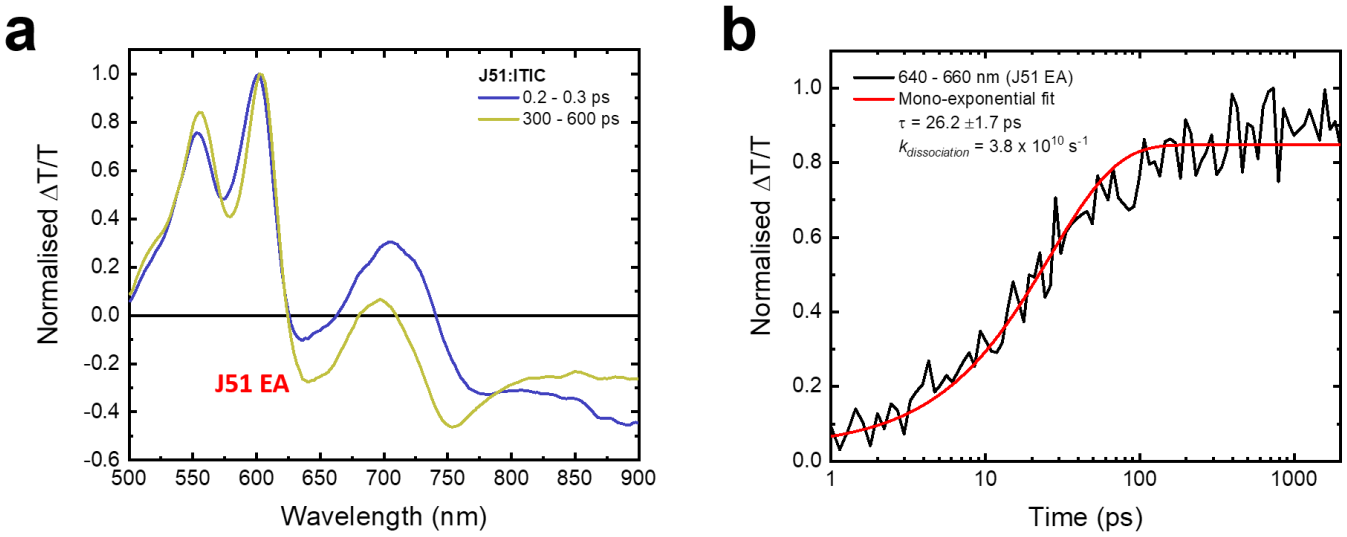

Figure S34: (a) The normalised TA spectra of a J51:ITIC film, pumped at 532 nm for preferential PM6 excitation with a fluence of 2.5 μJ cm^{-2}. At 0.2 ps, the J51 and ITIC GSBs are visible between 500 – 625 and 670 – 750 nm, respectively. By 300 – 600 ps, a new negative band has formed at the edge of the J51 GSB at 640 nm. This feature is assigned to EA of J51. **(b)** By tracking the kinetic from the EA region, we can visualise the separation of charge carriers, with the maximum intensity reached when they have fully separated. The EA peaks at 150 ps and can be well-described by a mono-exponential function with a time constant of 26.2 ±1.7 ps: this corresponds to a $k_{dissociation}$ =3.8x10^{10} s^{-1}.

Investigation of fast ISC in IEICO derivatives

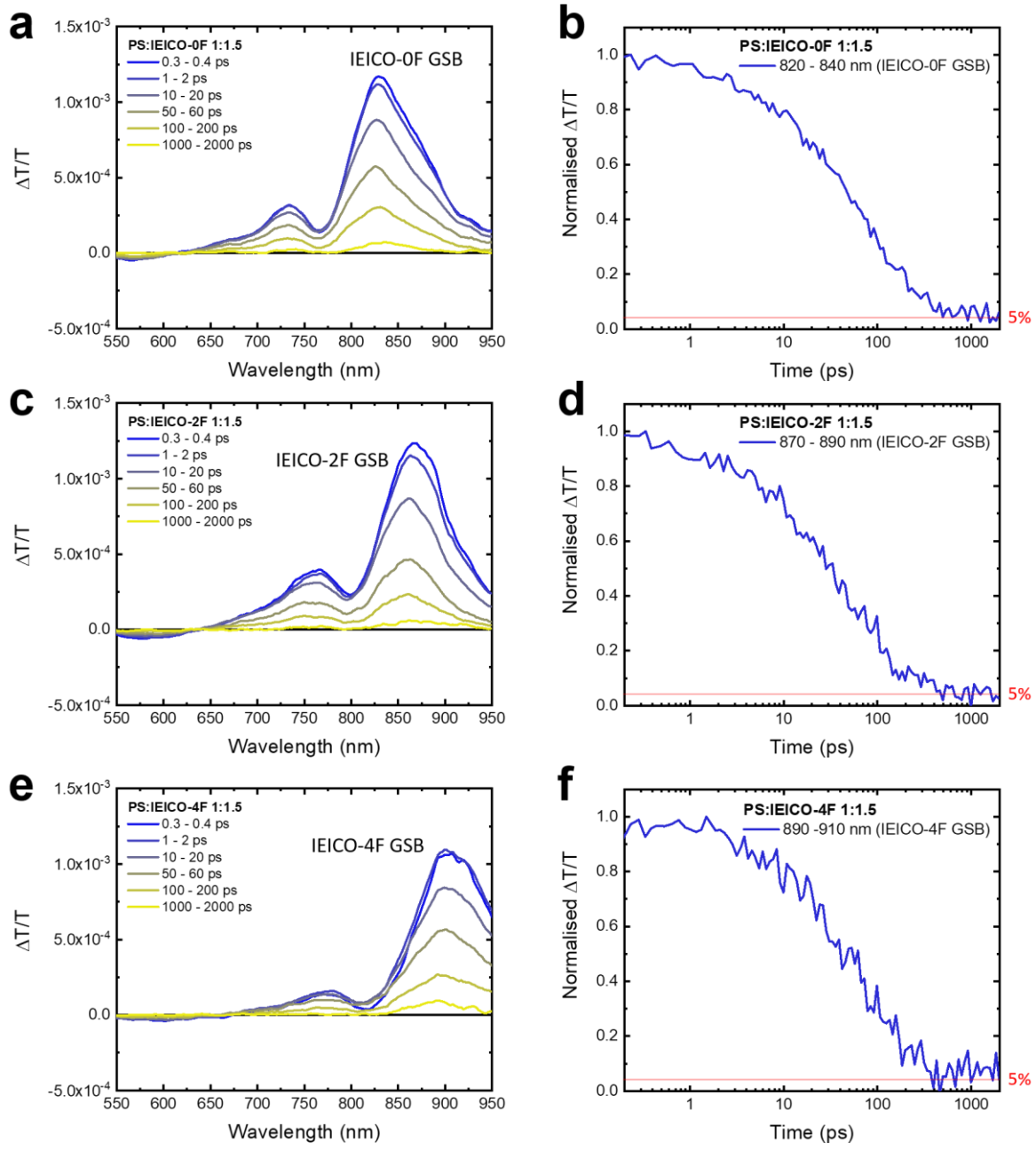

Figure S35: (a, c, e) The TA spectra of PS:IEICO-0F, -2F and -4F 1:1.5 films, pumped at 860, 890 and 925 nm with fluences of 0.74, 0.60 and 0.96 μJ cm^{-2},respectively. Note how there is a small amount of the NFA GSB remaining at 2 ns, significantly longer than the S_1 lifetime of the materials. **(b, d, f)** TA kinetics of the GSB region of the IEICO derivatives. The remaining GSB intensity at 2 ns is ~5% of the peak in all materials. NIR region TA (Fig. S36) confirms that the only species present at this time are triplet excitons, formed via rapid ISC of the IEICO derivatives. Assuming singlet and triplet excitons are localised on one NFA molecule, the quantum efficiency of ISC is ~5% in all IEICO derivatives studied.

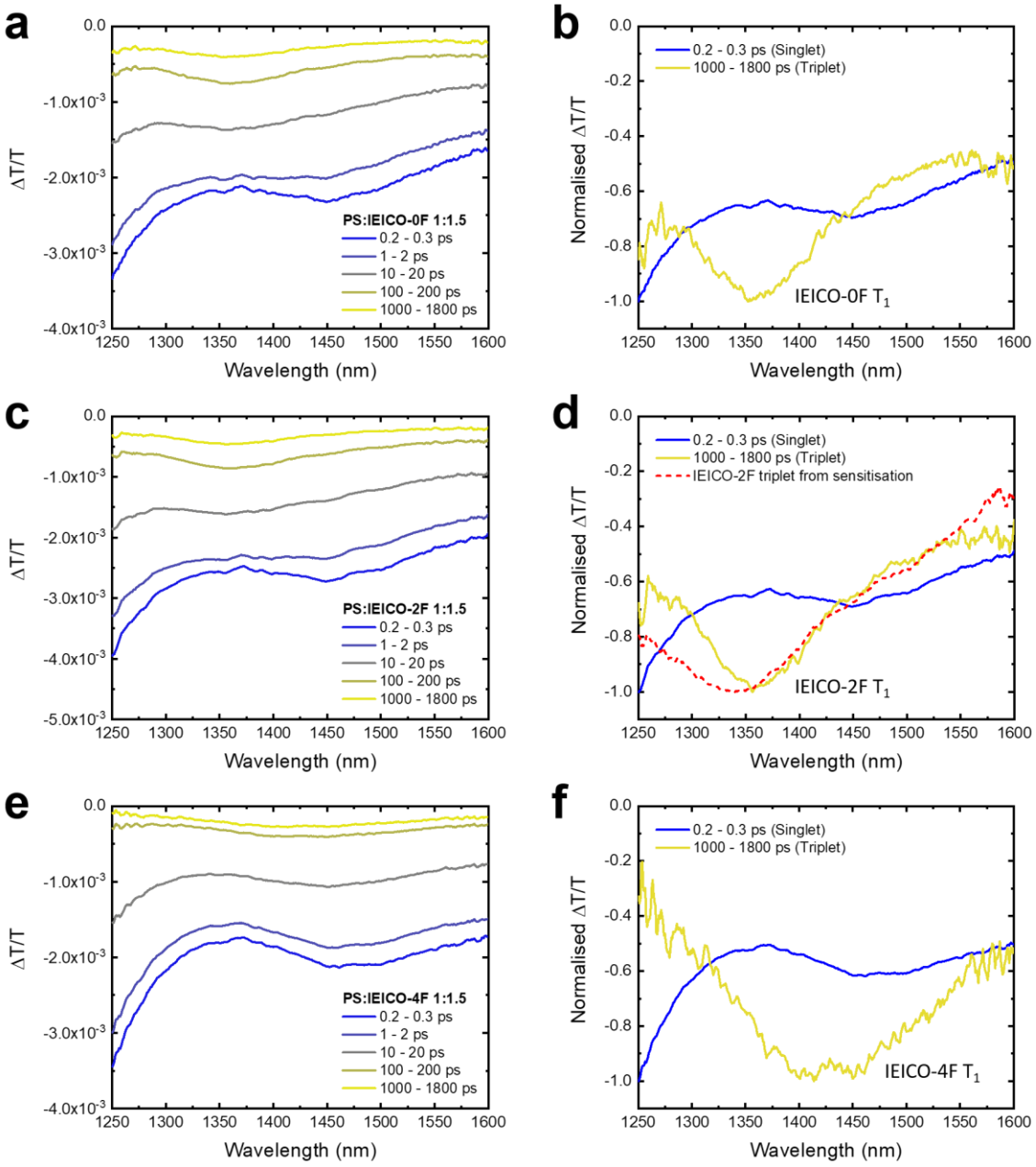

Figure S36: (a, c, e) The TA spectra of PS:IEICO-0F, -2F and -4F 1:1.5 films, all pumped at 800 nm with a fluence of 4.41 μJ cm^{-2}. After the S_1 PIA decays away, a new and long-lived PIA band remains that is assigned to the T_1 of the respective IEICO derivative. **(b, d, f)** Normalised TA spectra of the IEICO derivatives to more clearly show the T_1 PIA. A good match is found between the T_1 PIA of IEICO-2F from the sensitisation experiments and the PIA observed in the PS:IEICO-2F 1:1.5 blend, providing further evidence that this new PIA is the T_1 formed via rapid ISC. The discrepancy around 1250 – 1300 nm is likely due to a small amount of remaining IEICO-2F S_1 states in the sensitised blend; the S_1 lifetime will be enhanced in the PS:PtOEP:NFA 0.94:0.03:0.03 film as the high dilution of the NFA will reduce the non-radiative decay associated with aggregated molecules (concentration quenching).

Quantifying T_1 formation from TA

When quantifying T_1 formation, previous studies have suggested that a kinetic model using triplet-charge annihilation as the T_1-quenching pathway provides the best description of the T_1 dynamics in OSC blends[11–13]. Though triplet-triplet annihilation has also been observed as a T_1-quenching route in fullerene OSCs[17,18], we see no increase in the charge population after T_1 loss in the PM6:Y6 blend (Fig. S38), which would be expected from the separation of S_1 states reformed by triplet-triplet annihilation[18]. Thus, we were able to successfully model the Y6 T_1 population in the TA data of the PM6:Y6 blends using just the recombination of free charges and triplet-charge annihilation:

$$\frac{dN_T}{dt} = -\alpha \frac{dN_C}{dt} - \beta N_T N_C \qquad (1)$$

where N_T and N_C are the experimental T_1 and charge population densities, α is the fraction of recombination events that lead to T_1 formation, and β is the triplet-charge annihilation rate constant. To quantify the number of T_1 and charges present in the blend, we must first determine the absorption cross section (σ) of the T_1 and charge species. The measured change in transmission $\frac{\Delta T}{T}$ in the TA experiment is related to the total population (N) by the following relation:

$$\frac{\Delta T}{T} = \sigma N \qquad (2)$$

To begin, we will calculate σ of the charges (σ_C). To accurately track the population, we need to calculate σ_C at a wavelength where there is significant absorption by the charges, but no overlap with the Y6 GSB (Fig. S6a), or any other species. Therefore, we choose to use the signal at 930 nm, as it is free from other overlapping signals that could affect the accuracy of our modelling. In the very low-fluence TA measurement of the PM6:Y6 blend (Fig. S12a), we have determined that hole transfer following selective excitation of Y6 is completed by 100 ps: at this time in the PM6:Y6 blend, $\frac{\Delta T}{T}$ = -6.40 x 10^{-4} at 930 nm. As we know the absorbance (A) of the film (Fig. S39), we can evaluate the initial number of singlet excitons created on Y6 following excitation. Using A = 0.49 at 800 nm, we determine that 1.31 x 10^{12} singlet excitons have been created on Y6 by the 800 nm, 0.5 μJ cm^{-2} pump pulse (2.4 nJ per pulse). As we know the number of excited states created, we can now estimate the number of charges generated. If we were to assume the quantum efficiency of charge transfer from Y6 S_1 (η_{CT}) =

100%, the number of S_1 initially created (1.31 x 10^{12}) is equal to the charge population at 100 ps. We would then obtain σ_C = 4.90 x 10^{-16} cm^2 from equation 2 at 930 nm.

However, it is almost certain that $\eta_{CT} \neq 100\%$. To better evaluate the true value of η_{CT}, we begin by acknowledging that the photovoltaic internal quantum efficiency (IQE_{PV}) of optimised PM6:Y6 devices is ~90%[19,20]: this means that under operating conditions, 10% of the initially generated Y6 S_1 do not create charge carriers that are successfully extracted from the device. In order to estimate the potential loss pathways, we note that PM6:Y6 devices show exceptionally efficient carrier extraction[19]. Therefore, we expect the main loss pathway to be in the creation of charges, not the extraction. This can be rationalised by noticing that the slow hole transfer rate from Y6 to PM6 (Fig. S12) will have to compete against the relatively rapid S_1 decay of Y6 (Fig. S6), creating a plausible route for the decay of S_1. Therefore, as a conservative estimate, we consider that η_{CT} ~90% for Y6 excitons. To confirm the validity of this assumption, we also compare the timescales for hole transfer and Y6 S_1 decay. The time taken for the population of Y6 S_1 to fall to 1/e of its initial value in the PS:Y6 film is ~100 ps. In contrast, the time for the Y6 S_1 to be quenched to 1/e of their initial population in the blend is ~10 ps (Fig. S40). The ratio of these two lifetimes also gives η_{CT} ~90%, consistent with the value estimated from the IQE_{PV}. Because of this, our original value of σ_C = 4.90 x 10^{-16} cm^2 will be an underestimate as not every S_1 is dissociated; less charges than expected are leading to the observed signal. Therefore, to account for potential losses during charge generation, we divide this value by 0.9 to obtain our final σ_C = 5.44 x 10^{-16} cm^2.

Next, we must calculate σ of the Y6 T_1 (σ_T). We note that a very small fraction of Y6 S_1 undergo intersystem crossing (ISC) to T_1 prior to decay. This provides us a convenient means to calculate σ_T without having to rely on sensitisation experiments, where the fraction of T_1 that successfully energy transfer from a sensitizer to the target molecule can be difficult to quantify. The absorption spectrum of the PS:Y6 1:1.2 film investigated is given in Fig. S41: this film was excited at 800 nm with a high fluence of 16.1 μJ cm^{-2} (32.2 nJ per pulse) to create a significant population of S_1 from which ISC can potentially occur. As A = 0.57 at 800 nm, the number of S_1 generated is 5.57 x 10^{13}. By 1.8 ns, all S_1 states will have decayed, therefore any remaining population at this time will be solely T_1. This is confirmed by the absence of the S_1 PIA at 1550 nm and the presence of only the Y6 T_1 PIA at 1450 nm. Through comparing the relative intensity of the remaining Y6 GSB at 1.8 ns to the initial value, we determine that ~3% of the Y6 S_1 have undergone ISC to T_1. Therefore, the T_1 population at 1.8 ns is 1.67 x 10^{12}. As $\frac{\Delta T}{T}$ = -5.70 x 10^{-4} at the peak of the T_1 PIA at 1450 nm at 1.8 ns, we obtain σ_T = 3.42 x 10^{-16} cm^2 at 1450 nm from equation 2.

The values of σ_C and σ_T calculated were then used to determine N_T and N_C, using a film thickness of 90 nm for the optimised PM6:Y6 blend. We then input these values into equation 1 and fitted the TA kinetics globally over four different fluences (Fig S37). We note that kinetics following selective excitation of Y6 at 800 nm were used to simplify the charge transfer dynamics; as hole transfer from Y6 to PM6 is completed by 100 ps (Fig. S12), the data is analysed from this time onwards. From this, values of α = 0.91±0.03 and β = 8.03±0.20 x 10^{-9} cm^3 s^{-1} were obtained, confirming that ~90% of charges recombine via the Y6 T_1.

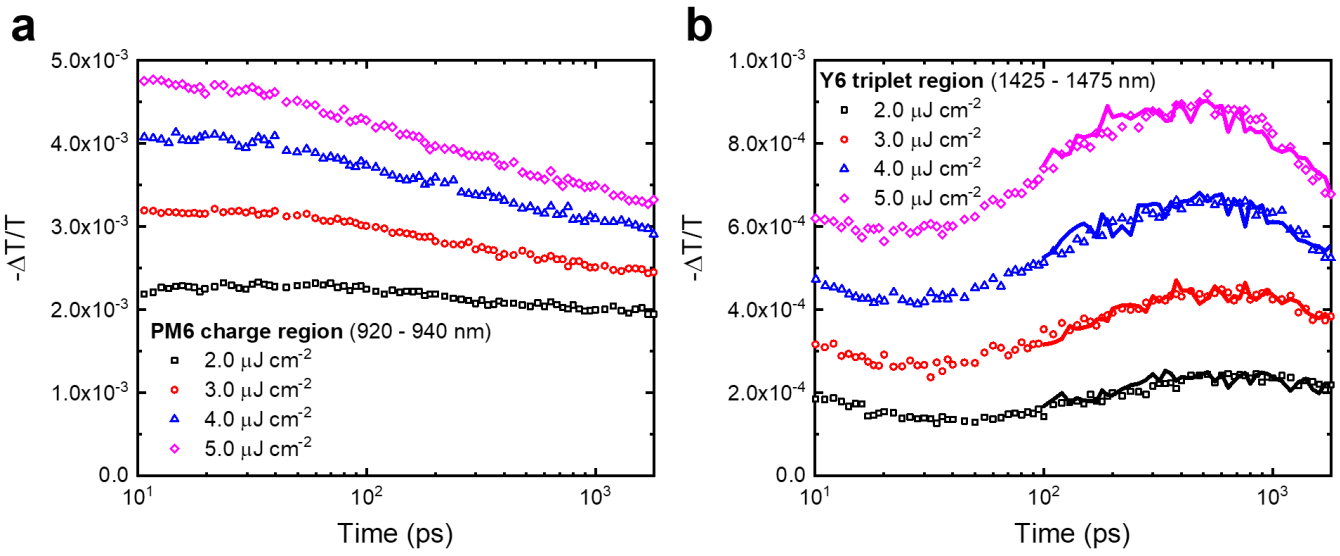

Figure 37: (a) The TA kinetics of the PM6:Y6 blend following selective excitation of Y6 at 800 nm at 293 K, taken around the maximum of the PM6 charge PIA between 920 – 940 nm. The PIA intensity, and therefore population, of the PM6 charges can be seen to decrease between 10 – 1800 ps. The loss of charges is significantly faster at higher excitation fluences, indicating non-geminate processes are responsible. This data was used as an input to the model described in equation 2. **(b)** The TA kinetics of the PM6:Y6 blend following selective excitation of Y6 at 800 nm at 293 K, taken around the maximum of the Y6 T_1 PIA between 1425 – 1475 nm. The rate and timescales over which charges are lost is clearly correlated with the increase of the Y6 T_1 population, indicating that the processes are related. The loss of Y6 T_1 population on timescales of 100's ps is due to the rapid triplet-charge annihilation occurring. The solid lines are global fits to the data using the model described in equation 2. As hole transfer from Y6 to PM6 is not completed until 100 ps (Fig. S12), as determined by an extremely low fluence measurement free from non-geminate recombination during the experimental time window, the data is only fitted for times >100 ps. Excellent agreement between the model and experimental data is obtained, revealing that ~90% of charges decay into T_1 on Y6.

For PTB7-Th:IEICO-2F, we have shown that T_1 formation is not a measurable loss pathway. However, it is important to be able to put an upper bound on the fraction of excited states that could recombine via the IEICO-2F T_1 without being detected. With this in mind, we note that the smallest signal we can reliably detect in our TA measurements is $\frac{\Delta T}{T}$ = 1 x 10^{-5} at 1350 nm (Fig. S43c). Therefore, in order to not be observed, the absorption by T_1 states on IEICO-2F must result in a signal lower than this baseline value. We begin by determining σ_T for IEICO-2F. Using A = 0.32 at 800 nm for our PS:IEICO-2F film (Fig. S43b) and an excitation fluence of 4.41 μJ cm^{-2} (17.0 nJ per pulse), we calculate the initial S_1 population after excitation to be 9.26 x 10^{12}. Assuming the T_1 yield is 5% (Fig. S35d), the number of T_1 states present at 1.8 ns after all S_1 have decayed is 4.63 x 10^{11}. From this population and a signal intensity of 4.1 x 10^{-4} at 1.8 ns in the NIR region TA of PS:IEICO-2F (Fig. S43d), we calculate σ_T = 8.86 x 10^{16} cm^2 for IEICO-2F (equation 2). Using this σ_T, the number of IEICO-2F T_1 states that would give a signal of 1 x 10^{-5} is 1.13 x 10^{10}. Turning now to the PTB7-Th:IEICO-2F blend; after excitation at 620 nm with a fluence of 3.80 μJ cm^{-2} (7.6 nJ per pulse), we calculate that 5.52 x 10^{12} S_1 states are formed, using A = 0.46 at 620 nm (Fig. S43a). From the ratio of the number of S_1 states formed (7.79 x 10^{12}) and the smallest number of IEICO-2F T_1 detectable (1.13 x 10^{10}), we determine that for T_1 formation not to be observed, the fraction of recombination proceeding via the IEICO-2F T_1 must be less than 0.15%.

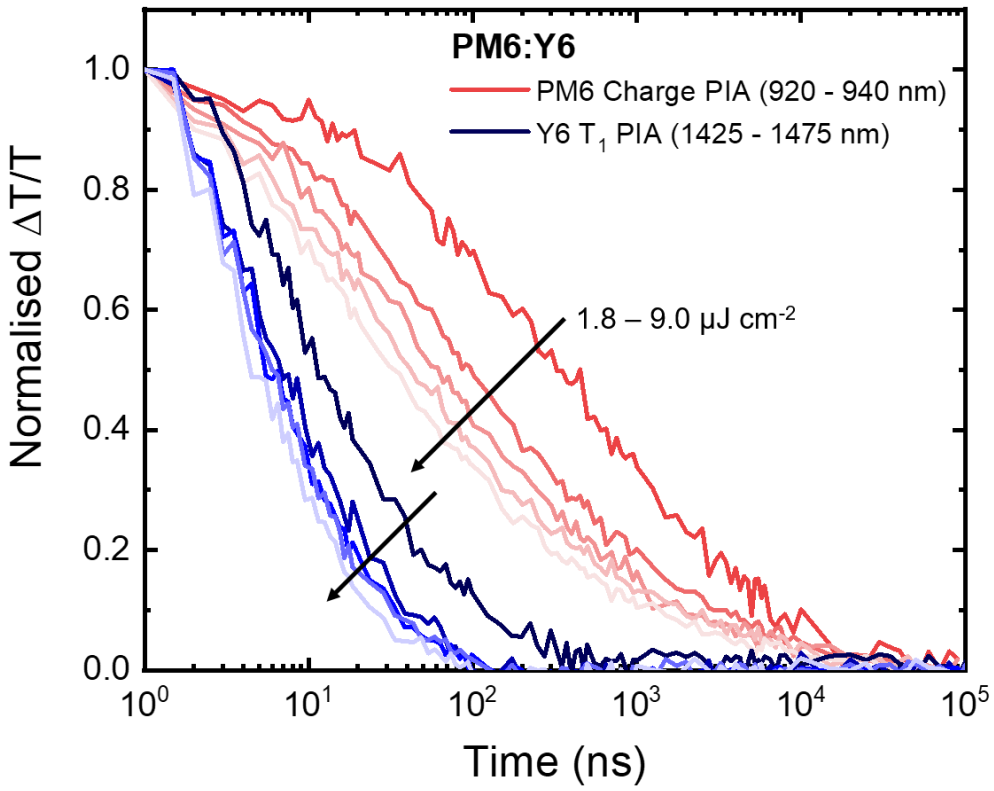

Figure S38: The ns-TA kinetics taken from the PM6 charge (red lines, 920 – 940 nm) and Y6 T_1 (blue lines, 1425 – 1475 nm) PIAs of a PM6:Y6 film, pumped at 532 nm for preferential PM6 excitation. A fluence series was performed, with fluences of 1.8, 3.6, 5.4, 7.2 and 9.0 μJ cm^{-2} used. We note that if a significant amount of triplet-triplet annihilation (TTA) was occurring, we would expect an increase in the number of charges over the timescales of T_1 quenching[18]. This is because TTA forms one S_1 state from two T_1 states, with the S_1 able to undergo charge transfer again, increasing the charge population. However, we clearly notice no increase in the PM6 charge PIA intensity over the timescales of 1 – 100 ns when T_1 quenching is taking place. From this, we conclude that the primary T_1 quenching route in our PM6:Y6 blend is via triplet-charge annihilation (TCA). Therefore, in order to avoid over-parameterisation, we introduce TCA as the only T_1 quenching pathway in our modelling of the T_1-charge dynamics. The validity of only including TCA is confirmed by the excellent agreement between the modelling and experimental data.

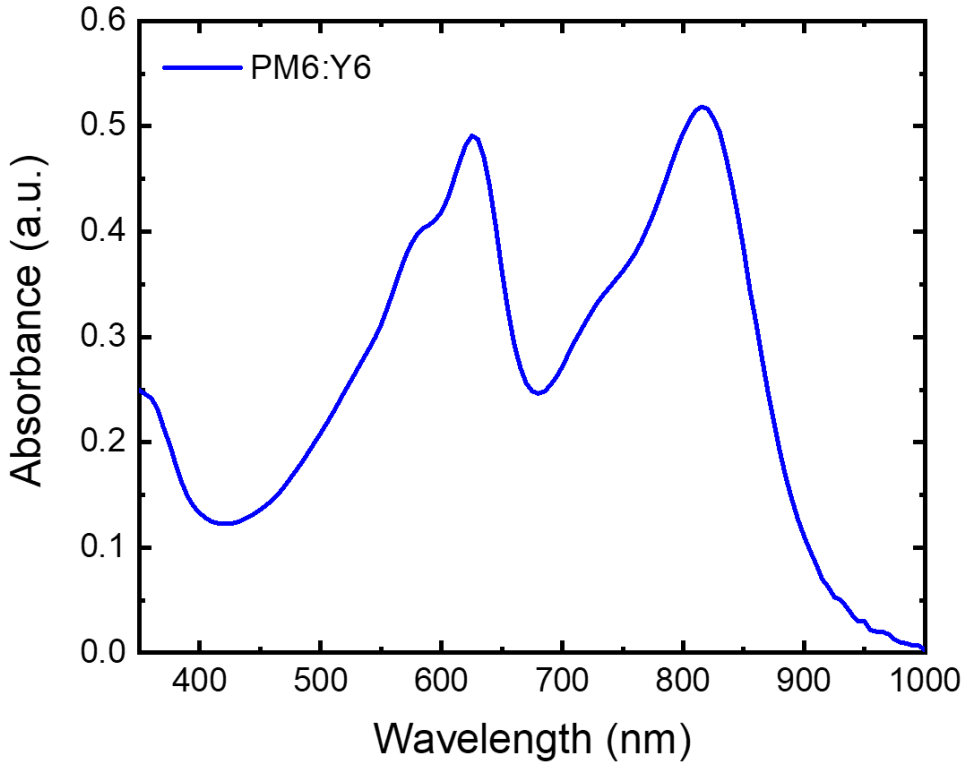

Figure S39: The absorbance spectrum of the PM6:Y6 film used in the TA measurements. This film was fabricated in an identical fashion to the optimised devices. The absorbance of the film at 800 nm is 0.49 and the thickness is 90 nm.

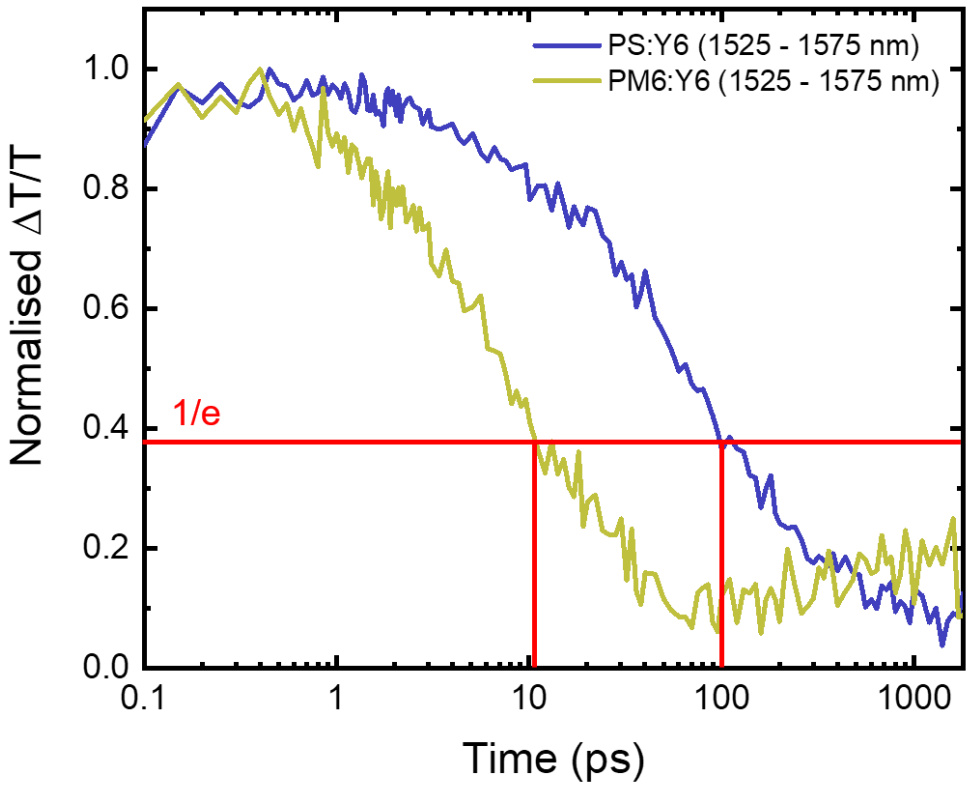

Figure S40: The TA kinetics of the Y6 S_1 PIA region (1525 – 1575 nm) in a PS:Y6 1:1.2 and PM6:Y6 film, excited at 800 nm with fluences of 1.8 and 1.0 μJ cm^{-2}, respectively. The time taken for the magnitude of the Y6 S_1 PIA to fall to 1/e in the PS:Y6 film is ~100 ps, whilst the time taken in the PM6:Y6 films is ~10 ps. From the ratio of these two lifetimes, η_{CT} is estimated to be ~90%. The slight rise in the blend signal after 100 ps is due to the kinetic also capturing the edge of the Y6 T_1 PIA at 1450 nm.

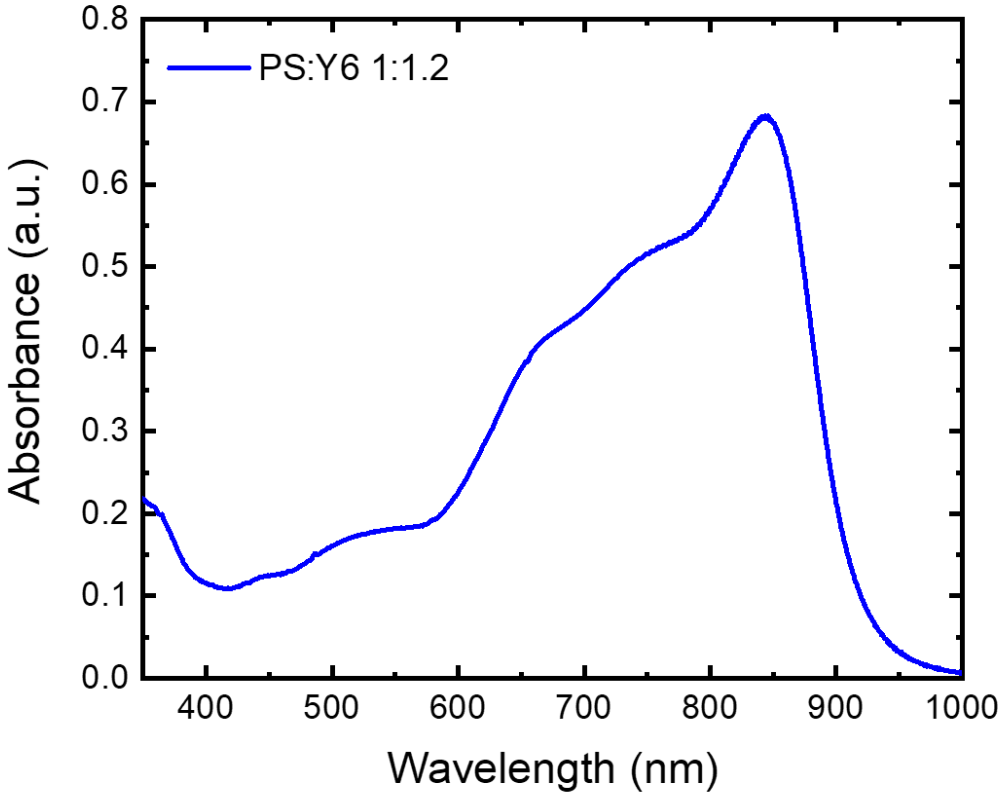

Figure S41: The absorbance spectrum of the PS:Y6 1:1.2 film used in the TA measurements. The absorbance of the film at 800 nm is 0.57.

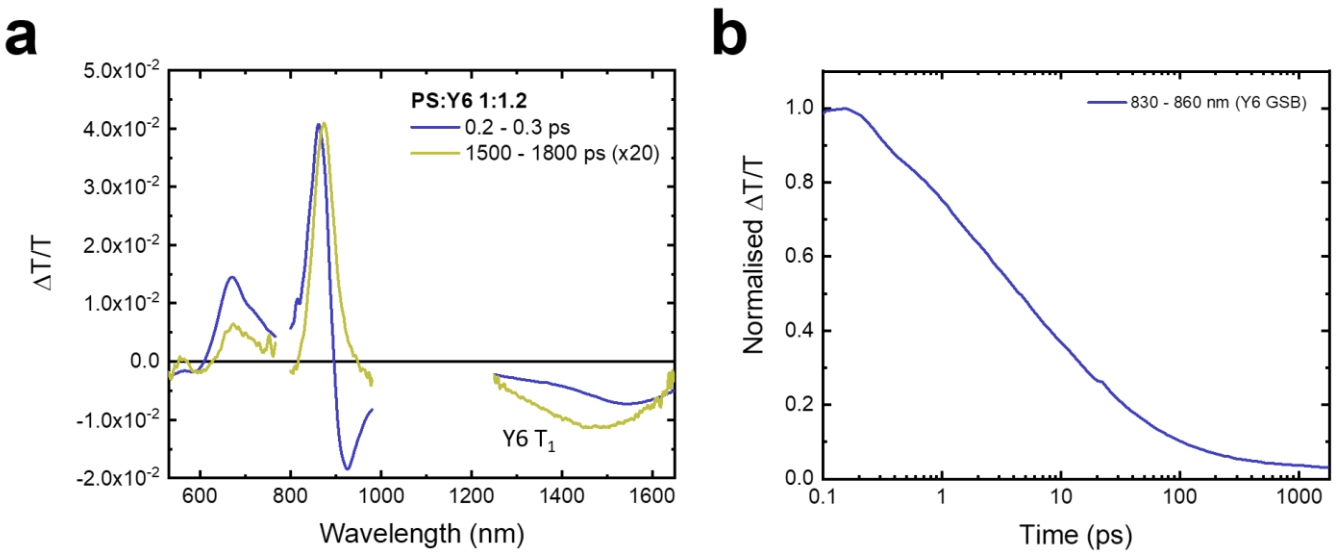

Figure S42: (a) The TA spectra of a PS:Y6 1:1.2 film, excited at 800 nm with a high fluence of 16.1 μJ cm^{-2} (pulse energy = 80 nJ). At 0.2 ps, the Y6 GSB is visible between 600 – 900 nm, with two distinct vibronic peaks. There are two Y6 S_1 PIAs in the NIR region: one sharp peak adjacent to the Y6 GSB at 910 nm and a weaker, broad feature peaked at 1550 nm. By 1.8 ns (scaled by a factor of 20 for clarity), the Y6 S_1 PIA has fully decayed, leaving behind only the Y6 T_1 PIA at 1450 nm. Therefore, we assume that any remaining GSB can be solely attributed to Y6 molecules bleached by triplet excitons. This allows us to determine the population of Y6 excited states remaining in the film and therefore σ_T. The intensity of the Y6 T_1 at 1.8 ns is -5.70 x 10^{-4} at 1450 nm. **(b)** The kinetic of the Y6 GSB region. As the sharp Y6 S_1 PIA band at 920 nm overlaps with the peak of the GSB at 870 nm, we have analysed the GSB between 830 – 860 nm to provide a better estimate of the fraction of Y6 excited states remaining at 1.8 ns. We find this value to be ~3% from the ratio of the maximum GSB signal intensity just after excitation.

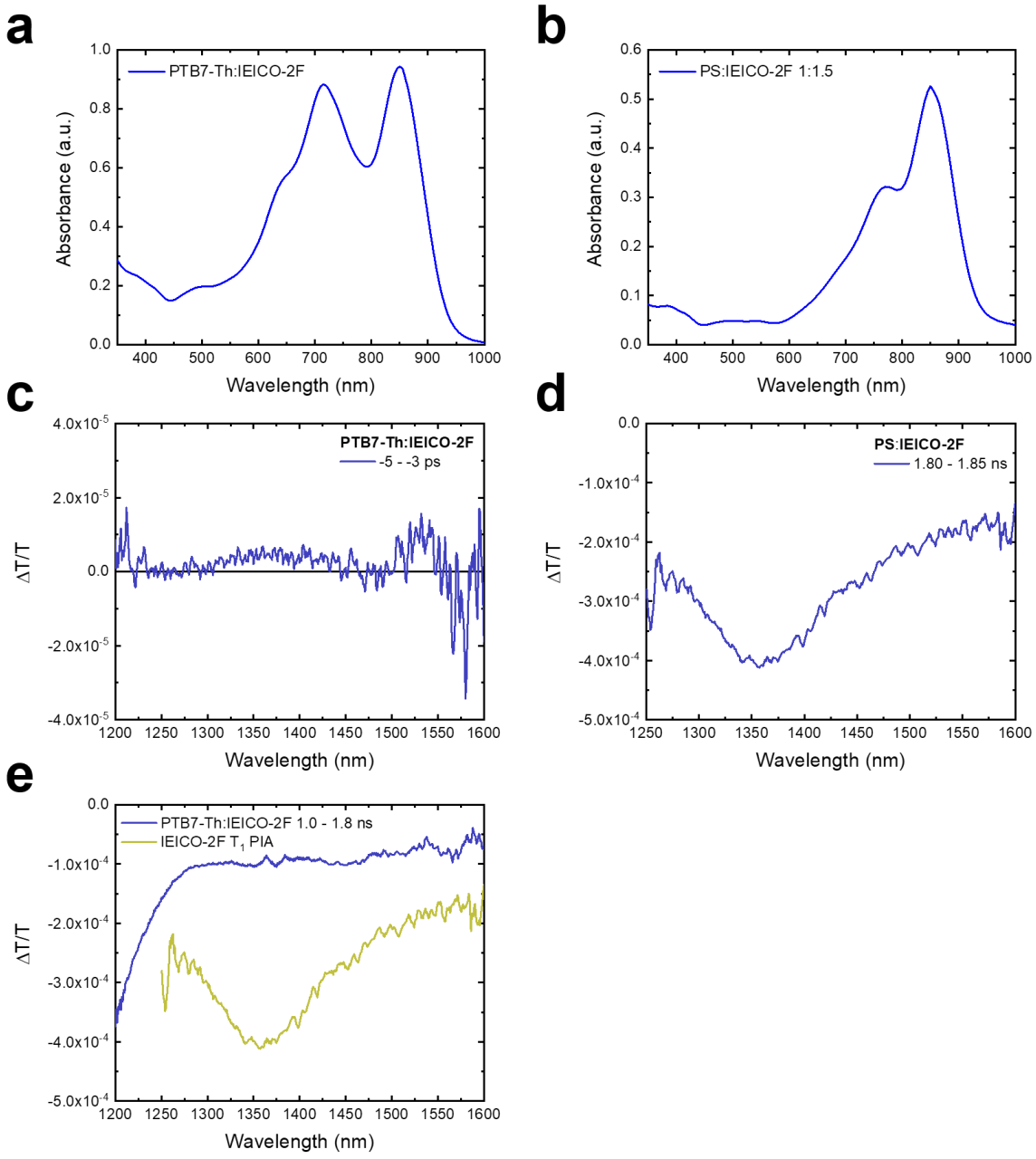

Figure S43: (a) The absorbance spectrum of the PTB7-Th:IEICO-2F film used in the TA measurements. This film was fabricated in an identical fashion to the optimised devices. The absorbance of the film at 620 nm is 0.27 and the thickness is 90 nm. **(b)** The absorbance spectrum of the PS-Th:IEICO-2F 1:1.5 film used in the TA measurements. The absorbance of the film at 800 nm is 0.32. **(c)** The baseline averaged between -5 and -3 ps for the measurement of the PTB7-Th:IEICO-2F blend that is displayed in the main text (Fig. 2d). From this, we assess that the smallest signal reliably resolvable around 1350 nm is 1 x 10^{-5}. **(d)** The TA spectra at 1.80 – 1.85 ns of a PS:IEICO-2F 1:1.5 film, pumped at 800 nm with a fluence of 4.41 μJ cm^{-2} (pulse energy = 17 nJ). The remaining signal is attributed to the IEICO-2F T_1

formed after ISC. From this, we calculate σ_T = 8.86 x 10^{16} cm^{-2} for IEICO-2F. **(e)** The TA spectra of PTB7-Th:IEICO-2F after excitation at 620 nm with a fluence of 3.80 μJ cm^{-2}. At 1.0 – 1.8 ns, there is no observable PIA band at 1350 nm that would correspond to the IEICO-2F T_1. The IEICO-2F T_1 PIA, taken from Fig. S43d, is overlaid for clarity.

Theory of triplet excited states studied by trEPR spectroscopy

Triplet states consist of two strongly coupled unpaired electrons that can be described by a spin Hamiltonian including the exchange term and the dipole-dipole term[21–23]. The exchange term depends exponentially on the distance of the two unpaired electrons, while the dipole-dipole term follows an inverse cubed dependence[21]. Since molecular triplet states are characterized by a short distance between the two unpaired electrons, the exchange term usually overwhelms the dipolar term and completely separates the energy levels of the triplet and singlet states[21]. As a result, the triplet sublevels of molecular triplet states are not "mixed" with the singlet level and therefore the exchange term is usually neglected in the simulation of molecular triplet states. The dipole-dipole term energetically splits the three sublevels of a triplet state even in the absence of an externally-applied magnetic field: it is also referred to as the Zero-Field Splitting (ZFS) interaction[21,22]. The eigenvalues of the ZFS Hamiltonian (X, Y and Z) are commonly expressed in terms of the ZFS parameters D and E that are defined as D = -3/2Z and E = 1/2(Y-X)[22]. The D parameter defines the strength of the dipolar coupling and is directly related to the delocalization of the triplet state, whilst the E parameter represents the deviation of the triplet delocalization from axial symmetry. It is important to note that the EPR line position depends only on the relative sign of D and E and therefore the absolute sign is often unknown.

Standard trEPR spectroscopy is carried out under the presence of an external magnetic field (about 340 mT). Therefore, to simulate the trEPR spectra of triplet states, both the electronic Zeeman and the dipole-dipole terms should be considered:

$$H = \mu_B \boldsymbol{B_0 g S} + \boldsymbol{SDS} \tag{3}$$

where $\boldsymbol{g}$ is the Zeeman g-tensor and $\boldsymbol{D}$ is the ZFS tensor, $\boldsymbol{B_0}$ is the external magnetic field vector, $\boldsymbol{S}$ is the spin operator, and μ_B is the Bohr magneton. In the high-field approximation, the spin sub-levels of the triplet state are commonly referred to as T_+, T_0 and T_- and their eigenvalues depend on the relative strength between the Zeeman and ZFS interactions and the direction of the magnetic field. For every molecular orientation, there are two allowed transitions between the three triplet sublevels ($\Delta m_s = \pm 1$) that correspond to two peaks in the trEPR spectrum. Their magnetic field position is determined by the eigenvalues of the spin Hamiltonian, while their intensity is determined by the spin-polarization mechanism, as discussed below. In a disordered material, such as the organic layers studied in this work, the

full trEPR spectrum can be calculated as the convolution of the contributions from all the randomly oriented molecules in the film. This is commonly referred to as a *powder spectrum*.

An interesting aspect of trEPR spectroscopy of triplet states is that although the instrument response is typically a few hundred ns, trEPR spectra allow us to obtain information about the photophysical processes that led to the creation of the observed triplet states, even if they occurred faster than the intrinsic experimental time resolution; this is due to the phenomenon of spin-polarization[24]. Spin-polarization occurs because the triplet states that are generated after a short laser pulse are far from thermal equilibrium, leading to trEPR spectra that show signals of enhanced absorption (*a*) and emission (*e*). This spin polarization pattern allows us to determine whether the triplet has been generated by an intersystem crossing (ISC) mechanism or a geminate back-charge transfer (BCT) process[24].

ISC from S_1 to T_1 is promoted by the spin-orbit interaction and is characterized by a strong anisotropy of the populating rates of the three triplet sublevels (m_s = -1,0,+1). ISC triplets can have several different spin polarization patterns, namely *aaaeee*, *eeeaaa*, *eeaeaa* and *aaeaee*[24]. Geminate BCT can be understood in the framework of the "spin correlated radical pair (SCRP) mechanism"[25–28]. The standard geminate recombination pathway starts from the ^1CT state, which in EPR spectroscopy is termed a spin-correlated radical pair (SCRP) due to the strong magnetic interactions between the two unpaired spins of the CT state. Distinct from localized molecular excited states, the $^1CT_0$ and $^3CT_0$ spin sublevels of a SCRP are "mixed" together because of hyperfine and electron Zeeman interactions. Thus, two distinct pathways can lead to the presence of BCT triplet polarisation patterns:

(i) The SCRP $^3CT_0$ sublevel formed by mixing with the $^1CT_0$ undergoes a spin-allowed BCT to an energetically low-lying molecular triplet T_0 state, generating an excess spin population in the T_0. This results in a spin polarisation pattern of *aeeaae* (D<0) or *eaaeea* (D>0) for the triplet exciton[24].

(ii) The mixing of the $^1CT_0$ and $^3CT_0$ SCRP sublevels opens a spin-allowed recombination pathway for $^3CT_0$ to the S_0 ground state via $^1CT_0$. This process results in an excess population remaining in the $^3CT_+$ and $^3CT_-$, which undergo a spin-allowed BCT to the molecular triplet T_+ and T_- sublevels, generating an excess spin population in the T_+ and T_-. This results in a spin polarisation pattern of *aeeaae* (D>0) or *eaaeea* (D<0) for the triplet exciton[24].

As a matter of clarity, molecular triplet states generated by non-geminate BCT cannot be detected by trEPR spectroscopy due to the lack of spin-polarization; the spin-statistical recombination of uncorrelated FCs results in an equal population of the $^1CT_0$, $^3CT_+$, $^3CT_0$ and $^3CT_-$. As a result, trEPR spectroscopy is well-suited as a complementary technique to the TA experiments, which can definitively confirm the presence of non-geminate BCT triplet excitons through the fluence dependence of the triplet formation.

Partial preferential order of triplet states

EPR spectroscopy allows for the detection of preferential molecular ordering as the EPR spectrum depends on the orientation of the paramagnetic species inside the magnetic field of the spectrometer. This effect arises from the anisotropy of spin interactions. As a result, in samples with some degree of molecular order, the EPR spectrum deviates from the "random" powder spectrum and a non-uniform distribution of molecular orientations, $P(\theta, \phi)$, should be considered to reproduce the spectral shape.

Specifically, the EPR intensity of partially oriented spectra at each field position can be calculated by the following integral performed over the all possible orientations[21,29]

$$I(B) = \sum_{\pm} \iint G\left(B - B_{res\pm}(\theta, \phi)\right) \cdot p_{\pm}(B, \theta, \phi) \cdot P(\theta, \phi) \cdot sin(\theta) d\theta d\phi \qquad (4)$$

Here, the summation is over the two transitions ($\Delta M_S = \pm 1$), $G(B - B_{res\pm}(\theta, \phi))$ is a Gaussian function centered at the resonance field $B_{res\pm}(\theta, \phi)$, and $p_{\pm}(B, \theta, \phi)$ is the population difference between the two triplet sublevels involved in the $\Delta M_S = \pm 1$ transitions, which determines the transition probability.

In our manuscript, we carried out all the EPR measurements by keeping the sample substrates parallel to the magnetic field. Given the disordered nature of our organic semiconductor samples, it is possible there is a small contribution to our measured spectra. However, we find that partial order is largely not required to obtain a satisfactory simulation of most of the spectra presented in our work.

The impact of temperature on the trEPR results

It is worth noting that standard trEPR experiments of organic semiconducting films are commonly performed at low temperatures (~80 K) to slow down the spin relaxation processes, which results in improved signal-to-noise. Therefore, it is important to consider whether the low temperature may affect the photo-generation dynamics. In the systems studied, ISC triplets are formed from singlet excitons that do not reach the D/A interface for charge transfer. In relation to this, we note that the low temperatures used will reduce the non-radiative vibrational relaxation of singlet excitons[30], allowing more time for ISC to occur before exciton decay; this provides a route for enhanced ISC triplet yields at the low temperatures in the trEPR measurements. We note that this increased ISC triplet yield may be balanced out by a reduction in the ISC efficiency, as ISC can be a thermally activated process[31]. However, it is not clear if this is the case in the materials studied in our work. All things considered, at room temperature where vibrational decay can occur rapidly, we believe that the presence of a significant amount of ISC triplets is unlikely[32], as most un-dissociated singlets will decay directly to the ground state. When contemplating the potential formation of geminate BCT triplets at room temperature in NFA OSCs, we note that the charge separation can take up to 100 ps[1,33,34]. It is thus reasonable to assume charge separation takes place via thermalized CT states[15,16]. Therefore, charge separation likely occurs via a thermally-assisted hopping mechanism and will be slower at low temperatures[35,36], though we note one report has claimed little dependence on the efficiency of charge separation with temperature for a PM6:Y6 blend[20]. In light of this we consider that, if anything, BCT triplet formation is more likely to take place at low temperature due to the slower charge separation timescales providing more opportunity for the mixing of $^1CT_0$ and $^3CT_0$; this typically takes place on ~ns timescales[37,38]. Therefore, if BCT triplets are not present at 80 K in the NFA blends, they are exceedingly unlikely to then be present at room temperature.

trEPR experimental details

All the time-resolved EPR spectra reported in our manuscript were recorded by adopting a direct-detection scheme, which is depicted below:

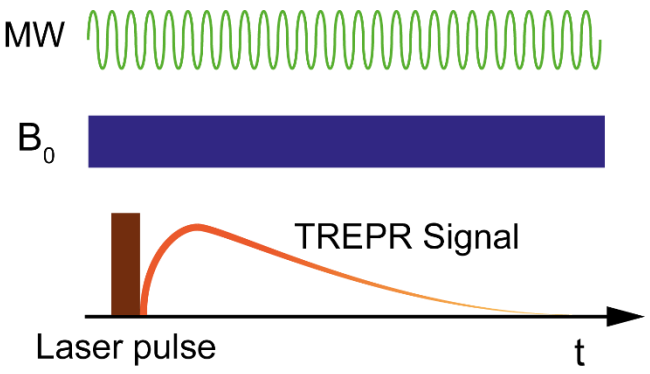

A schematic representation of a continuous-wave time-resolved EPR experiment. For each value of the external magnetic field, the EPR intensity is recorded as a function of the time after excitation by a laser pulse under continuous X-band microwave radiation.

Specifically, in reference to the trEPR scheme, the EPR intensity is recorded as a function of time following pulsed laser excitation (laser pulse), with constant applied X-band microwave radiation (MW), for each externally applied magnetic field position ($\mathbf{B_0}$). The trEPR signal is recorded through a transient recorder with timing synchronisation by a delay generator. This technique enables the time-evolution of the EPR signal of a photoinduced species to be recorded from a few hundred nanoseconds (the overall response time of our set-up is about 200 ns) to several microseconds[39].

The magnetic field is swept to cover the entire range of resonances. For each field point, the EPR signal is accumulated multiple times to obtain the desired signal-to-noise ratio (SNR, usually 400 averages per point). The resulting dataset is a two-dimensional matrix containing the intensity of microwave absorption as a function of both the magnetic field and the time after the laser flash.

The raw data matrix consists of: (1) the actual EPR signal of the transiently photogenerated species, which is superimposed on; (2) the laser-induced field-independent background signal; (3) the signals of non-photogenerated species and stable (or long-lived) light-induced species. To isolate the actual EPR signal, it is therefore necessary to apply a baseline correction in both the time and field dimensions. First, we subtracted the transient signal offset, i.e. the mean value of the EPR response before the laser pulse (pre-trigger offset compensation), from each transient, to eliminate the contribution of the non-photogenerated species and the long-lived photo-induced components. Second, we filtered out the laser-induced background signal, which is independent from the magnetic field, by subtracting the off-resonance signal intensity from the spectra at each time point. Finally, to further increase the SNR, we averaged the reported trEPR signal on a time window of 1 µs.

trEPR simulation procedure

The acquired trEPR spectra have been simulated by using the core functions *pepper* and *esfit* of the open-source MATLAB toolbox EasySpin[40]. The parameters included in our best-fit simulations are the ZFS parameters (D and E), the triplet population sublevels (p_1, p_2, p_3) and the line broadening (assumed as only Lorentzian). To avoid over-parameterising the fitting, no Gaussian contribution has been included in our best-fit simulations. We also note that the Gaussian contribution was found to be insignificant with respect to the Lorentzian contribution and did not improve the quality of the fit. For the determination of the spin polarization, the populations of the spin-triplet sublevels at zero field were computed (T_x, T_y, T_z) in the fitting program and used by EasySpin to simulate the trEPR spectrum at resonant fields[40]. For all the simulations, the g tensor was assumed isotropic with g_{iso}=2.002.

The quality of the fit has been estimated by the NRMSD (Normalised Root Mean Square Deviation), which has been calculated with the following formula:

$$NRMSD = \frac{\sqrt{\frac{\sum_{i=1}^{n}(y_i - \hat{y})^2}{n}}}{y_{max} - y_{min}}$$

Where y_i is the i*th* observation of y (i.e. trEPR experimental signal) and $\hat{y}$ the predicted y value given the model (i.e. best-fit), n is the number of points of the spectrum and y_{max} and y_{min} are respectively the maximum and the minimum of the simulated species in the trEPR spectrum. This approach provides an estimate through which the fit quality of different datasets can be compared on a standardized scale."

To carry out our least-square fittings, a user-defined simulation function has been developed which allowed for the fitting of "non-spin system" parameters, such as the spin populations of the triplet sublevels. All the fits were carried out using a Nelder/Mead downhill simplex optimisation algorithm. The fitting results clearly demonstrate that the ISC contribution is adequate to simulate all the experimental spectra. This is confirmed by the residuals for the field regions where the triplets were simulated. The residuals have been reported together with the experimental spectra and the corresponding best-fit simulations below.

trEPR results summary

We have carried out trEPR spectroscopy to investigate in detail the structure and the dynamics of the excited triplet states in the NFA blends, as well as the neat materials. The trEPR spectra acquired at two or three different delay times after the laser pulse are reported in Figures S44 – S61, together with the best-fit spectral simulations and residual. In Table S2, we summarize the main results obtained from the spectral simulations. In Figure S62, we report the plots of the full 2D trEPR spectra for all the studied samples. In the following, we divide the trEPR results into two sections: (1) neat donor and acceptor films, and (2) NFA blends.

Neat donor and acceptor films

The trEPR spectra of the neat donor and acceptor films are characterized by the presence of up to two different signals (one spectrally-narrow and the other much broader) with a different time evolution. The narrow bandwidth EPR signal extends for a few mT and possesses a g-value and a polarization pattern (either in enhanced absorption or emission) which are typical of free charges generated upon photon absorption[41]. The detection of free charges highlights the capability of the neat materials to generate FC despite the absence of an electron-donor/acceptor counterpart[42]. This can be rationalized by the presence of electron-donor and -acceptor units within the polymer chain which favour the photo-induced charge transfer process (either intra- or inter-molecular)[42] and the subsequent charge separation of the CT state. In line with previous observations[43], the EPR signal of these photo-generated charges decays very rapidly (a few µs) due to the rapid charge recombination process occurring, even at low temperatures (80 K).

The broad EPR signal can be attributed to localized triplet excitons[24,44–46]. To confirm our hypothesis, we performed best-fit spectral simulations for all the studied samples that exhibited substantial triplet formation. However, the triplet signal in neat IEICO-2F, SiOTIC-4F, ITIC and IT-4F were too weak for successful simulation. The obtained spectroscopic parameters are summarised in Table S2. From the simulations, we obtained information about the zero-field splitting (ZFS) parameters and the non-equilibrium populations of triplet sublevels (spin polarization). These ZFS parameters are directly related to the delocalization and the symmetry of the triplet states[47]. The obtained ZFS parameters suggest that the observed triplet states are delocalized over few monomeric units (~1-2), in-line with other photovoltaic polymers in literature[21]. The spin polarization is related to the triplet populating

mechanism, which in our neat films is always ISC driven by spin-orbit interactions from S_1 to T_1[47]. The good ISC yields in the neat polymer films is due to the longer lifetimes of the singlet excitons at low temperature, resulting from a decreased rate of non-radiative vibrational decay[30].

It is worth mentioning that PM6 shows a slightly different behaviour; a third signal with different spectral features and time evolution is observed. From the spectral simulations, we conclude that this signal can be attributed to a second triplet state generated via ISC. Furthermore, the ZFS parameters of triplet 2 (Table S2) suggest it is more delocalized than triplet 1, which can be rationalized with the presence of a hybrid locally excited charge-transfer (HLCT) triplet state[48].

Finally, we noticed that some of the SOC-ISC triplets detected via trEPR show an inversion in the spin polarization pattern with time. This effect can be understood taking a closer look at the populating and decay rates of the triplet sublevels. In both cases, the populating and decay kinetic constants possess a similar mathematical description: $k_{\mu}^{pop} \propto \left|\left\langle \psi_{T_\mu} \middle| \boldsymbol{H_{ISC}} \middle| \psi_{S_1} \right\rangle\right|^2$ and $k_{\mu}^{dec} \propto \left|\left\langle \psi_{T_\mu} \middle| \boldsymbol{H_{ISC}} \middle| \psi_{S_0} \right\rangle\right|^2$. Since ψ_{S_1} and ψ_{S_0} possess similar symmetry, it is probable that the spin-population of the triplet levels that are populated more rapidly will also decay faster. As a result, the triplet polarization evolves with time, showing an inversion of the spin polarization pattern whilst retaining the same spectral shape[46].

NFA blends

All trEPR spectra of NFA blends, apart from J51:ITIC, are characterized by the presence of two main signals: one narrow and one broad. The narrow signal in the centre of the EPR spectrum can be attributed to charges photo-generated following photon absorption. This signal is more intense (relative to the triplet signal) in the blends than in the neat films because of the more efficient charge photo-generation. In PTB7-Th:IEICO-2F, PBDBT:ITIC, and J51:ITIC, the signal shows an interesting time evolution: at shorter times (1 μs), the *ea* polarization pattern typical of SCRP is observed. Notably, SCRPs are characterised by either *ea* or *ae* polarization patterns depending on the sign of the exchange interaction, J, and the spin multiplicity of the RP precursor state. The presence of SCRPs highlights that in these blends, the charges are still magnetically interacting at shorter times and are therefore not fully separated. At longer times (5 μs), the signal evolves into a single peak which can be explained by the spin-lattice relaxation generating thermal equilibrium spin populations of either SCRPs

or free (i.e. unbound) charges. However, the line width of the peak at 5 µs slightly decreases compared to the peak at 1 µs, which is likely due to a weaker dipolar interaction between the charges, which may further imply the presence of free thermalised charges. This observation suggests that in these three blends, the charge generation process at 80 K is slower compared to the other NFA blends, which also show only a single peak at shorter times. In contrast, the PM6:ITIC blend exhibits a SCRPs signal at both 1 and 5 µs, potentially indicating even slower charge generation. This is consistent with the relatively low performance observed in this blend.

The broader signal is attributed to triplet excitons generated via ISC from S_1 to T_1. In the studied NFA blends, this signal is much weaker compared to the pristine polymer films due to the faster singlet exciton quenching rates resulting from an efficient charge transfer process. The triplet excitons appear particularly weak in PTB7-Th:IEICO-4F and J51:ITIC, where no spectral simulation could be performed. For the other blends, we carried out the spectral simulations: importantly, by comparing the obtained ZFS values to those measured in the neat films, we could elucidate whether the detected triplets are localized on the donor or the acceptor (Table S2). In all PTB7-Th NFA blends, the observed triplet excitons are localized on the acceptor, whilst in contrast, the triplet is usually localised on the donor in the PM6 and PBDB-T blends, except for PM6:Y6. Furthermore, in PM6:ITIC and PM6:IT-4F blends, we detect two ISC triplets: this is consistent with the observations from the neat PM6 film. As demonstrated by the absence of ISC triplets in the TA measurements (with the exception of PTB7-Th:IEICO-0F), ISC triplets are unlikely to be observed at room temperature under normal device operating conditions[32].

Material class	Material	Triplet	[D E] (MHz)	Populations [p1 p2 p3]	Linewidth (mT)	NRMSD*	D or A?	Charges
Neat donor films	PM6 (1 µs)	ISC 1	[1410 125]	[0.28 0.36 0.36]	8.0	0.08	D	FC
	PM6 (5 µs)**	ISC 2	[135 0]	[0.34 0.43 0.23]	5.0	0.10**	D	FC
	PTB7-Th (1 µs)	ISC	[1100 160]	[0.12 0.43 0.45]	11.0	0.03	D	FC
	PTB7-Th (5 µs)	ISC	[1050 160]	[0.47 0.28 0.25]	8.0	0.04	D	FC
	PBDB-T (1 µs)	ISC	[1410 190]	[0.25 0.39 0.36]	8.0	0.10	D	FC
	PBDB-T (1 µs) +0.3 order	ISC	[1360 150]	[0.00 0.58 0.42]	10.0	0.09	D	FC
	J51 (1 µs)	ISC	[1390 210]	[0.00 0.45 0.55]	10.0	0.10	D	FC
Neat acceptor films	Y6 (1 µs)	ISC	[900 170]	[0.27 0.36 0.36]	8.6	0.06	A	
	ITIC	ISC (very weak)	no sim				A	FC
	IT-4F	ISC (very weak)	no sim				A	FC
	IEICO-2F	ISC (very weak)	no sim				A	CT
	SiOTIC-4F (1 µs)	ISC (weak)	no sim D=840 MHz				A	
Blend films	PM6:Y6 (1 µs)	ISC (weak)	[1280 240]	[0.31 0.37 0.32]	7.0	0.55	A***	FC
	PM6:ITIC (1 µs)	ISC	[1310 130]	[0.00 0.43 0.57]	11.5	0.30	D	CT
	PM6:ITIC (5 µs)	ISC	[140 0]	[0.34 0.32 0.34]	8.0	0.10	D	CT

	PM6:IT-4F (1 µs)	ISC	[1300 90]	[0.16 0.39 0.45]	14.0	0.18	D	FC
	PTB7-Th:IEICO-0F (1 µs)	ISC	[850 210]	[0.00 0.32 0.68]	10.4	0.20	A****	FC
	PTB7-Th:IEICO-2F (1 µs)	ISC	[850 190]	[0.12 0.43 0.46]	7.5	0.15	A****	CT -> FC
	PTB7-Th:IEICO-4F	ISC (very weak)	no sim					FC
	PTB7-Th:SiOTIC-4F (5 µs)	ISC	[920 210]	[0.41 0.31 0.28]	8.9	0.10	A****	FC
	PBDB-T:ITIC (1 µs)	ISC	[1380 220]	[0.00 0.37 0.63]	14.0	0.20	D	CT -> FC
	J51:ITIC	-						CT -> FC

* the NRMSD is affected by the presence of a polaron or CT state that is not included in the simulation.

** only the narrow triplet signal has been fitted. The larger NRMSD in this case results from the broader triplet feature that has not been simulated for this spectrum.

*** the D parameter in the blend is higher than in the neat film, possibly due to the tendency of Y6 to form more delocalised excitations in the more aggregated neat film environment where there is no polymer to disrupt the aggregation[2,49].

**** as [D E] for the triplet are very different to the donor polymer (PTB7-Th), the triplets have been assigned to the acceptor. However, as the triplet signals in the neat acceptors were weak, it is not possible to simulate them to confirm this assignment.

Table S2: A summary of the best-fit spectral simulations of the trEPR measurements reported in Figures S44 – S61. The samples are split into three categories: neat donor films, neat acceptor films and the blend films. For each blend, the ZFS parameters and the populating mechanism of the triplet states are reported. The ZFS parameters are given in absolute value units of MHz. From the ZFS parameters, we assigned the triplet either to the donor (D) or the acceptor (A). Populations order is from low-to-high energy zero-field states, Tz, Tx, and Ty, respectively, for D > 0

& E > 0. Only Lorentzian broadening was considered to not over-parametrize the fitting; the linewidth is reported in units of mT. The normalised root-mean-square-deviation (NRMSD) is also reported. Finally, the presence of charges (either a CT state or FC) is summarized.

Full trEPR results and discussion

PM6 film

The trEPR spectrum of the neat PM6 film at 1 μs after the laser pulse shows two features; a sharp peak at ~346 mT, which is a signature of polarons, and a broader signal between 290 – 410 mT, which is assigned to triplet excitons. As time progresses, the broader triplet signature largely disappears and a new, narrower triplet feature between 330 – 360 mT forms. From the best-fit simulation of the spectrum at 1 μs, an *eeeaaa* polarisation pattern, indicative of a triplet exciton formed via ISC, is observed. The [D E] parameters of the triplet state are [1410 125] MHz, typical of triplets delocalised over a few aromatic rings (localised excitons, LE). The simulation of the trEPR spectrum at 5 μs has only been performed for the spectrally narrower triplet. The narrower triplet has [D E] parameters of [135 0] MHz, which suggests that this triplet state is more delocalised than triplet 1 μs and may be attributed to triplet state with partial CT character.

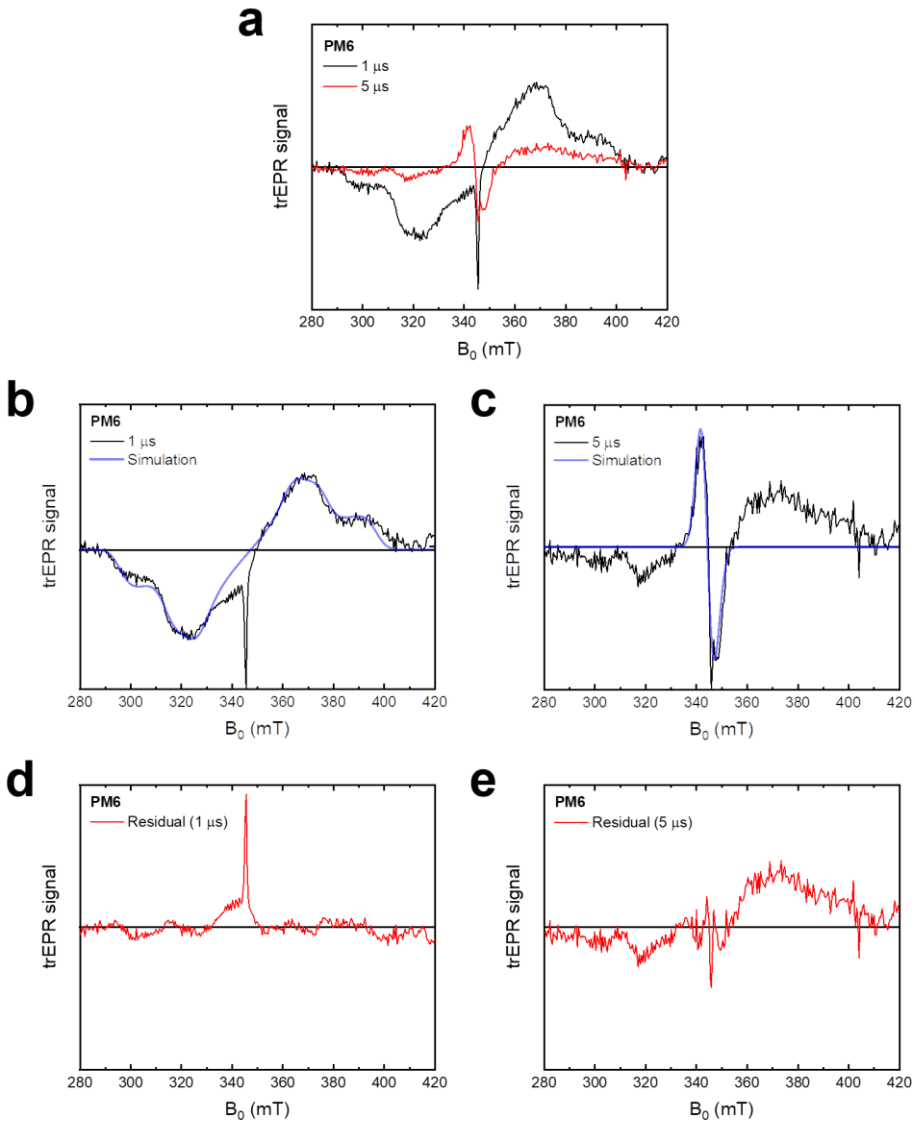

Figure S44: (a) The trEPR spectra of a neat PM6 film, taken at representative time points of 1 and 5 µs after excitation at 532 nm. Absorption (*a*) is up, emission (*e*) is down. **(b)** The trEPR spectra at 1 µs is shown, with the simulation overlaid. **(c)** The trEPR spectra at 5 µs is shown, with the simulation of the central, narrower triplet feature between 330 – 360 mT overlaid. **(d)** The residual from the best fit simulation in Fig. S44b, shown on the same y-axis scale. The residual (excluding the polaron region, which was not included in the simulation) indicates that the simulation describes the experimental spectrum well. **(e)** The residual from the best fit simulation in Fig. S44c, shown on the same y-axis scale. The residual in the 330 – 360 mT region of the narrower triplet feature (excluding the polaron region, which was not included in the simulation) indicates that the simulation describes the experimental spectrum well. The remaining residual is due to the presence of a more localised triplet exciton with a larger [D] parameter, likely the triplet observed at 1 µs in Fig. S44a.

PTB7-Th film

The trEPR spectrum of the neat PTB7-Th film (Fig. S45) at 1 µs shows a sharp peak at ~346 mT, which is a signature of free polarons, and a broader signal between 310 – 390 mT, which is assigned to triplet excitons. As time progresses, the triplet signal inverts. From the best-fit simulation at 1 µs, an *eeeaaa* polarisation pattern, indicative of a triplet exciton formed via ISC, is obtained. The [D E] parameters of the triplet state are [1100 160] MHz, typical of triplets delocalised over a few aromatic rings (LE). The simulation of the trEPR spectrum at 5 µs shows an *aaaeee* polarisation pattern, indicative of a triplet exciton formed via ISC. The [D E] parameters of the triplet state are [1050 160] MHz, very similar to those of the triplet observed at 1 µs. Thus, it is likely the same ISC triplet as visible at 1 µs but inverted. We attribute this to unequal decay rates from the three high-field triplet states[50].

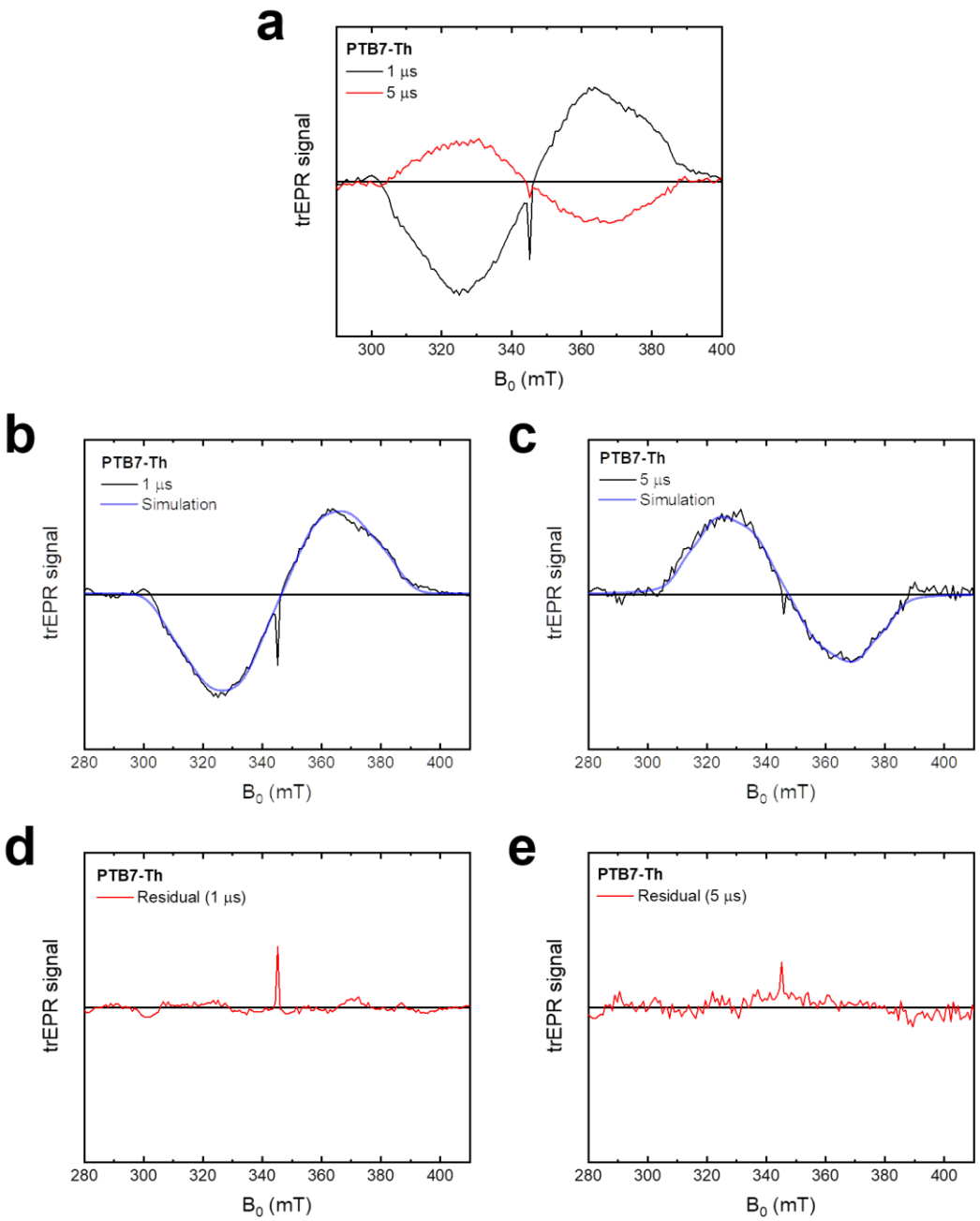

Figure S45: (a) The trEPR spectra of a neat PTB7-Th film, taken at representative time points of 1 and 5 µs after excitation at 532 nm. Absorption (*a*) is up, emission (*e*) is down. **(b)** The trEPR spectra at 1 µs is shown, with the simulation overlaid. **(c)** The trEPR spectra at 5 µs is shown, with the simulation overlaid. **(d)** The residual from the best fit simulation in Fig. S45b, shown on the same y-axis scale. **(e)** The residual from the best fit simulation in Fig. S45c, shown on the same y-axis scale. The residual (excluding the polaron region, which was not included in the simulation) indicates that the simulation describes the experimental spectrum well.

PBDB-T film

The trEPR spectrum of the neat PBDB-T film at 1 μs shows a pronounced and sharp polaron peak at ~346 mT, suggesting that the pathway to free charge generation is relatively efficient. In addition, there is a broad triplet signal between 290 – 400 mT. From the best-fit simulation without preferential ordering effects at 1 μs (Fig. S46b), an *eeeaaa* polarisation pattern, indicative of a triplet exciton formed via ISC, is obtained. The [D E] parameters of the triplet state are [1410 190] MHz, typical of triplets delocalised over a few aromatic rings. We note that there is still some structured residual around the baseline from the simulation without preferential ordering effects, so to improve the quality of the simulation, we have including a preferential ordering of +0.3 (Fig. S46c).

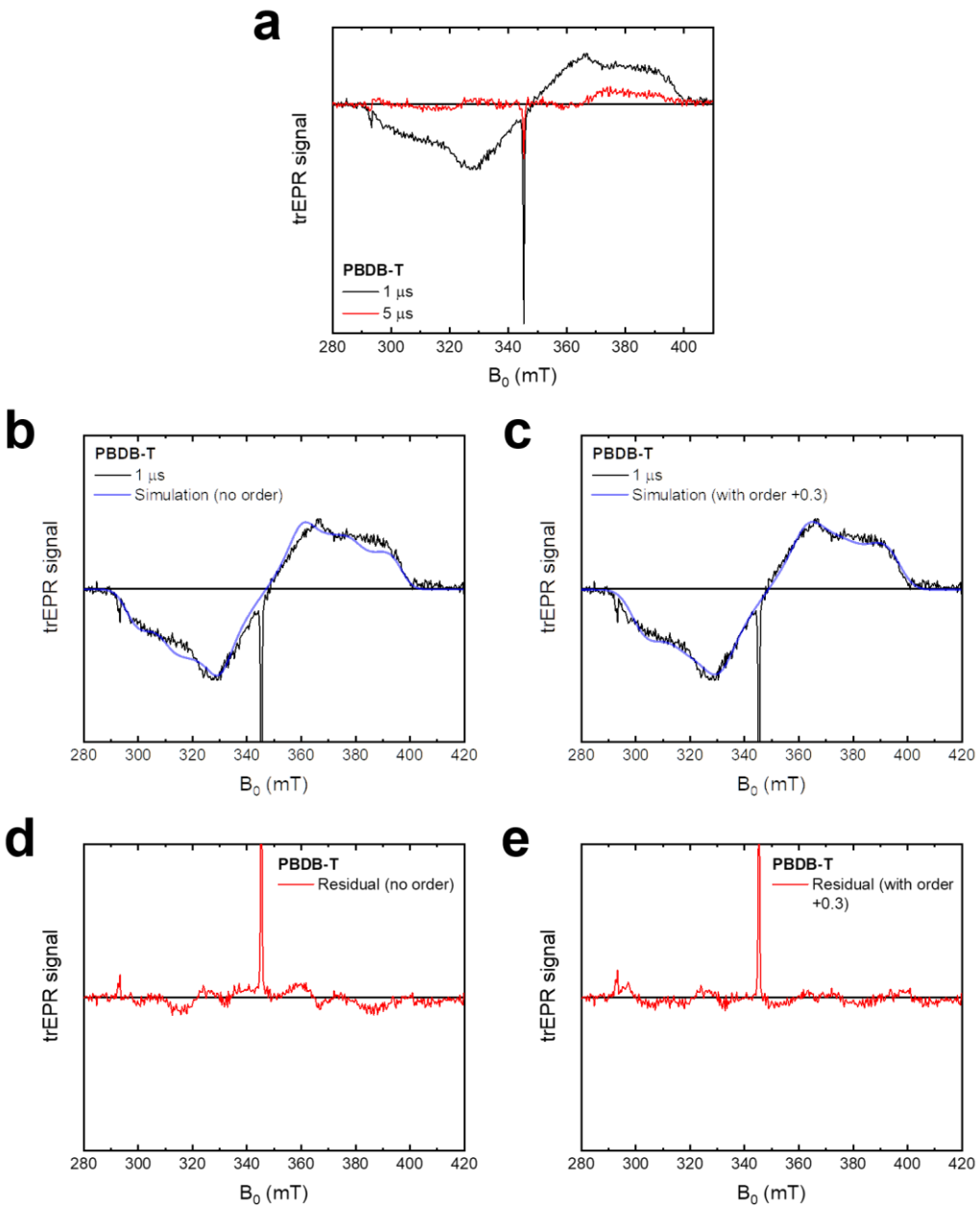

Figure S46: (a) The trEPR spectra of a neat PBDB-T film, taken at representative time points of 1 and 5 µs after excitation at 532 nm. Absorption (*a*) is up, emission (*e*) is down. **(b)** The trEPR spectra at 1 µs is shown, with the simulation overlaid. An *eeeaaa* polarisation pattern, indicative of a triplet exciton formed via ISC, is obtained. In this simulation, no preferential ordering is used. **(c)** The trEPR spectra at 1 µs is shown, with the simulation, now including an ordering parameter (+0.3), overlaid. An *eeeaaa* polarisation pattern, indicative of a triplet exciton formed via ISC, is obtained. **(d)** The residual from the best fit simulation in Fig. S46b, shown on the same y-axis scale. Though the residual is small, there is some structure remaining, which may indicate that the simulation does not fully describe the triplet. **(e)** The residual from the best fit simulation in Fig. S46c, shown on the same y-axis scale. The residual is slightly reduced by including the preferential ordering parameter, indicating a better fit.

J51 film

The trEPR spectrum of the neat J51 film at 1 µs shows a sharp peak at ~346 mT, which is a signature of free polarons. Additionally, there is a broad signal between 290 – 400 mT, which is assigned to triplet excitons. From the best-fit simulation of the spectrum at 1 µs, an *eeeaaa* polarisation pattern, indicative of a triplet exciton formed via ISC, is obtained. The [D E] parameters of the triplet state are [1390 210] MHz, typical of triplets delocalised over a few aromatic rings. The triplet signal decays over time with no change in its ZFS values, suggesting that no further triplet populating pathways are present.

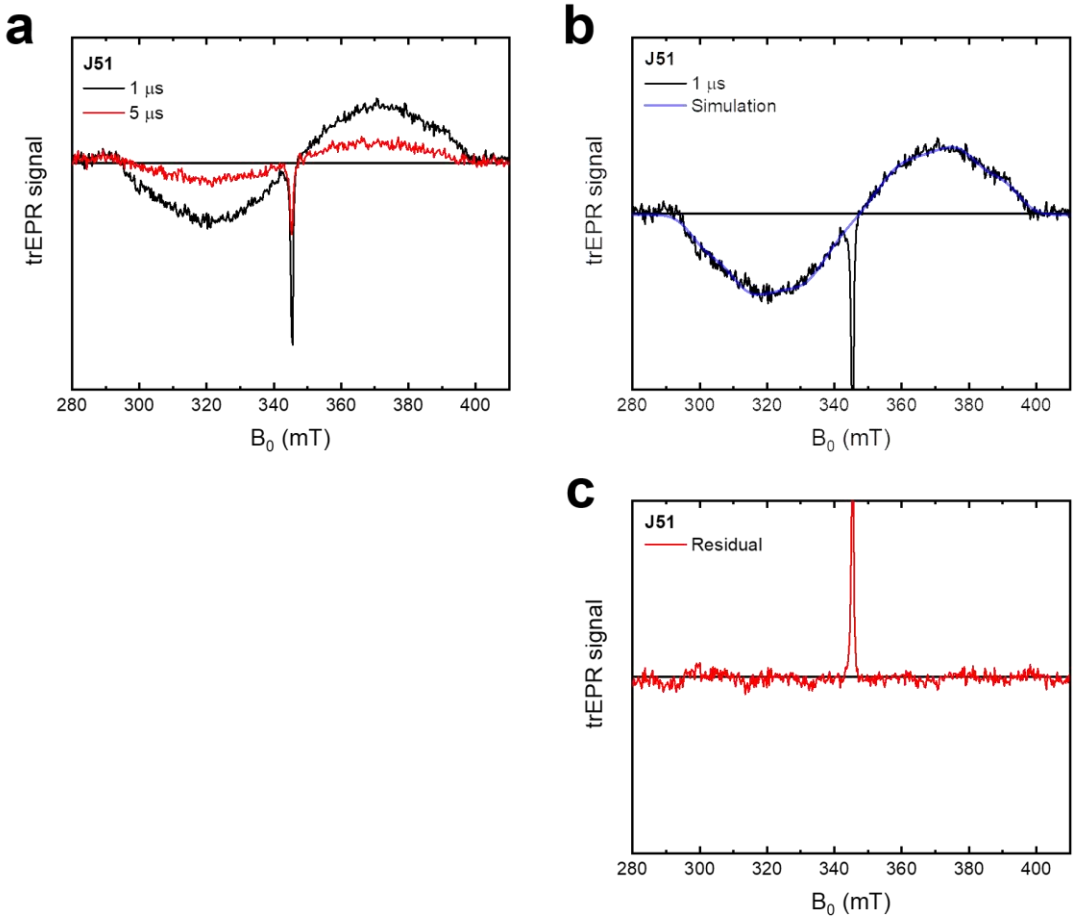

Figure S47: (a) The trEPR spectra of a neat J51 film, taken at representative time points of 1 and 5 µs after excitation at 532 nm. Absorption (*a*) is up, emission (*e*) is down. **(b)** The trEPR spectra at 1 µs is shown, with the simulation overlaid. An *eeeaaa* polarisation pattern, indicative of a triplet exciton formed via ISC, is obtained. **(c)** The residual from the best fit simulation in Fig. S47b, shown on the same y-axis scale. The residual (excluding the polaron region, which was not included in the simulation) indicates that the simulation describes the experimental spectrum well.

Y6 film

The trEPR spectrum of the neat Y6 film at 1 µs shows a broad signal between 310 – 380 mT, which is assigned to triplet excitons. From the best-fit simulation of the spectrum at 1 µs, an *eeeaaa* polarisation pattern, indicative of a triplet exciton formed via ISC, is obtained. The [D E] parameters of the triplet state are [900 170] MHz, typical of triplets delocalised over a few aromatic rings. The triplet signal decays over time with no change in its ZFS values, suggesting that no further triplet populating pathways are present.

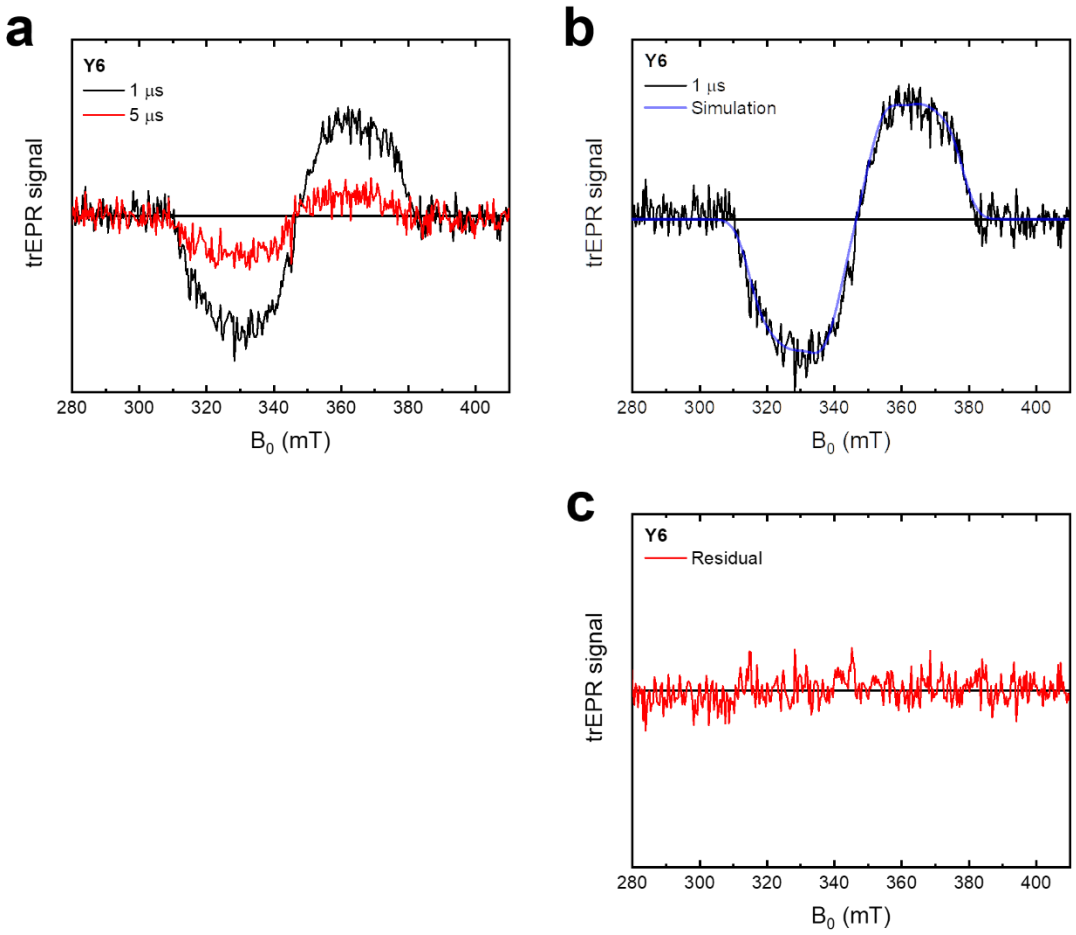

Figure S48: (a) The trEPR spectra of a neat Y6 film, taken at representative time points of 1 and 5 µs after excitation at 532 nm. Absorption (*a*) is up, emission (*e*) is down. **(b)** The trEPR spectra at 1 µs is shown, with the simulation overlaid. An *eeeaaa* polarisation pattern, indicative of a triplet exciton formed via ISC, is obtained. **(c)** The residual from the best fit simulation in Fig. S48b, shown on the same y-axis scale. The residual indicates that the simulation describes the experimental spectrum well.

ITIC film

The trEPR spectra of the neat ITIC film show a sharp peak at ~346 mT which is a signature of free polarons. A broad feature between 320 – 360 mT is weakly visible at 1 µs, which appears to have an *eeeaaa* polarisation pattern indicative of a triplet exciton formed via ISC. However, due to the extremely low intensity of the signal, it is not possible to perform a simulation to confirm this. The low intensity of the triplet signal suggests that triplet generation rates are very low.

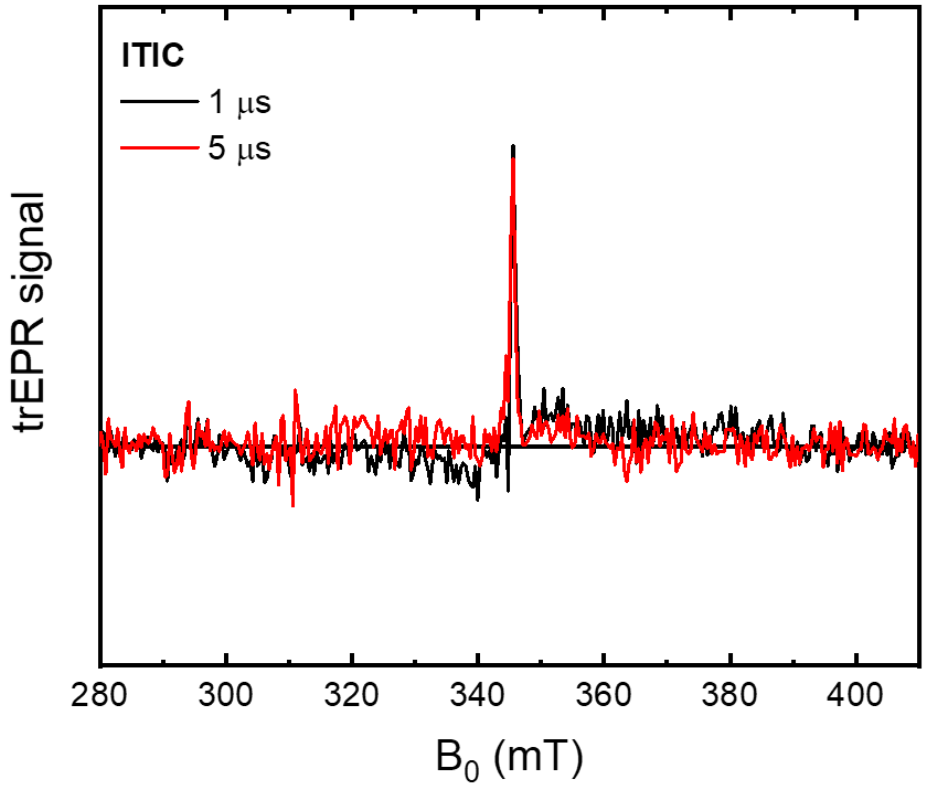

Figure S49: (a) The trEPR spectra of a neat ITIC film, taken at representative time points of 1 and 5 µs after excitation at 532 nm. Absorption (*a*) is up, emission (*e*) is down. The sharp peak at ~346 mT is a signature of free polarons.

IT-4F film

The trEPR spectra of the neat IT-4F film show a sharp peak at ~346 mT which is a signature of free polarons. No obvious features that could be associated with triplet excitons are visible in this sample, which highlights that IT-4F behaves similarly to the structurally related ITIC.

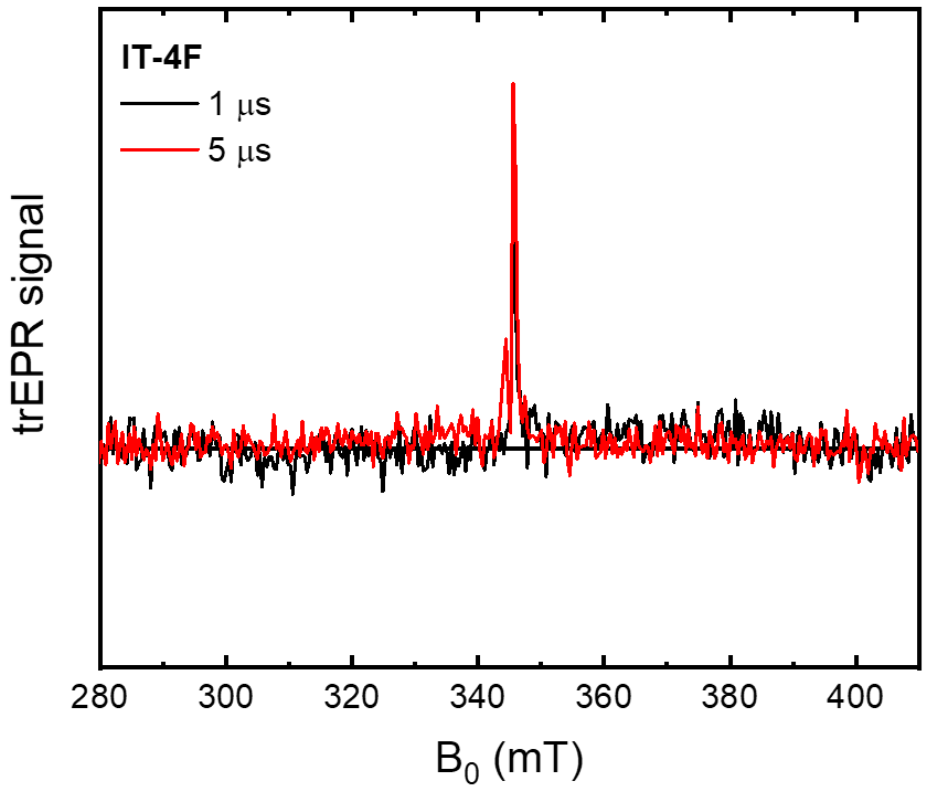

Figure S50: The trEPR spectra of a neat IT-4F film, taken at representative time points of 1 and 5 μs after excitation at 532 nm. Absorption (*a*) is up, emission (*e*) is down. The sharp peak at ~346 mT is a signature of free polarons.

IEICO-2F film

The trEPR spectra of the neat IEICO-2F film shows a sharp *ae* peak at ~346 mT, which is a signature of charge photogeneration. At this level of analysis, it is difficult to say if the charges are magnetically interacting (e.g. secondary CT state) or separated. A broad feature between 320 – 360 mT is weakly visible at 1 µs, which appears to have an *eeeaaa* polarisation pattern indicative of a triplet exciton formed via ISC. However, due to the extremely low intensity of the signal, it is not possible to perform a simulation to confirm this.

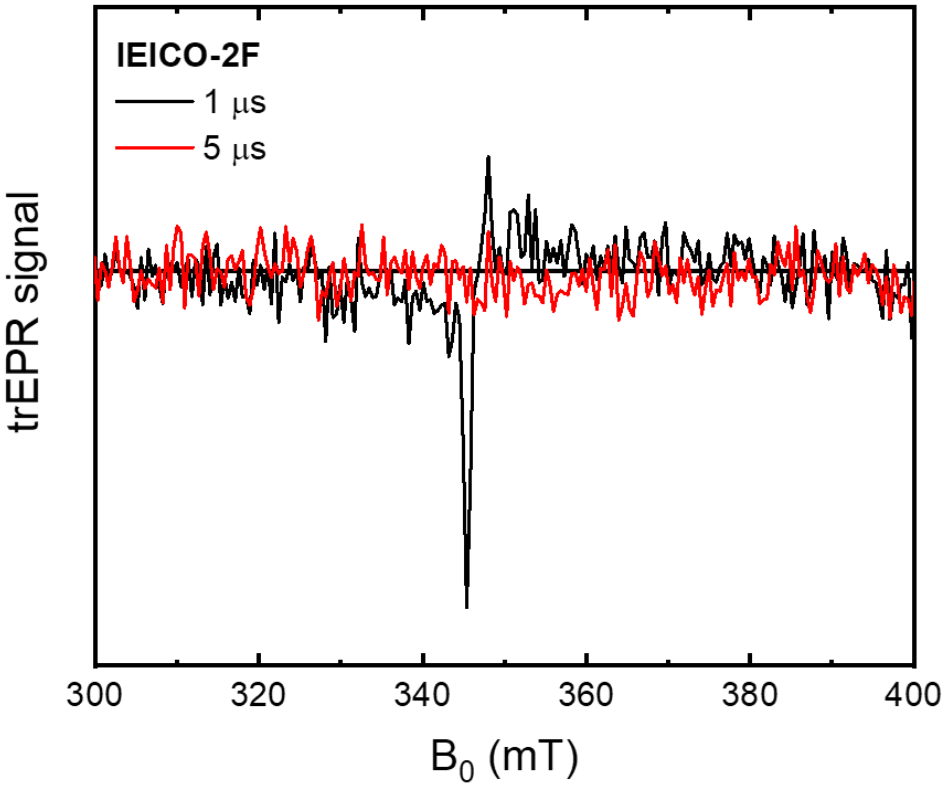

Figure S51: (a) The trEPR spectra of a neat IEICO-2F film, taken at representative time points of 1 and 5 µs after excitation at 532 nm. Absorption (*a*) is up, emission (*e*) is down.

SiOTIC-4F film

The trEPR spectra of the neat SiOTIC-4F film shows a broad signal between 310 – 380 mT, which is assigned to triplet excitons. As time progresses, the triplet signal inverts; this is likely due to unequal decay rates from the three high-field triplet states[50]. Due to the low S/N ratio, it is possible to obtain only the D value (840 MHz), which is typical of triplet states delocalised over a few aromatic rings. In addition, the eeeaaa polarization pattern at 1 µs confirms that the triplet states are generated via ISC. The absence of any clear signal attributable to free charges suggests that charge generation is less pronounced compared to the ITIC and IEICO series. This is further confirmed by the presence of a stronger triplet signal, which may be less visible in the ITIC and IEICO series of materials due to more efficient intermolecular charge transfer.

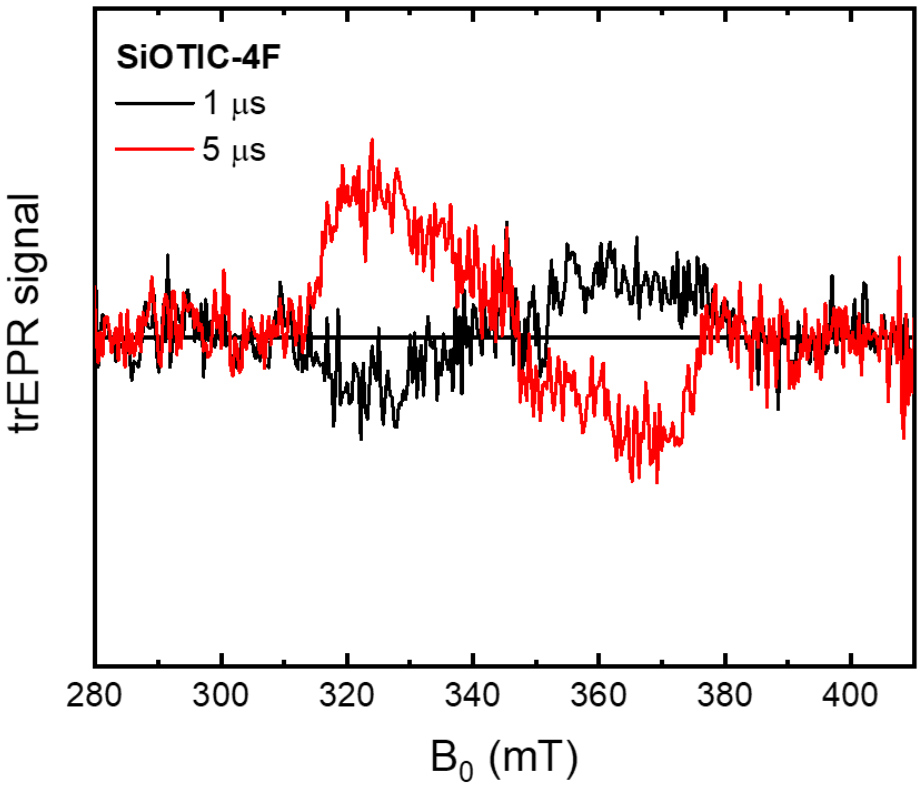

Figure S52: The trEPR spectra of a neat SiOTIC-4F film, taken at representative time points of 1 and 5 µs after excitation at 532 nm. Absorption (*a*) is up, emission (*e*) is down.

PM6:Y6 film

The trEPR spectra of the PM6:Y6 blend film shows a strong and sharp feature at ~346 mT, typical of a polaron; this underlines the expected strong charge photogeneration in this OSC blend. Conversely, the broad and weak signal between 290 – 410 mT is assigned to triplet excitons. The polaron signal is particularly intense compared to the triplet exciton signal in PM6:Y6, indicating that triplet generation in this blend is much less efficient than charge generation. From the best-fit simulation at 1 µs, an *eeeaaa* polarisation pattern, indicative of a triplet exciton formed via ISC, is obtained. The [D E] parameters of the triplet state are [1280 240] MHz. These are in between the values of triplet 1 observed in neat PM6 (Fig. S44) and the triplet observed in neat Y6 (Fig. S48). However, we believe that the triplet is most likely localised on Y6. We rationalise the larger D parameter of Y6 in the PM6:Y6 blend by considering the tendency of Y6 to form delocalised excitations in the more aggregated neat film environment where there is no polymer chains to disrupt the aggregation[2,49]. Importantly, no triplets with a polarisation pattern characteristic of BCT are observed in this blend.

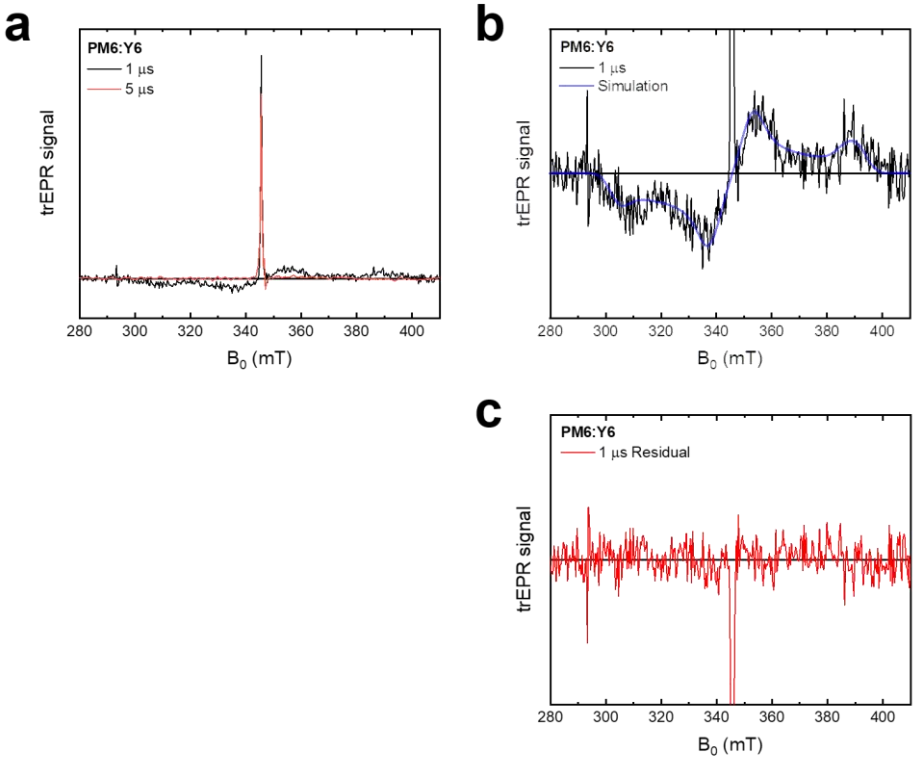

Figure S53: (a) The trEPR spectra of a PM6:Y6 blend film, taken at representative time points of 1 and 5 µs after excitation at 532 nm. Absorption (*a*) is up, emission (*e*) is down. **(b)** The trEPR spectra at 1 µs is shown, with the simulation overlaid. **(c)** The residual from the best fit simulation in Fig. S53b, shown on the same y-axis scale. The residual (excluding the polaron region, which was not included in the simulation) indicates that the simulation describes the experimental spectrum well.

PM6:ITIC film

The trEPR spectra of the PM6:ITIC blend film shows a strong and sharp *ea* feature at ~346 mT, typical of a CT state; this underlines the expected strong charge photogeneration in this OSC blend. Conversely, the broader signal between 290 – 410 mT is assigned to triplet excitons. As time progresses, the broader triplet signal disappears and a new, narrower triplet feature between 335 – 355 mT forms. From the best-fit simulation at 1 µs, an *eeeaaa* polarisation pattern, indicative of a triplet exciton formed via ISC, is obtained. The [D E] parameters of the triplet state are [1310 130] MHz, which are comparable to the spectra of triplet 1 observed in neat PM6 (Fig. S44). The narrower triplet, which appears at 5 µs, has [D E] parameters of [140 0] and is an excellent match to the spectrum of triplet 2 in PM6 (Fig. S44). Given the similarities in spectra and time evolution of the triplet signals, it is likely they originate from the ISC of un-dissociated singlets located on PM6. Importantly, no triplets with a polarisation pattern characteristic of BCT are observed in this blend.

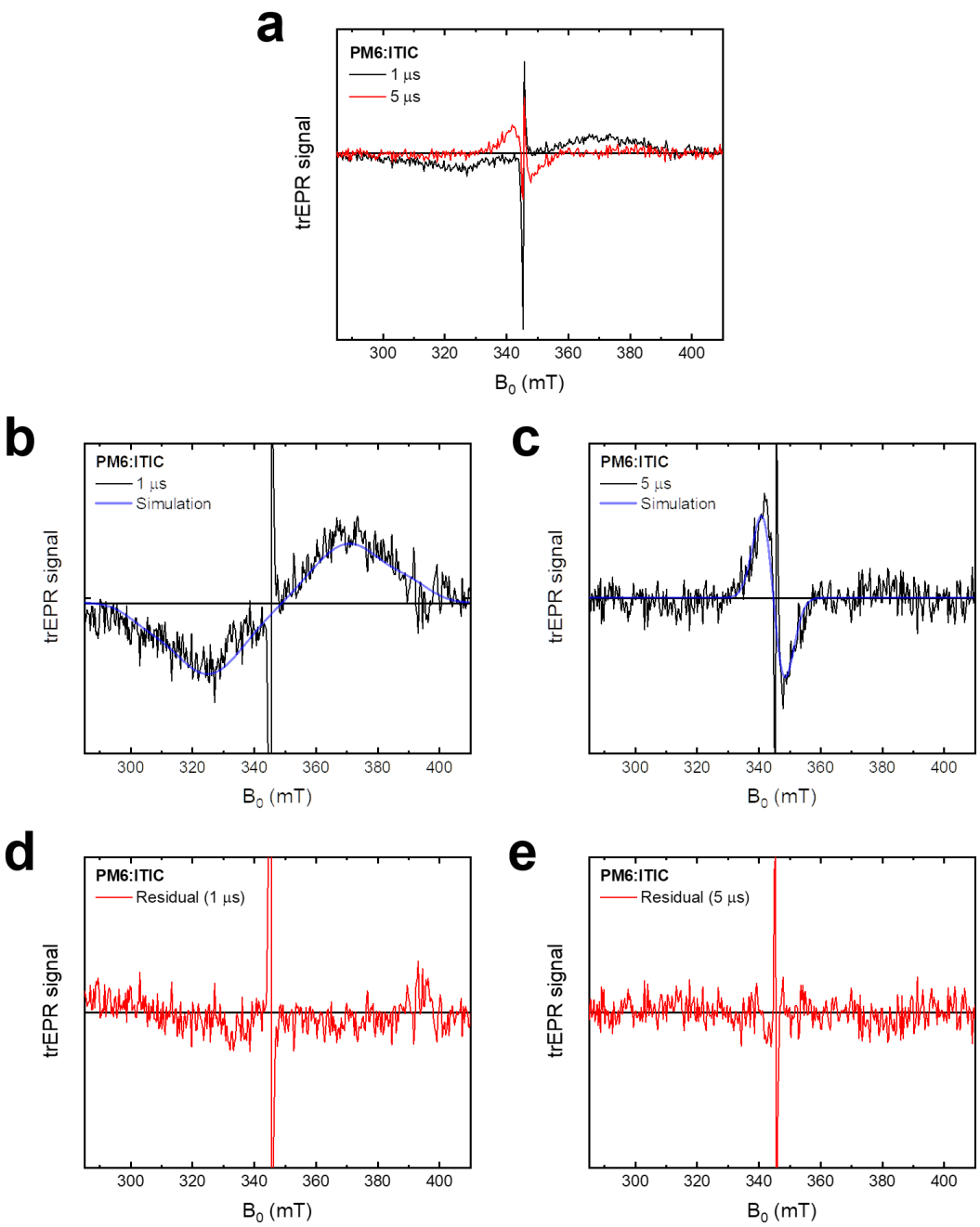

Figure S54: (a) The trEPR spectra of a PM6:ITIC blend film, taken at representative time points of 1 and 5 µs after excitation at 532 nm. Absorption (*a*) is up, emission (*e*) is down. **(b)** The trEPR spectra at 1 µs is shown, with the simulation overlaid. **(c)** The trEPR spectra at 5 µs is shown, with the simulation overlaid. **(d)** The residual from the best fit simulation in Fig. S54b, shown on the same y-axis scale. The residual (excluding the polaron region, which was not included in the simulation) indicates that the simulation describes the experimental spectrum well. **(e)** The residual from the best fit simulation in Fig. S54c, shown on the same y-axis scale. The residual (excluding the polaron region, which was not included in the simulation) indicates that the simulation describes the experimental spectrum well.

PM6:IT-4F film

The trEPR spectra of the PM6:IT-4F blend film shows a strong and sharp feature at ~346 mT, typical of free polarons; this underlines the strong charge photogeneration in this OSC blend. Conversely, the broader signal between 290 – 410 mT is assigned to triplet excitons. As time progresses, the broader triplet signal largely disappears and a new, narrower triplet feature between 335 – 355 mT forms. From the best-fit simulation at 1 µs, an *eeeaaa* polarisation pattern, indicative of a triplet exciton formed via ISC, is obtained. The [D E] parameters of the triplet state are [1300 90] MHz, which are comparable to the spectra of triplet 1 observed in neat PM6 (Fig. S44). Therefore, it is highly likely that the triplet is localised on PM6. Importantly, no triplets with a polarisation pattern characteristic of BCT are observed in this blend.

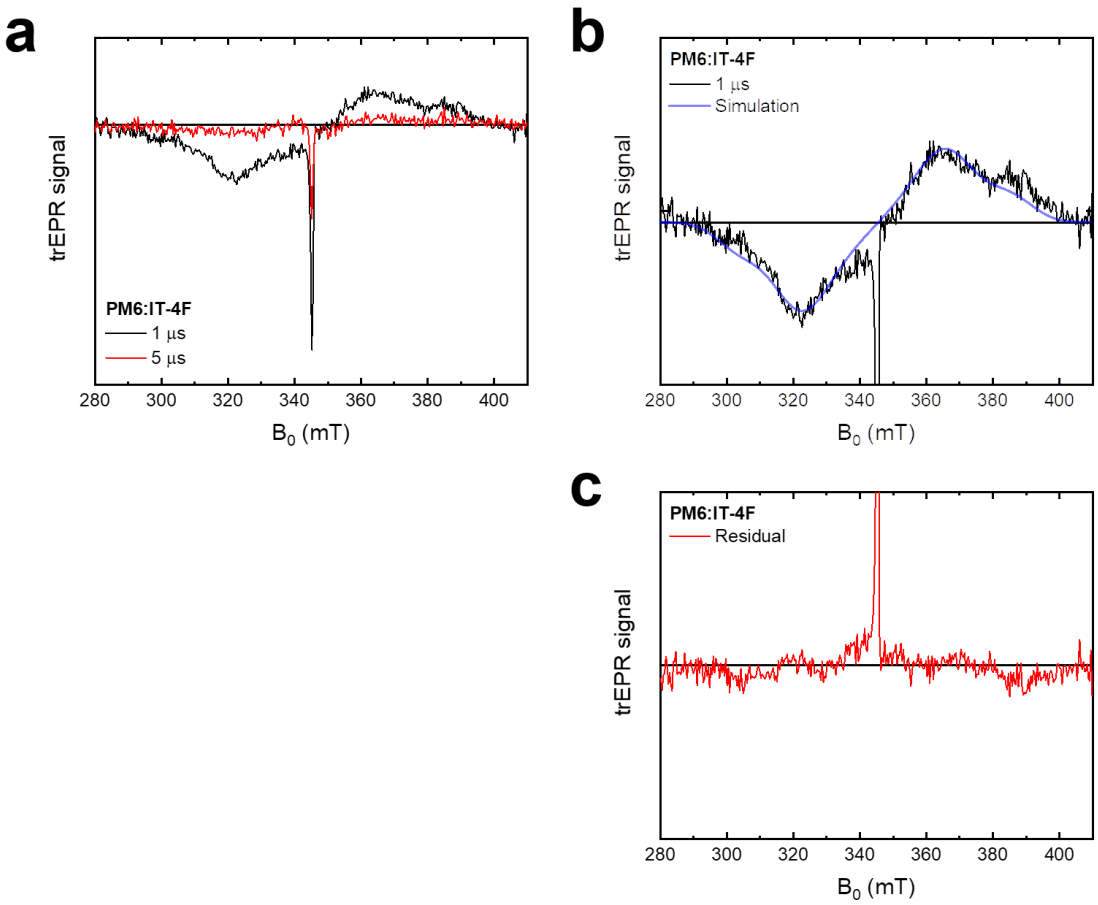

Figure S55: (a) The trEPR spectra of a PM6:IT-4F blend film, taken at representative time points of 1, 5 and 10 µs after excitation at 532 nm. Absorption (*a*) is up, emission (*e*) is down. **(b)** The trEPR spectra at 1 µs is shown, with the simulation overlaid. **(c)** The residual from the best fit simulation in Fig. S55b, shown on the same y-axis scale. The residual (excluding the polaron region, which was not included in the simulation) indicates that the simulation describes the experimental spectrum well.

PTB7-Th:IEICO-0F film

The trEPR spectra of the PTB7-Th:IEICO-0F blend film shows a sharp feature at ~346 mT typical of free polarons; this underlines the strong charge photogeneration in this OSC blend. Conversely, the broader signal between 310 – 380 mT is assigned to triplet excitons. As time progresses, the triplet signal inverts. This is likely due to unequal decay rates from the three high-field triplet states[50]. We note that the ISC triplet signal in this blend is significantly more intense relative to the polaron signal than in the PTB7-Th:IEICO-4F blend (Fig. S58), suggesting that the ISC of undissociated singlet excitons is enhanced; this is consistent with the observations in the TA (Fig. S24), where charge generation is slower in PTB7-Th:IEICO-0F, leading to the observation of IEICO-0F triplets formed via direct ISC from singlet excitons. From the best-fit simulation at 1 µs, an *eeeaaa* polarisation pattern, indicative of a triplet exciton formed via ISC, is obtained. The [D E] parameters of the triplet state are [850 210] MHz. As the [D E] parameters extracted are very different to those of the PTB7-Th triplet, the triplet observed here can be assigned to the direct ISC of un-dissociated excitons on IEICO-0F. Importantly, no triplets with a polarisation pattern characteristic of BCT are observed in this blend.

.

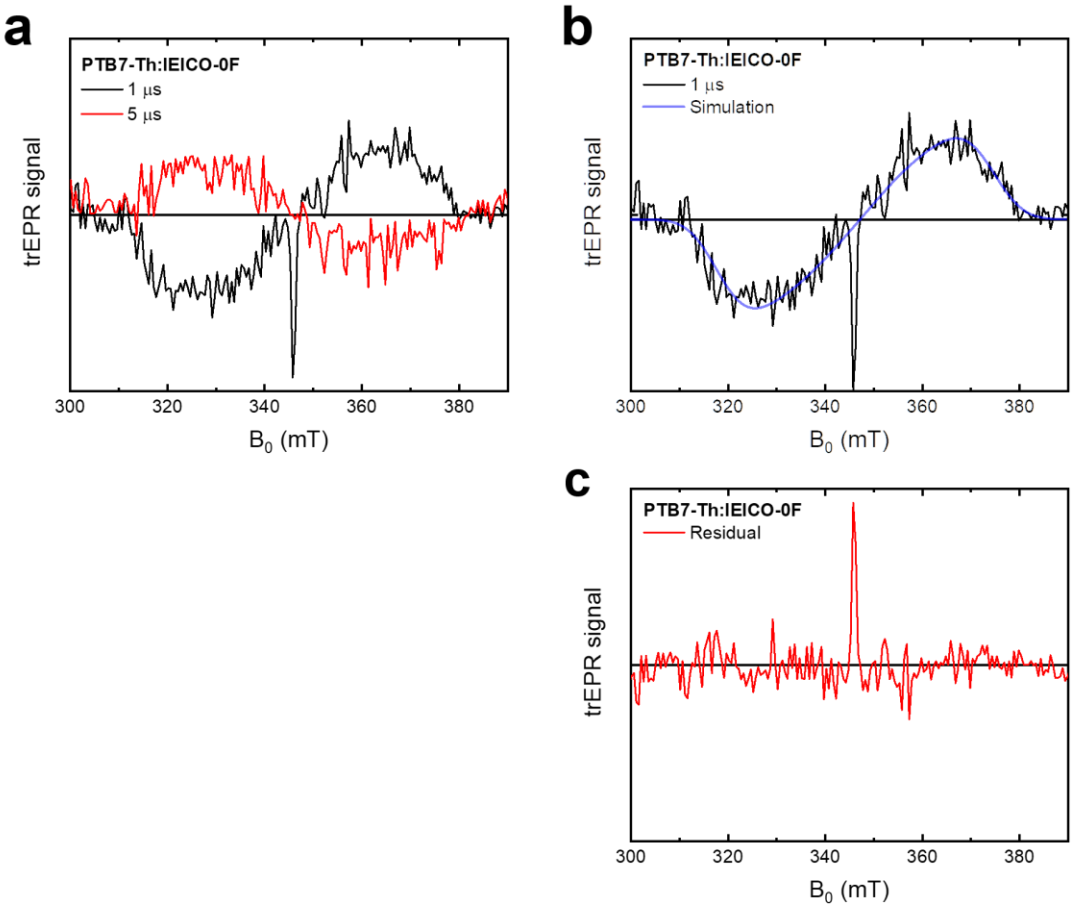

Figure S56: (a) The trEPR spectra of a PTB7-Th:IEICO-0F blend film, taken at representative time points of 1 and 5 µs after excitation at 532 nm. Absorption (*a*) is up, emission (*e*) is down. **(b)** The trEPR spectra at 1 µs is shown, with the simulation overlaid. **(c)** The residual from the best fit simulation in Fig. S56b, shown on the same y-axis scale. The residual (excluding the polaron region, which was not included in the simulation) indicates that the simulation describes the experimental spectrum well.

PTB7-Th:IEICO-2F film

The trEPR spectra of the PTB7-Th:IEICO-2F blend film shows a strong and sharp *ea* feature at ~346 mT, typical of a CT state; this underlines the expected strong charge photogeneration in this OSC blend. Conversely, the broader signal between 310 – 380 mT is assigned to triplet excitons. As time progresses, the triplet signal inverts. This is likely due to unequal decay rates from the three high-field triplet states[50]. From the best-fit simulation at 1 µs, an *eeeaaa* polarisation pattern, indicative of a triplet exciton formed via ISC, is obtained. The [D E] parameters of the triplet state are [850 190] MHz. As the [D E] parameters extracted are very different to those of the PTB7-Th triplet, the triplet observed here can be assigned to the direct ISC of un-dissociated excitons on IEICO-2F. Importantly, no triplets with a polarisation pattern characteristic of BCT are observed in this blend.

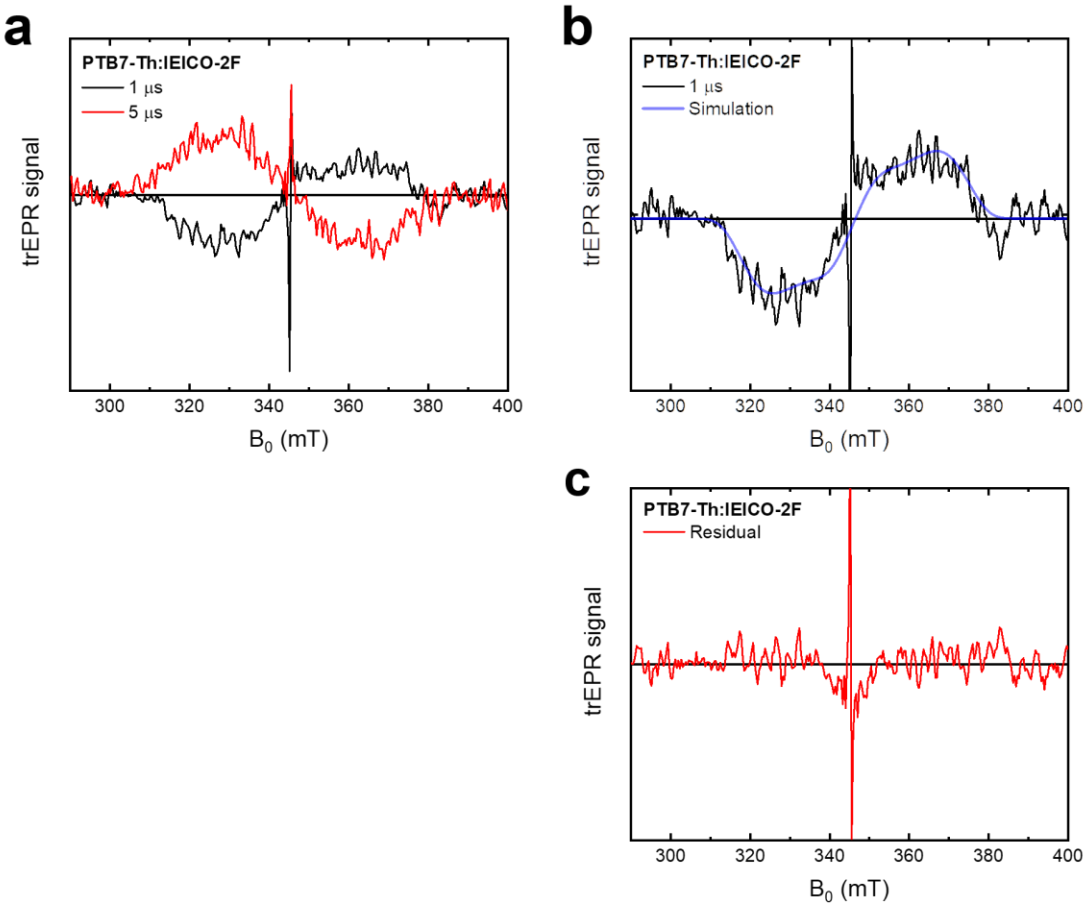

Figure S57: (a) The trEPR spectra of a PTB7-Th:IEICO-2F blend film, taken at representative time points of 1 and 5 µs after excitation at 532 nm. Absorption (*a*) is up, emission (*e*) is down. **(b)** The trEPR spectra at 1 µs is shown, with the simulation overlaid. **(c)** The residual from the best fit simulation in Fig. S57b, shown on the same y-axis scale. The residual (excluding the polaron region, which was not included in the simulation) indicates that the simulation describes the experimental spectrum well.

PTB7-Th:IEICO-4F film

The trEPR spectra of the PTB7-Th:IEICO-4F blend film shows a strong and sharp peak in at ~346 mT, which is a signature of efficient charge photogeneration. No obvious triplet signals are present in the blend. The absence of triplets, especially in comparison to the prominent triplet in the PTB7-Th:IEICO-0F blend, can be attributed to the more rapid hole transfer in this blend. This quenches the singlet excited states on the NFA faster, leaving less opportunity for ISC.

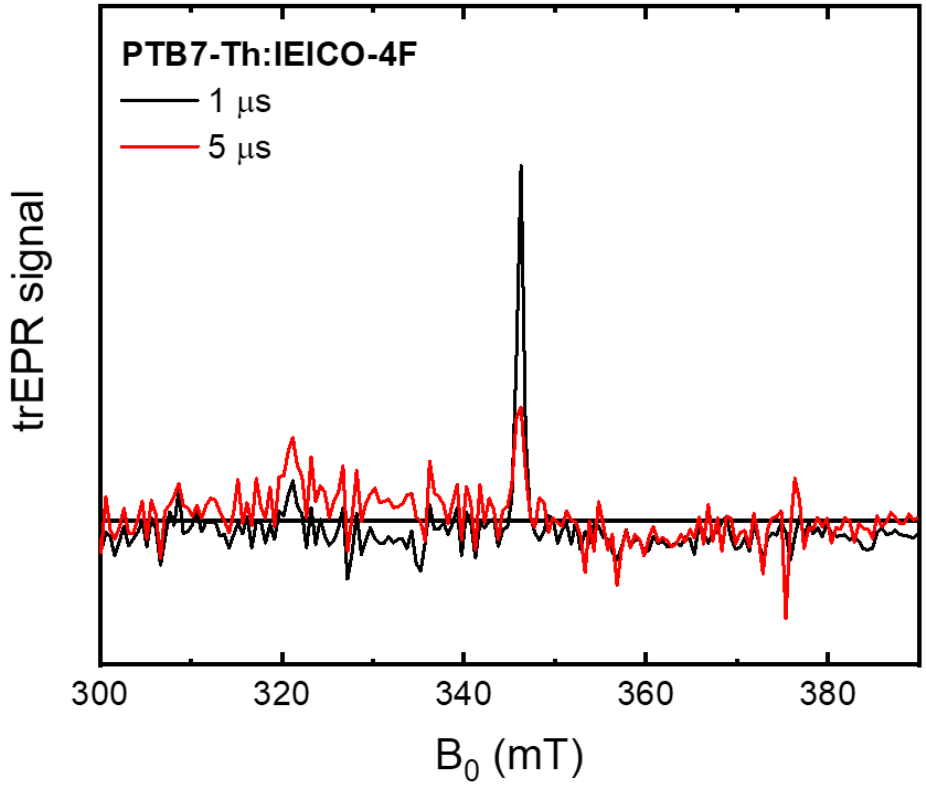

Figure S58: The trEPR spectra of a PTB7-Th:IEICO-4F blend film, taken at representative time points of 1 and 5 μs after excitation at 532 nm. Absorption (*a*) is up, emission (*e*) is down.

PTB7-Th:SiOTIC-4F film

The trEPR spectra of PTB7-Th:SiOTIC-4F blend film show a strong and sharp feature at ~346 mT typical of free polarons, which confirms the strong charge photogeneration in this blend. Conversely, the broader signal between 310 – 380 mT is assigned to triplet excitons. As time progresses, the triplet signal inverts and becomes more evident. This is likely due to a subtle balance between populating and depopulating rates of the three high-field triplet states[50]. From the best-fit simulation at 5 µs, an *eeeaaa* polarisation pattern, indicative of a triplet exciton formed via ISC, is obtained. The [D E] parameters of the triplet state are [920 210] MHz, which closely match those obtained from the neat SiOTIC-4F film (Fig. S52). Therefore, the triplet is assigned to the direct ISC of un-dissociated excitons on SiOTIC-4F. Importantly, no triplets with a polarisation pattern characteristic of BCT are observed in this blend.

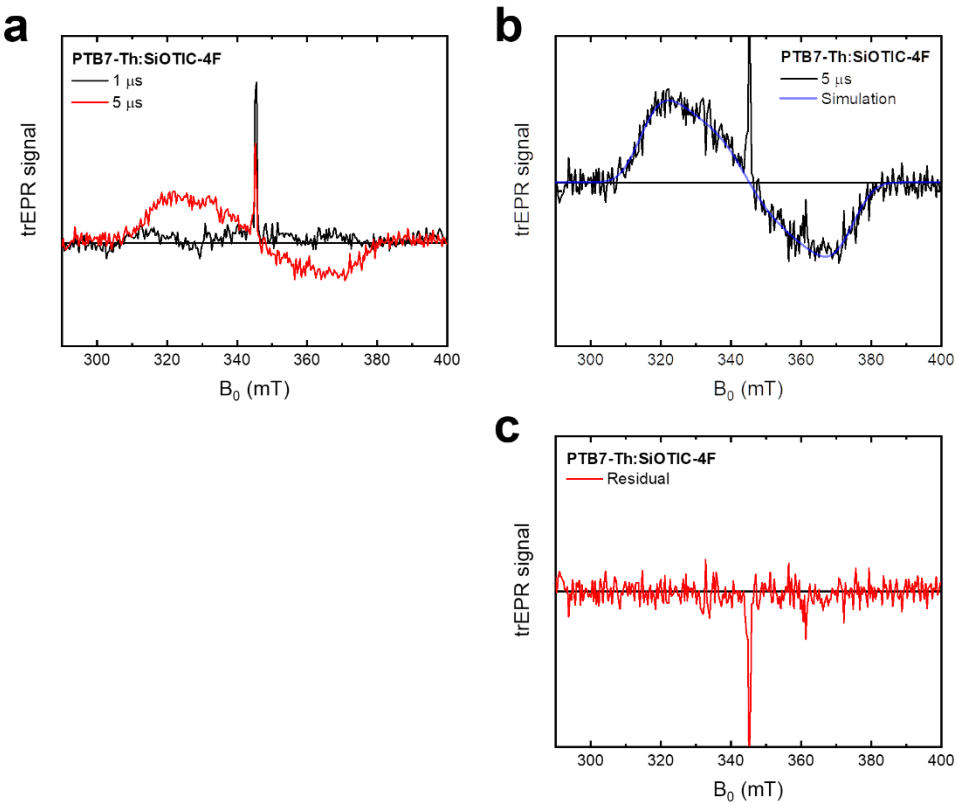

Figure S59: (a) The trEPR spectra of a PTB7-Th:SiOTIC-4F blend film, taken at representative time points of 1 and 5 µs after excitation at 532 nm. Absorption (*a*) is up, emission (*e*) is down. **(b)** The trEPR spectra at 5 µs is shown, with the simulation overlaid. **(c)** The residual from the best fit simulation in Fig. S59b, shown on the same y-axis scale. The residual (excluding the polaron region, which was not included in the simulation) indicates that the simulation describes the experimental spectrum well.

PBDB-T:ITIC film

The trEPR spectra of the PBDB-T:ITIC blend film shows a strong and sharp feature at ~346 mT, characteristic of free polarons; this underlines the strong charge photogeneration in this blend. Conversely, the broader signal between 290 – 400 mT is assigned to triplet excitons. From the best-fit simulation at 1 µs, an *eeeaaa* polarisation pattern, indicative of a triplet exciton formed via ISC, is observed. The [D E] parameters of the triplet state are [1380 220] MHz, which are comparable to the values obtained from the neat PBDB-T film (Fig. S46). Therefore, the triplet is assigned to the direct ISC of un-dissociated excitons on PBDB-T. Importantly, no triplets with a polarisation pattern characteristic of BCT are observed in this blend.

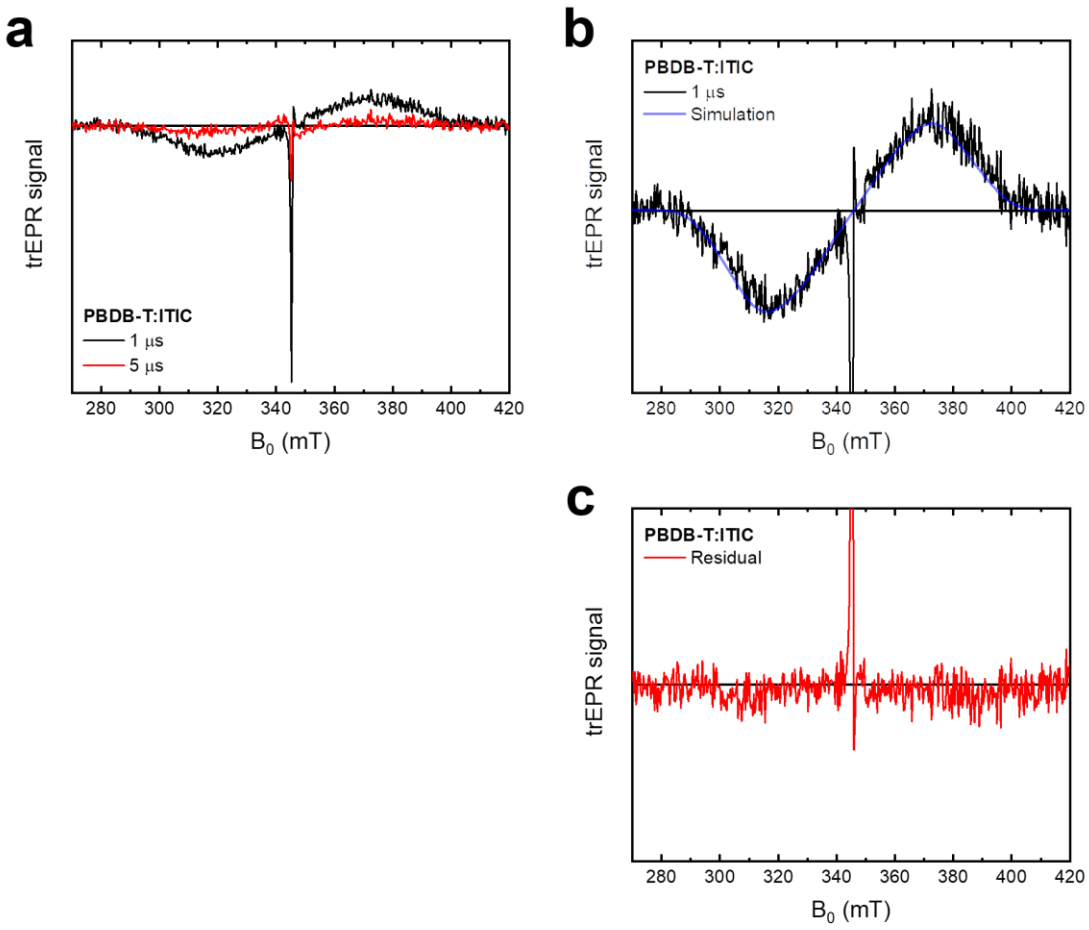

Figure S60: (a) The trEPR spectra of a PBDB-T:ITIC blend film, taken at representative time points of 1 and 5 µs after excitation at 532 nm. Absorption (*a*) is up, emission (*e*) is down. **(b)** The trEPR spectra at 1 µs is shown, with the simulation overlaid. **(c)** The residual from the best fit simulation in Fig. S60b, shown on the same y-axis scale. The residual (excluding the polaron region, which was not included in the simulation) indicates that the simulation describes the experimental spectrum well.

J51:ITIC film

The trEPR spectra of the J51:ITIC blend film shows a strong and sharp peak in at ~346 mT; the signal has an *ea* polarisation pattern at 1 µs and evolves into pure *a* at 5 µs. This is a signature of photogenerated charges that at early times are close to each other and magnetically interacting (CT state), with a later time separation into free charges. No obvious triplet signals are present in the blend. The absence of triplets can likely be assigned to a rapid charge transfer in this blend which limits the ISC triplet yield.

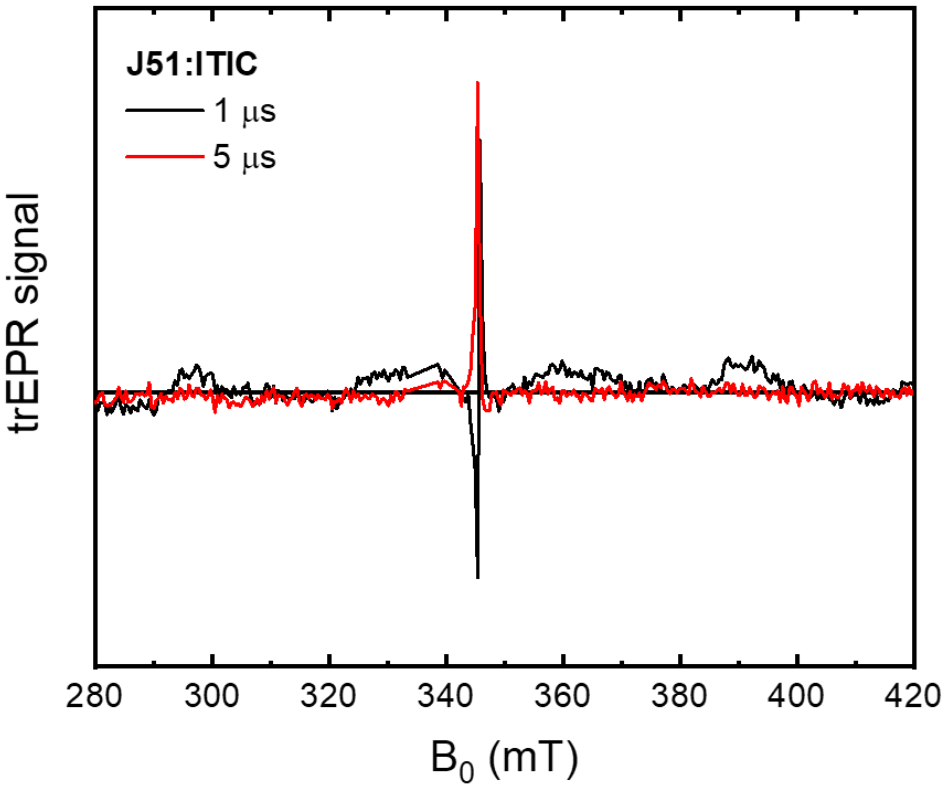

Figure S61: The trEPR spectra of a J51:ITIC blend film, taken at representative time points of 1 and 5 µs after excitation at 532 nm. Absorption (*a*) is up, emission (*e*) is down.

Full 2D trEPR spectra

PM6

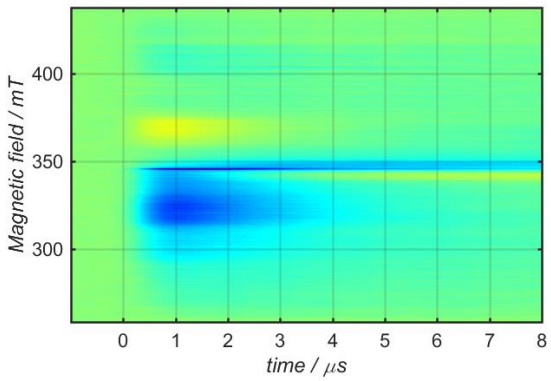

PTB7-Th

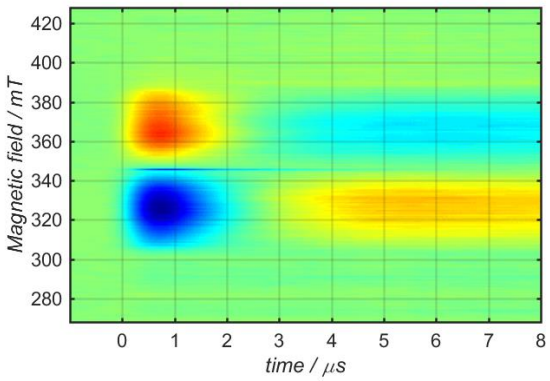

PBDB-T

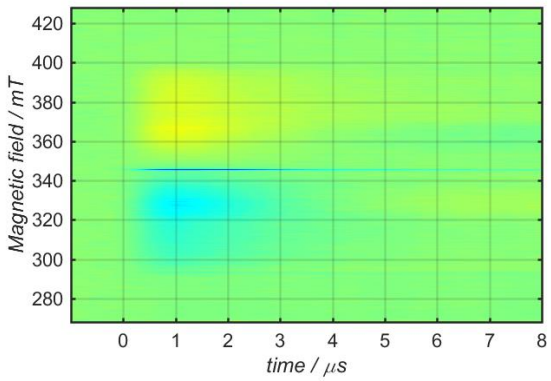

J51

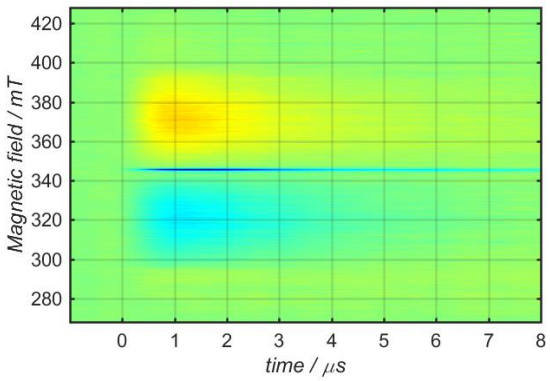

Y6

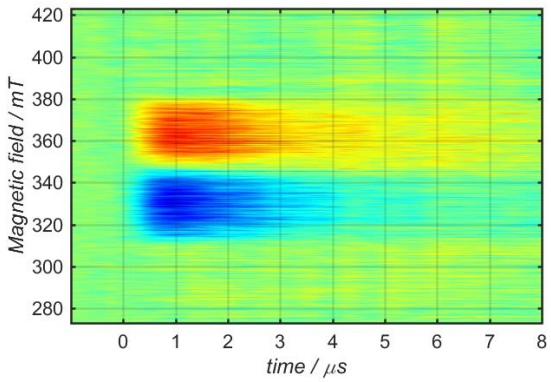

ITIC

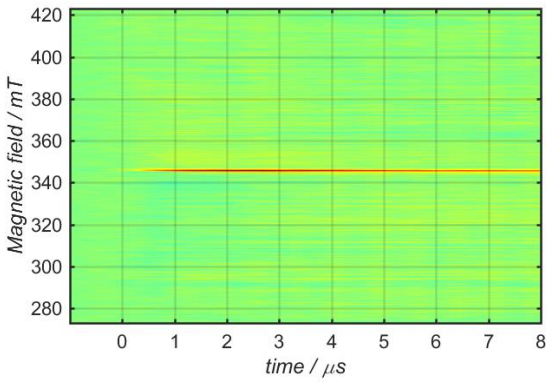

IT-4F

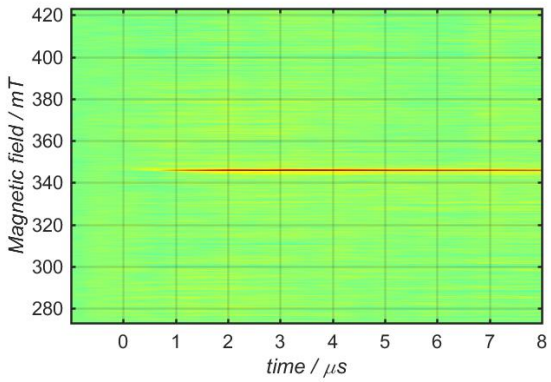

IEICO-2F

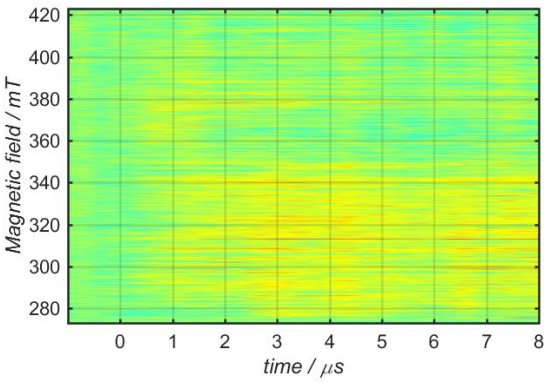

SiOTIC-4F

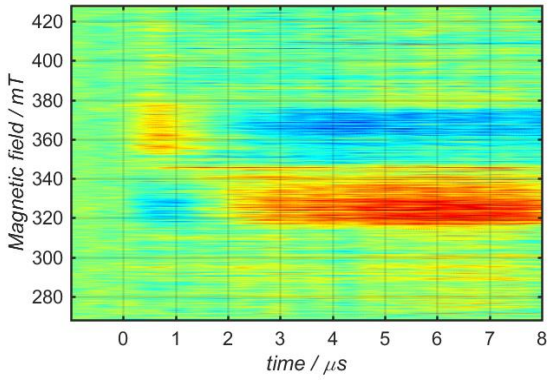

PM6:Y6

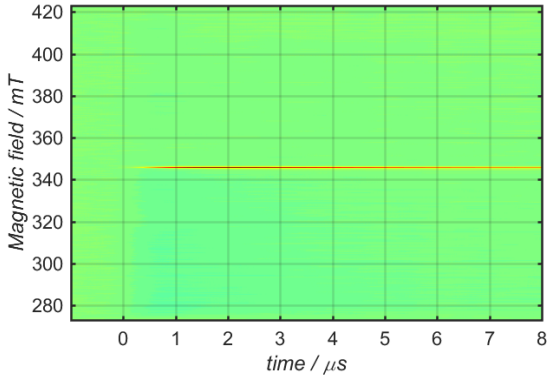

PM6:ITIC

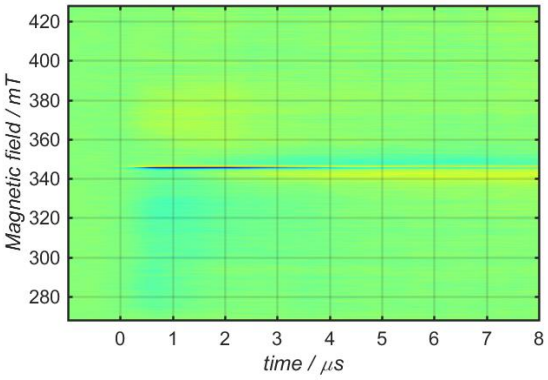

PM6:IT-4F

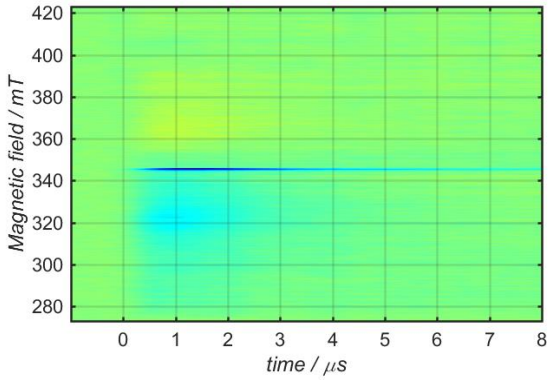

PTB7-Th:IEICO-0F

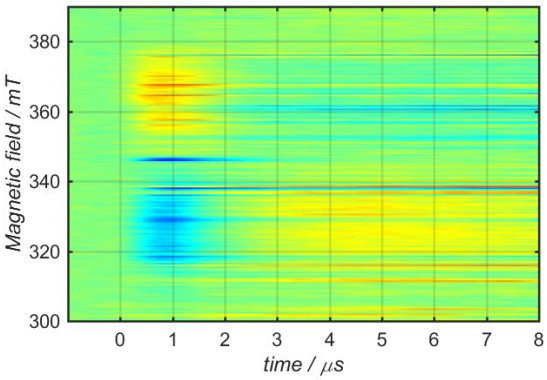

PTB7-Th:IEICO-2F

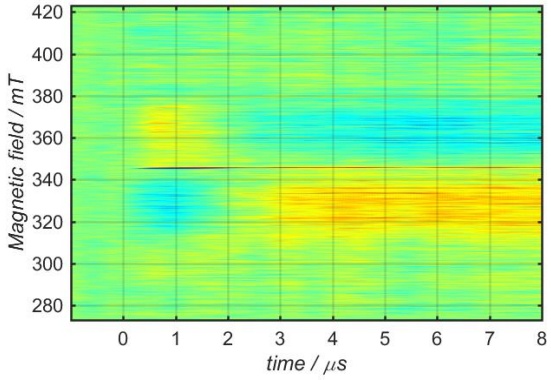

PTB7-Th:IEICO-4F

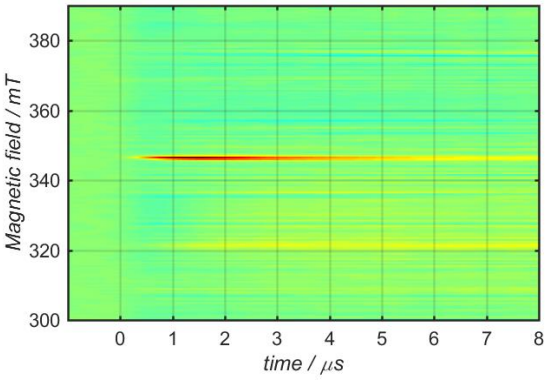

PTB7-Th:SiOTIC-4F

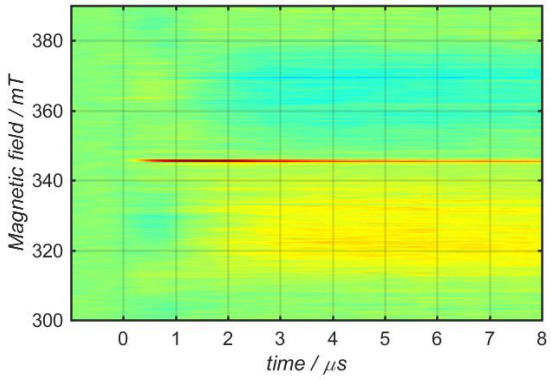

PBDB-T:ITIC

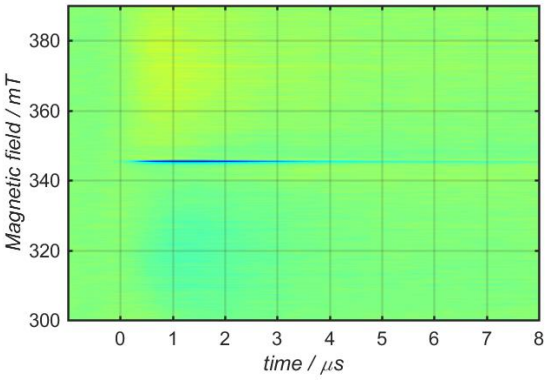

J51:ITIC

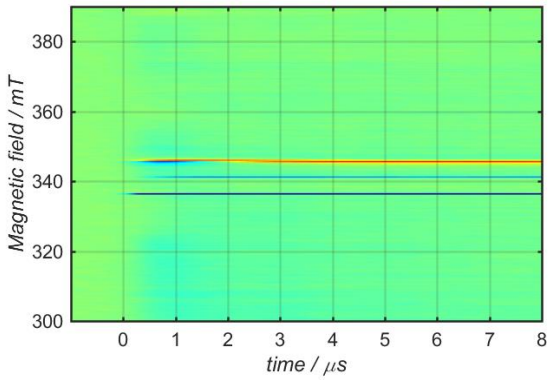

Figure S62: The raw 2D trEPR spectra of all the films studied in this work acquired at 80 K after excitation at 532 nm. In the previous discussion all the reported spectra have been time-averaged over 1000 ns), with smoothing applied where necessary. Colour legend: blue = emission, red = absorption.

E_g *and* E_{CT} determination for NFA blends

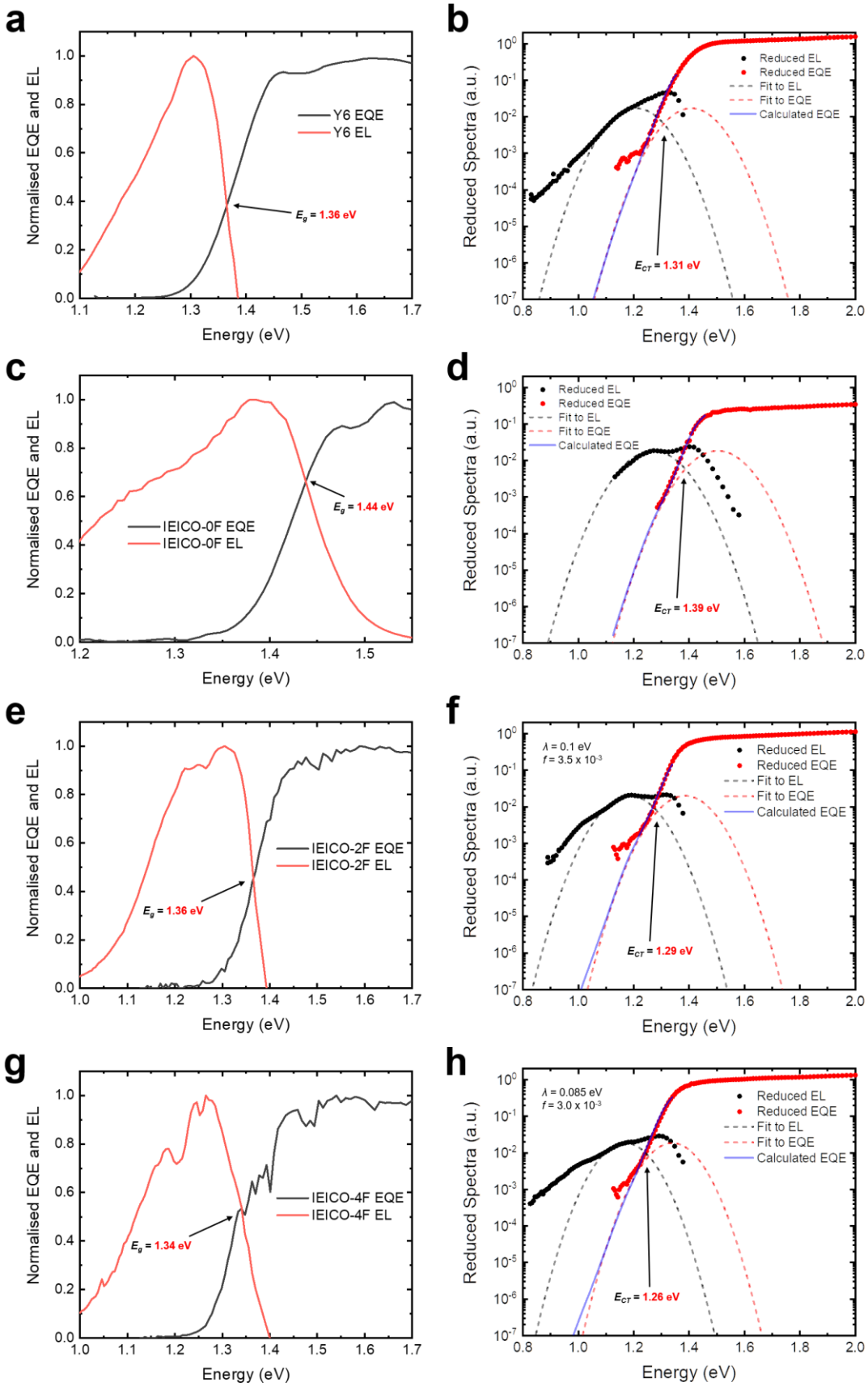

Figure S63: (a) The band gap of Y6 is 1.36 eV, as determined from the crossing point of the normalised EQE and EL spectra of a neat Y6 OSC. **(b)** The reduced EQE and EL spectra for PM6:Y6 with the fits obtained from Marcus theory included. From this, a charge transfer state energy (E_{CT}) = 1.31 eV is obtained. **(c)** The band gap of IEICO-0F is 1.44 eV, as determined from the crossing point of the normalised EQE and EL spectra of a neat IEICO-2F OSC. **(d)** The reduced EQE and EL spectra for PTB7-Th:IEICO-0F with the fits obtained from Marcus theory included. From this, E_{CT} = 1.39 eV is obtained. **(e)** The band gap of IEICO-2F is 1.36 eV, as determined from the crossing point of the normalised EQE and EL spectra of a neat IEICO-2F OSC. **(f)** The reduced EQE and EL spectra for PTB7-Th:IEICO-2F with the fits obtained from Marcus theory included. From this, a charge transfer state energy (E_{CT}) = 1.29 eV is obtained. **(g)** The band gap of IEICO-4F is 1.34 eV, as determined from the crossing point of the normalised EQE and EL spectra of a neat IEICO-2F OSC. **(h)** The reduced EQE and EL spectra for PTB7-Th:IEICO-4F with the fits obtained from Marcus theory included. From this, E_{CT} = 1.26 eV is obtained.

The equations used to perform the Marcus theory fitting and obtain the E_{CT}[51]:

$$EQE_{PV,CT}(E) = \frac{f}{E\sqrt{4\pi\lambda k_B T}} \exp\left(\frac{-(E_{CT} + \lambda - E)^2}{4\lambda k_B T}\right) \quad (5)$$

$$EQE_{EL,CT}(E) = E\frac{f}{\sqrt{4\pi\lambda k_B T}} \exp\left(\frac{-(E_{CT} - \lambda - E)^2}{4\lambda k_B T}\right) \quad (6)$$

$$EQE_{PV}(E) \propto EL(E)E^{-2} \exp\left(\frac{E}{k_B T}\right) \quad (7)$$

where, k_B is Boltzmann's constant, E is the photon energy, and T is the absolute temperature. The fit parameters are E_{CT}, which is the energy at the point of intersection between the CT state absorption and emission, λ, which is the reorganization energy, and f, which is a measure of the strength of the donor-acceptor coupling.

Quantum chemical calculations

Time-Dependent Density Functional Theory calculations

To begin our computational study, we shall focus on several representative models for 1:1 D/A complexes, comprising a tetramer of PTB7-Th interacting with IEICO-2F or SiOTIC-4F. It is pertinent to note here that the PTB7-Th:IEICO-2F blend did not exhibit non-geminate T_1 formation, whilst the PTB7-Th:SiOTIC-4F blend did. Additionally, as both blends utilise the same donor polymer, PTB7-Th, this allows for a more consistent investigation of factors involving the NFA that affect triplet formation. In all the calculations, the alkyl chains were replaced with methyl groups to reduce the computational costs. Gas-phase ground state 1:1 complexes were optimized at the DFT level with a range-separated hybrid (RSH) ωB97X-D functional using 6-31G(d,p) basis set[52]. The D/A intermolecular equilibrium distance was found to be in range of 3.5–4.0 Å for all investigated configurations. In order to account for the solid-state environment, we tuned the range-separation parameter ω in the presence of polarizable continuum model (PCM) by setting the dielectric constant of toluene $\varepsilon = 2.37$ and utilizing optimized gas-phase geometries[53]. In this approach[54], for each system of interest an optimal value of ω was found by aligning the negative eigenenergies of HOMO orbitals for the N and the (N+1)-electron system with their respective vertical ionization potentials (IP) (barring relaxation effects). The overall error function to be minimize is given as follows:

$$J^2(\omega) = \sum_{i=0}^{1} (\varepsilon_{HOMO}(N+i,\omega) + IP(N+i,\omega))^2 \qquad (8)$$

The non-empirical "optimal" tuning ω in PCM yielded $\omega_{PCM} = 0.011\, Bohr^{-1}$ for the PTB7-Th:IEICO-2F complex and $\omega_{PCM} = 0.014\, Bohr^{-1}$ for PTB7-Th:SiOTIC-4F. Subsequent TD-DFT + PCM calculations were carried out with the optimally tuned ω_{PCM} parameter for each complex, targeting the ^{1}CT and ^{3}CT energies of the D/A dyads which together with the energies of local excitations are summarised in Table S3. Interestingly, as explained in the main text in Figure 3a, the energy ordering of the CT states is inverted in the PTB7-Th:IEICO-2F complex, with the ^{3}CT higher than the ^{1}CT by 70 meV as a result of hybridisation between local exciton and CT states. On the other hand, the typical energy ordering is restored in the other two complexes due to the lack of hybridisation effects. Indeed, in PTB7-Th:SiOTIC-4F, the ^{3}CT is lower in energy of 18 meV with respect to the ^{1}CT.

To check the accuracy of the optimally-tuned functionals, we benchmarked the excitation energies by employing more robust *screened* RSH (SRSH) functionals[55]. In this approach, solid-state polarization effects are introduced by adjusting two additional *α* and *β* parameters within the exchange-correlation density functional along with ω. For LC-ωhPBE functional[56], the exchange-correlation energy expression reads as:

$$E_{xc}^{SRSH} = (\alpha + \beta)E_{x,HF}^{LR} + (1 - \alpha - \beta)E_{x,PBE}^{LR} + \alpha E_{x,HF}^{SR} + (1 - \alpha)E_{x,PBE}^{SR} + E_{c,PBE} \qquad (9)$$

where *α* quantifies the fraction of Hartree-Fock (HF) exchange included in the short-range (SR) domain, while $\alpha + \beta$ quantifies the fraction of HF exchange included in the long-range (LR) part and the PBE correlation is used for the whole range. For any choice of *α*, the condition $\alpha + \beta = 1$ ensures 100% of HF exchange in the LR part and the correct asymptotic behaviour of the Coulomb potential in gas-phase. To introduce the effect of the surrounding medium, we imposed the asymptotic convergence of Coulomb potential to $\frac{1}{\varepsilon r}$ rather than to $\frac{1}{r}$, and by fixing $\alpha = 0.2$, we deduced the *β* parameter from $\alpha + \beta = \frac{1}{\varepsilon}$, so that $\beta = \frac{1}{\varepsilon} - \alpha = 0.221$, where $\varepsilon = 2.37$ (a typical value used for a variety of organic molecules). In these calculations, the optimally tuned ω_{vac} (in vacuum) value have been retained: for PTB7-Th:IEICO-2F we have found $\omega_{vac} = 0.080\ Bohr^{-1}$, while for PTB7-Th:SiOTIC-4F $\omega_{vac} = 0.079\ Bohr^{-1}$.

The SRSH TD-DFT calculations have been carried out for G0_PTB7-Th:IEICO-2F and G0_PTB7-Th:SiOTIC-4F complexes, featuring the smallest and the largest energy difference between ^{3}CT and ^{1}CT, respectively. In PTB7-Th:IEICO-2F, the ^{3}CT has been found to be higher in energy than the ^{1}CT by 45 meV, a result which is on par with that obtained with the optimally tuned functionals (the energy of ^{1}CT is 1.41 eV with an oscillator strength of 0.171 and the energy of ^{3}CT is 1.46 eV). In contrast, the PTB7-Th:SiOTIC-4F complex shows a more stable ^{3}CT in energy than its ^{1}CT by 34 meV, with the energy of ^{1}CT of 1.45 eV (with an oscillator strength of 0.003) and the energy of ^{3}CT of 1.42 eV. The consistency of the results obtained by the two approaches that introduce solid-state screening effects in a different fashion indicates a weak dependence on methodology, which reinforces the robustness of the conclusions drawn from the theoretical data. DFT and TD-DFT calculations were carried out with Gaussian16 suite[57].

Back charge-transfer rate calculations

Since the exact back-charge transfer rate between ^{3}CT and T_1 is difficult to obtain experimentally, we computed the values theoretically for all the representative polymer/NFA complexes from Figure S65. Here, we first defined auxiliary diabatic states $(D^+)(A^-)$, $(D^*)(A^0)$, and $(D^0)(A^*)$ where D is for donor (polymer), and A is for acceptor (NFA), being either in ionized (+/-), ground (0) or excited T_1 (*) state, respectively. These states represent ^{3}CT and T_1 in the absence of configurational mixing. With this definition, the BCT rate was calculated by employing Marcus-Levich-Jortner theory[58,59], using the following expression:

$$k_{CT\to T1\left(\frac{D}{A}\right)} = \frac{2\pi}{\hbar} H^2_{CT\to T1\left(\frac{D}{A}\right)} \sqrt{\frac{1}{4\pi\lambda_s k_B T}} \sum_{n=0}^{\infty} exp^{-S} \frac{S^n}{n!} exp^{-\frac{\left(\Delta E_{\mathrm{CT\to T1}\left(\frac{\mathrm{D}}{\mathrm{A}}\right)} + \lambda_s + n\hbar\omega_i\right)^2}{4\lambda_s k_B T}} \qquad (10)$$

where besides for the fundamental Boltzmann constant, k_B, and temperature, T of 298.15 K, three most important contributions, namely, the difference in the diabatic energies, $\Delta E_{\mathrm{CT\to T1(D/A)}}$, coupling parameter between the triplet states, $H_{CT\to T1(D/A)}$, and Huang-Rhys factors, $S = \lambda_i/\hbar\omega$, were calculated for each D/A complex as described below. In turn, the remaining, external reorganization energy, λ_s, together with $\hbar\omega$, were taken from literature.

To compute the couplings, we utilized the Generalized Mulliken-Hush theory that targets minimizing the transition dipole moment between the adiabatic ^{3}CT and T_1, $\mu_{CT\to T1(D/A)}$[60]. For the two-state model, the coupling is given as follows:

$$H_{CT\to T1\left(\frac{D}{A}\right)} = \frac{\mu_{CT\to T1\left(\frac{D}{A}\right)} \left(E^{ad}_{T1\left(\frac{D}{A}\right)} - E^{ad}_{CT}\right)}{\sqrt{\left(\mu_{T1\left(\frac{D}{A}\right)} - \mu_{CT}\right)^2 - 4\mu^2_{CT\to T1\left(\frac{D}{A}\right)}}} \qquad (11)$$

This scheme is particularly convenient since it deals only with the observable adiabatic energies, E^{ad}, and state dipole moments, μ, that are readily available from TD-DFT calculations using the Gaussian software suite. The transition dipole moments between the (excited) ^{3}CT and T_1 states were extracted by post-processing the TD-DFT wavefunctions using the Multiwfn software[61].

The λ_i internal reorganization energy entering Eq. 10 through the Huang-Rhys factor *S* reflects changes in the geometry of the D/A complex upon BCT. These were calculated at the DFT level based on 4-point total energy differences between reactants and products and assuming additive contributions from the polymer donor and NFA acceptor[62].

Finally, using the two-state model, the difference in diabatic energies was directly deduced from the adiabatic-to-diabatic transformation[63,64], given as:

$$\begin{pmatrix} E_{CT}^{diab} & H_{CT\rightarrow T1\left(\frac{D}{A}\right)} \\ H_{CT\rightarrow T1\left(\frac{D}{A}\right)} & E_{T1\left(\frac{D}{A}\right)}^{diab} \end{pmatrix} = U \begin{pmatrix} E_{CT}^{ad} & 0 \\ 0 & E_{T1\left(\frac{D}{A}\right)}^{ad} \end{pmatrix} U^T \quad (12)$$

where U is a unitary matrix, commonly referred to as a rotation matrix for a mixing angle between adiabatic ^{3}CT and T_1, α, given as:

$$U = \begin{pmatrix} \cos\alpha & \sin\alpha \\ -\sin\alpha & \cos\alpha \end{pmatrix} \quad (13)$$

Once the coupling was computed from eq. 11, the mixing angle was determined from $\sin 2\alpha = 2H_{CT\rightarrow T1(D/A)}/\Delta E^{ad}$, leading to a rapid evaluation of the diabatic energy differences as

$$\Delta E^{diab} = \Delta E^{ad} \cdot \cos 2\alpha = \Delta E^{ad} \cdot \sqrt{\frac{\Delta E_{ad}^2 - 4H_{CT\rightarrow T1\left(\frac{D}{A}\right)}^2}{\Delta E_{ad}^2}} = (sign)\sqrt{\Delta E_{ad}^2 - 4H_{CT\rightarrow T1\left(\frac{D}{A}\right)}^2} \quad (14)$$

with the sign taken in consistency with ΔE^{ad}.

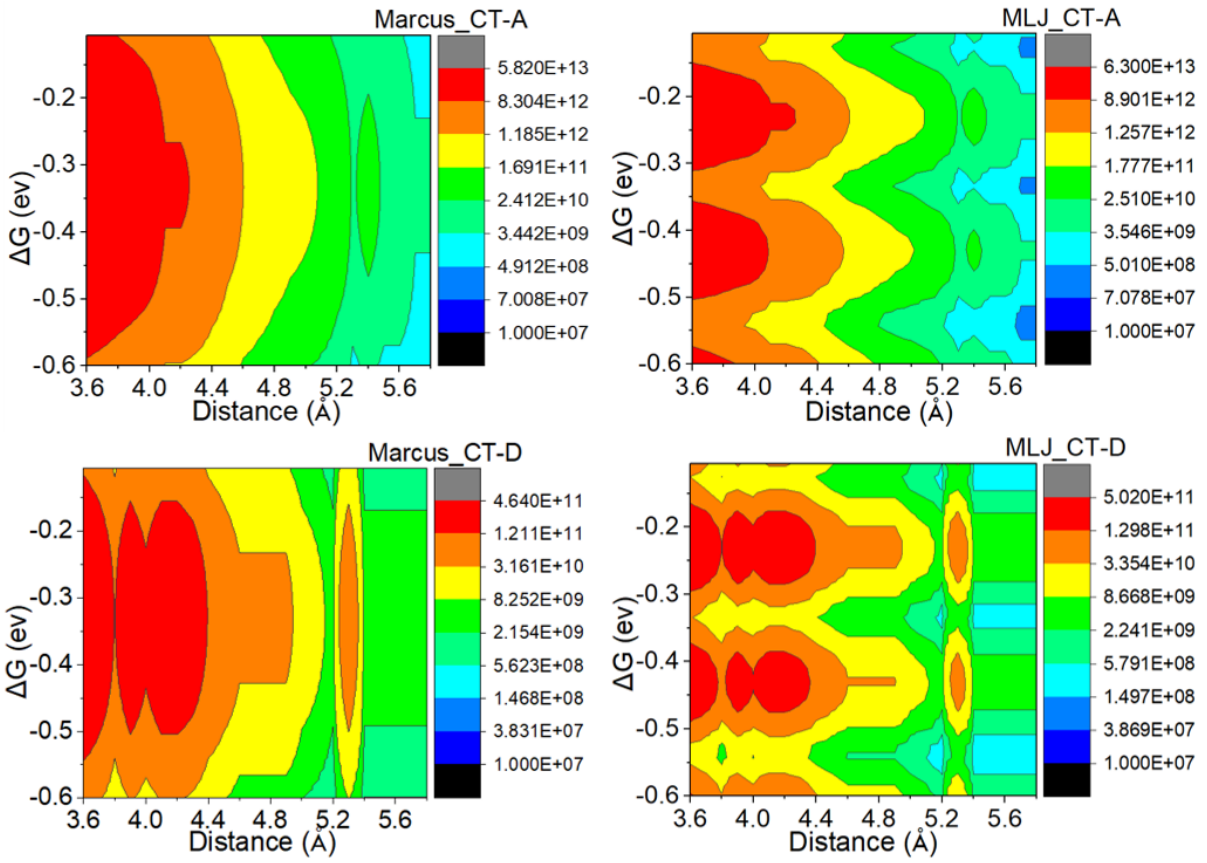

Figure S64: BCT recombination rates from the triplet charge-transfer state to the localized triplet excitation localized on the polymer donor and NFA acceptor, as computed for PTB7-Th:IEICO-2F(G0) using Marcus (left) and Marcus-Levich-Jortner (right) rate expressions. MLJ includes quantum tunnelling through an effective high-frequency vibration of energy 0.2 eV. The total reorganization energy is 0.33 eV in the Marcus calculations and is split into an internal part λ_i of 0.3 eV and an external part λ_s of 0.03 eV in the MLJ calculations. The rates are shown for a range of energy differences between the involved states spanning around the TD-DFT values (along the vertical axis) and as a function of the distance between the conjugated backbones of the interacting donor and acceptor (along the horizontal axis). Recurrences in the MLJ rates are due to tunnelling through successive quantum vibrational states. Recombination into the deeper-lying NFA acceptor is predicted to be one-to-two orders of magnitude faster than to the polymer donor, essentially because of a larger excitonic coupling. Most importantly, the rates decrease exponentially with increasing intermolecular separation as a result of the decreasing wavefunction overlap and excitonic interaction, from values in the range ps^{-1} at close distances to ~ns^{-1} when the molecules are further separated by less than 2 Å. G_i (i=0,1,2,…) represents one possible local minimum on the ground-state potential energy surface of the complex, as probed using dispersion-corrected DFT calculations by changing the initial configuration (namely by translating one molecule with

respect to another longitudinally and/or laterally). The data reported on Fig. 3a of the manuscript correspond to rates obtained using the following set of parameters: $\lambda_i = 0.3$ eV, $\lambda_s = 0.03$ eV, $\Delta G \approx$ -0.3 eV[65].

Singlet and triplet hybridization

A first hint towards hybridization in the singlet manifold is obtained from the sharing of the oscillator strengths among the lowest adiabatic states of the complexes[10,19,66]. From Table S3, it clearly appears that configurational mixing is particularly important in the PTB7-Th:IEICO-2F(G0 and G1) case, where the CT-like singlet borrows significant intensity from the closely-lying localized excited states, while it is less effective in other geometries of the same system, as well as in the other blends. To proceed, it is informative to focus on the PTB7-Th:SiOTIC-4F(G0) vs PTB7-Th:IEICO-2F(G1) complexes, as both systems share the same polymer donor and similar face-to-face orientation, but only the latter shows an inversion of the state ordering with the ^{3}CT state being higher in energy than the ^{1}CT. Because the energy separation between the involved electronic states is similar in the two cases, we hypothesized that the difference in hybridization must be due to the excitonic interactions. Under the reasonable assumption that the wavefunctions for ^{3}CT and T_1 states are captured by single electronic configurations based on the two-level models shown in Figure S68, the excitonic coupling between the many-body wavefunctions can be cast in terms of one-electron transfer integrals among molecular orbitals. For the dominant (as indicated by the BCT rate calculations above) coupling to the NFA acceptor, the relevant transfer integral is between the HOMOs of D and A. Such a matrix element scales with the spatial overlap between the orbitals. We thus plotted the (diabatic) HOMOs of the isolated D and A on a common grid and computed their overlap in Figure S69[67]. We see a substantial difference between the two systems; while for PTB7-Th:IEICO-2F(G1), the two orbitals interact in-phase giving rise to a constructive overlapping pattern (with most contributions being of the same sign), the corresponding orbitals are out-of-phase and yield destructive interactions with alternating regions of positive and negative overlap in PTB7-Th:SiOTIC-4F. Note that this is fully consistent with the 3D transition density cube plots between the adiabatic states involved in the BCT reaction (and that directly enters the GMH excitonic coupling through the corresponding transition dipole moment, $\mu_{CT \to T1(D/A)}$), see Figure S68. The transition density distributions for $CT \to T1(A)$ directly echo the symmetry patterns defined by the orbitals, with contributions along the heterojunction adding up constructively (destructively) to yield a large (smaller) transition moment dipole moment of 2.51D (0.71D) in PTB7-Th:IEICO-2F(G1) (PTB7-Th:SiOTIC-4F(G0)).

PTB7-Th:IEICO-2F							
G0		G1		G2		G3	
Singlet (ev)	f_{osc}	Singlet (ev)	f_{osc}	Singlet (ev)	f_{osc}	Singlet (ev)	f_{osc}
1.41	0.443	1.42	0.554	1.58	0.552	1.56	0.937
1.52	0.318	1.60	0.569	1.59	0.046	1.61	1.563
1.59	1.341	1.65	1.057	1.67	1.553	1.67	0.043
1.74	0.032	1.78	0.006	1.85	0.066	1.78	0.001
1.78	0.001	1.87	0.004	1.89	0.008	1.83	0.048
PTB7-Th:SIOTIC-4F				**PTB7-Th:IEICO-4F**			
G0		G1		G0			
Singlet (ev)	f_{osc}	Singlet (ev)	f_{osc}	Singlet (ev)		f_{osc}	
1.40	0.004	1.42	0.016	1.38		0.375	
1.52	0.304	1.47	0.889	1.49		0.265	
1.55	1.584	1.61	0.966	1.57		1.509	
1.76	0.112	1.75	0.033	1.72		0.035	
1.77	0.085	1.80	0.004	1.75		0.004	

Table S3: Vertical excitation energies and oscillator strengths for the D/A complexes from Figure S65.

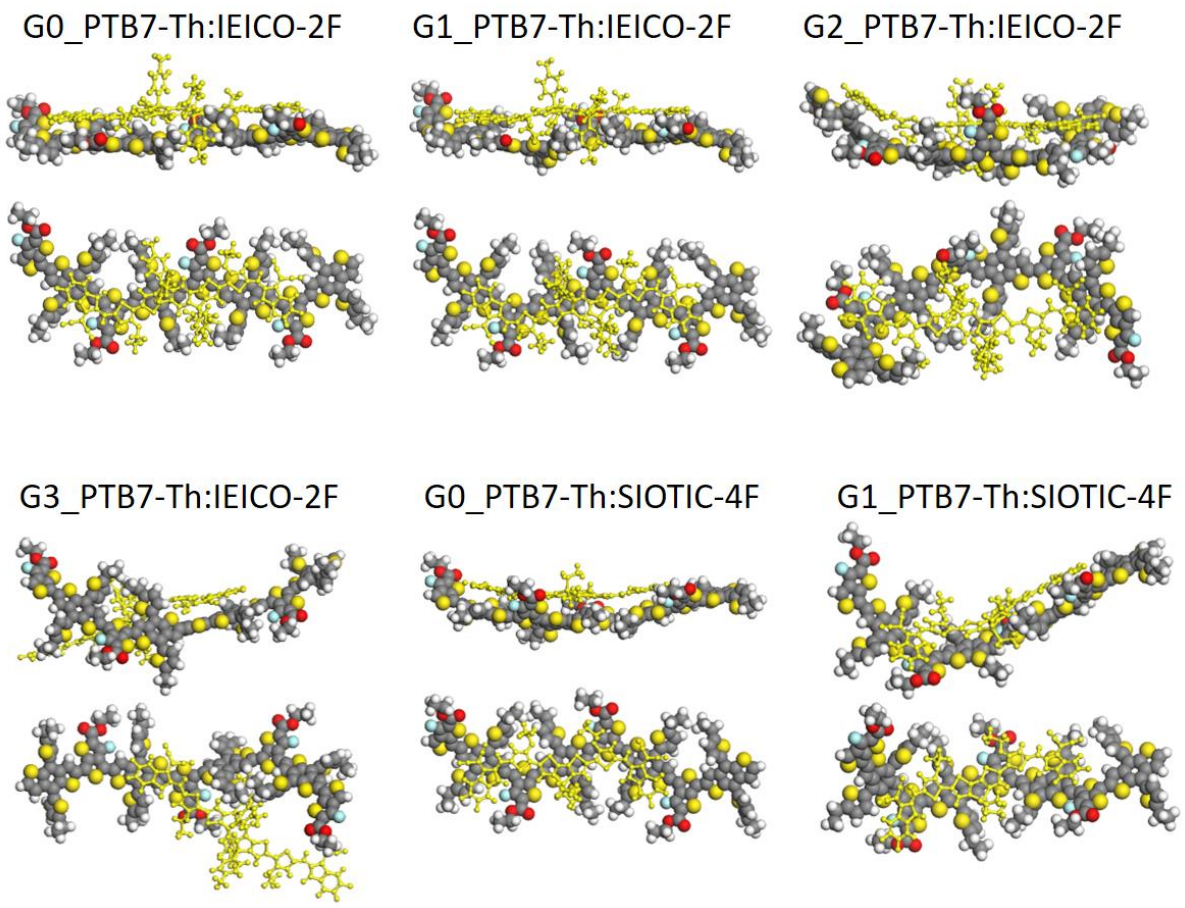

Figure S65: Top- and side-view of polymer/NFA complexes investigated in this work. G_i (i=0,1,2,…) represents one possible local minimum on the ground-state potential energy surface of the complex, as probed by changing the initial configuration (namely by translating one molecule with respect to another longitudinally and/or laterally).

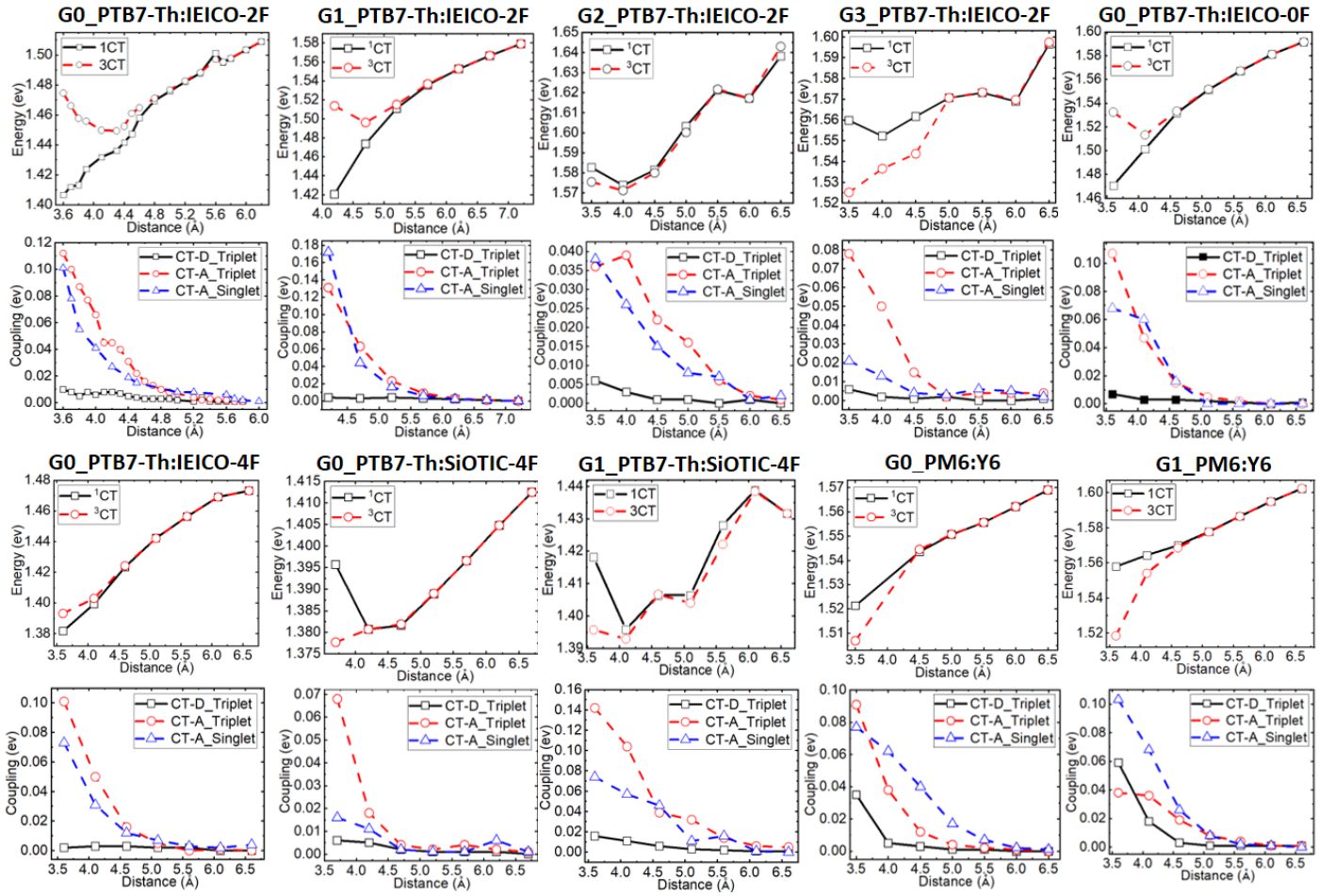

Figure S66: (top) ^{1}CT and ^{3}CT energies and (bottom) couplings between CT and local excitations for the D/A complexes from Figure S65. Note that hybridization, as manifested with an inverted energy ordering of the triplet and singlet CT-like states, is only present for the G0 and G1 geometries of the PTB7-Th:IEICO-2F complex, while G2 and G3 lead to the usual situation with the ^{3}CT being stabilized over the ^{1}CT by exchange coupling. Thus, not surprisingly, the local microstructure has a strong impact on configurational mixing. However, as the most stable PTB7-Th:IEICO-2F complexes do show hybridisation, it is reasonable to suggest that recombination will be funnelled through these lower energy CT sites in a real-world blend. It is also interesting to compare G0_PTB7-Th:IEICO-2F with G0_PTB7-Th:IEICO-0F and G0_PTB7-Th:IEICO-4F. While the two former blends behave similarly, the degree of hybridization is strongly reduced (the lowest singlet and triplet CT-like states are now quasi-degenerate) in G0_PTB7-Th:IEICO-4F because of the larger energy mismatch between the interacting states (associated with the pulling down of the frontier energy levels on the NFA acceptor when grafting additional fluorine atoms). Thus, the energy alignment between the local and the charge-transfer excitations is also critical. None of the geometrical structures generated for PTB7-Th:SiOTIC-4F or for PM6:Y6 (with the constraint of no D/A intermolecular F⋯F interactions at distances <1 nm, imposed from our previous solid-state

NMR studies on the PM6:Y6 blend[19]) result in hybridisation and an inversion in the ordering of the ^{1}CT and ^{3}CT states.

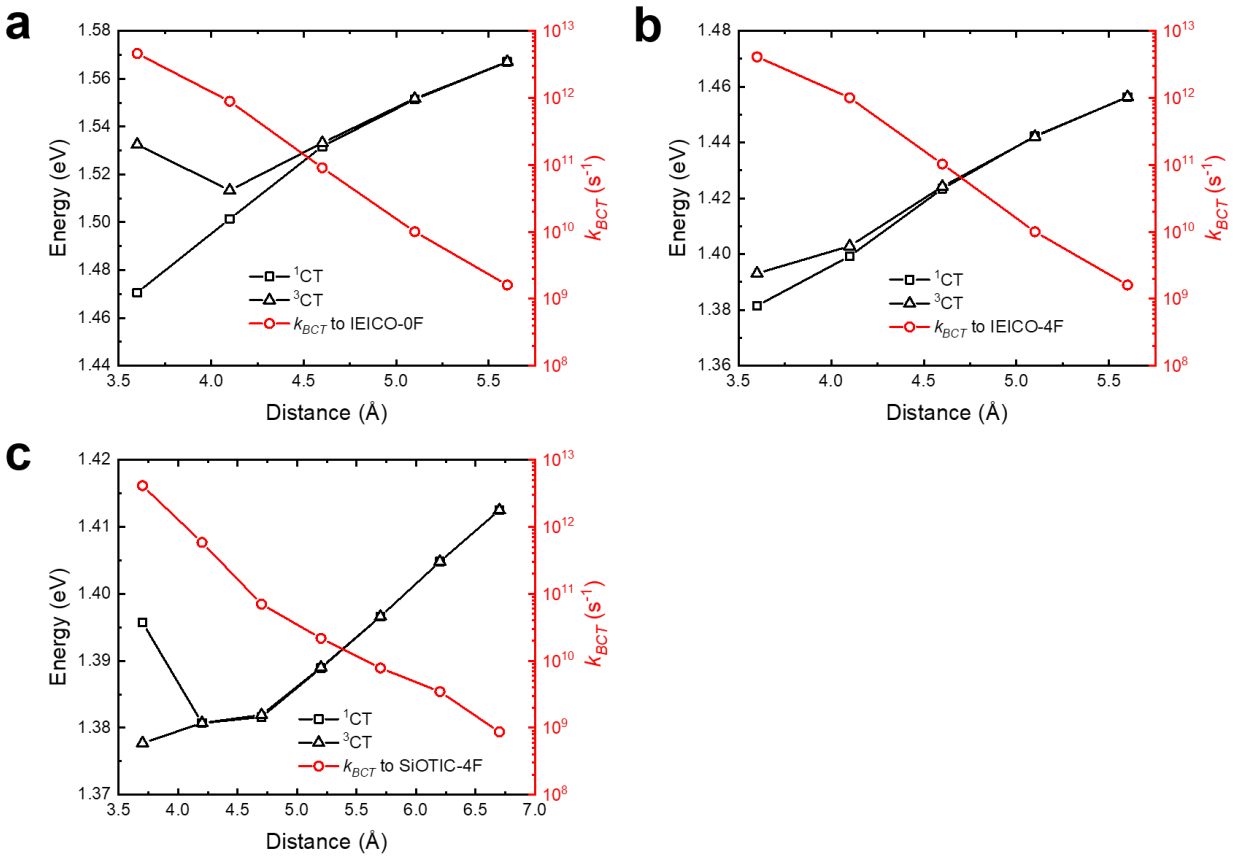

Figure S67: (a) The BCT rate from ^{3}CT to the IEICO-0F T_1 for the PTB7-Th:IEICO-0F "G0" complex as a function of D/A separation, overlaid on the ^{1}CT and ^{3}CT state energies. As with the PTB7-Th:IEICO-2F complex, the inversion of the ^{1}CT and ^{3}CT as a result of hybridisation can clearly be seen. Additionally, the most stable ^{3}CT configuration is no longer at the equilibrium geometry; this increases the separation of the charges in the ^{3}CT state, slowing the BCT process by an order of magnitude. This result is completely consistent with the experimental observations, where there is no evidence for triplet formation via BCT in the PTB7-Th:IEICO-0F blend. **(b)** The BCT rate from ^{3}CT to the IEICO-4F T_1 for the PTB7-Th:IEICO-4F "G0" complex as a function of D/A separation, overlaid on the ^{1}CT and ^{3}CT state energies. In contrast to the PTB7-Th:IEICO-0F and -2F complexes, the ^{3}CT is only slightly destabilised as a result of hybridisation, as discussed in Fig. S66. As the most stable ^{3}CT configuration is still at the equilibrium geometry, it is no longer energetically unfavourable for the charges to approach each other; the BCT rate is not decreased. This is consistent with experimental observations, where IEICO-4F triplets are formed via BCT. **(c)** The BCT rate from ^{3}CT to the SiOTIC-4F T_1 for the PTB7-Th:SiOTIC-4F "G0" complex as a function of D/A separation, overlaid on the ^{1}CT and ^{3}CT state energies. Due to the weak electronic coupling between D and A in this blend, CT-LE hybridisation is not observed and the ^{1}CT and ^{3}CT

energy ordering is as expected from exchange interactions. The BCT rate is therefore not decreased and triplet formation via BCT is observed in this blend.

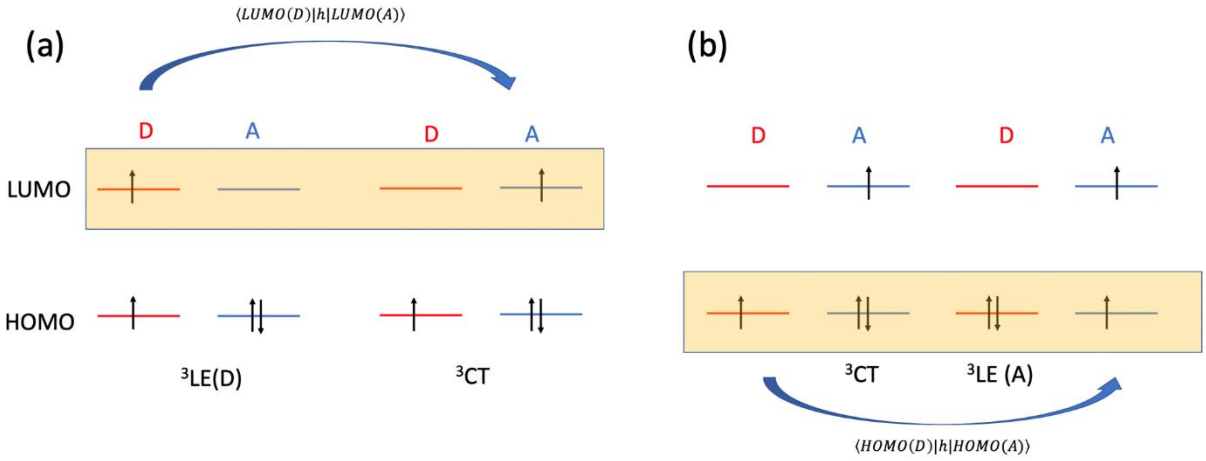

Figure S68: Leading electronic configurations, responsible for the coupling between **(a)** LE(D) and CT and **(b)** LE(A) and CT states.

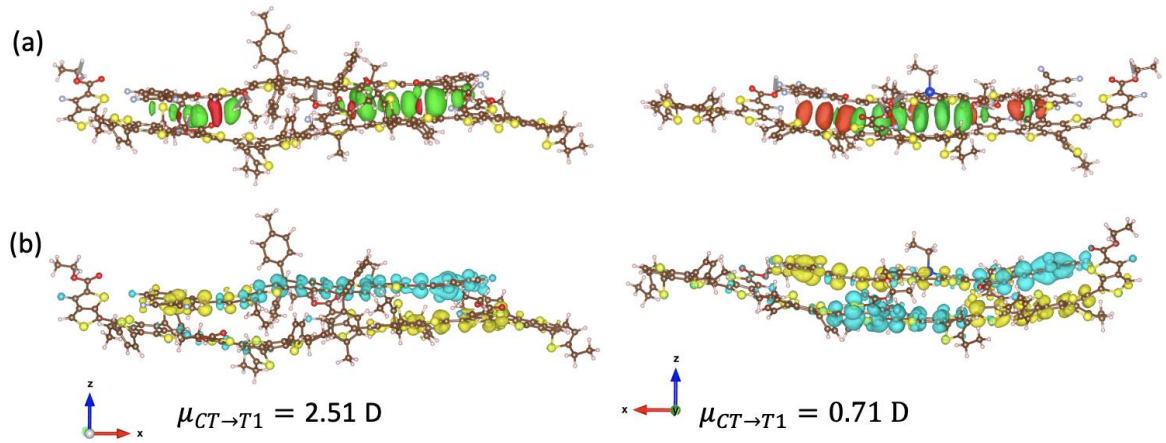

Figure S69: (a) Overlap between HOMOs of D and A and **(b)** transition densities for (left) PTB7-Th:IEICO-2F(G1) and (right) PTB7-Th:SiOTIC-4F(G0).

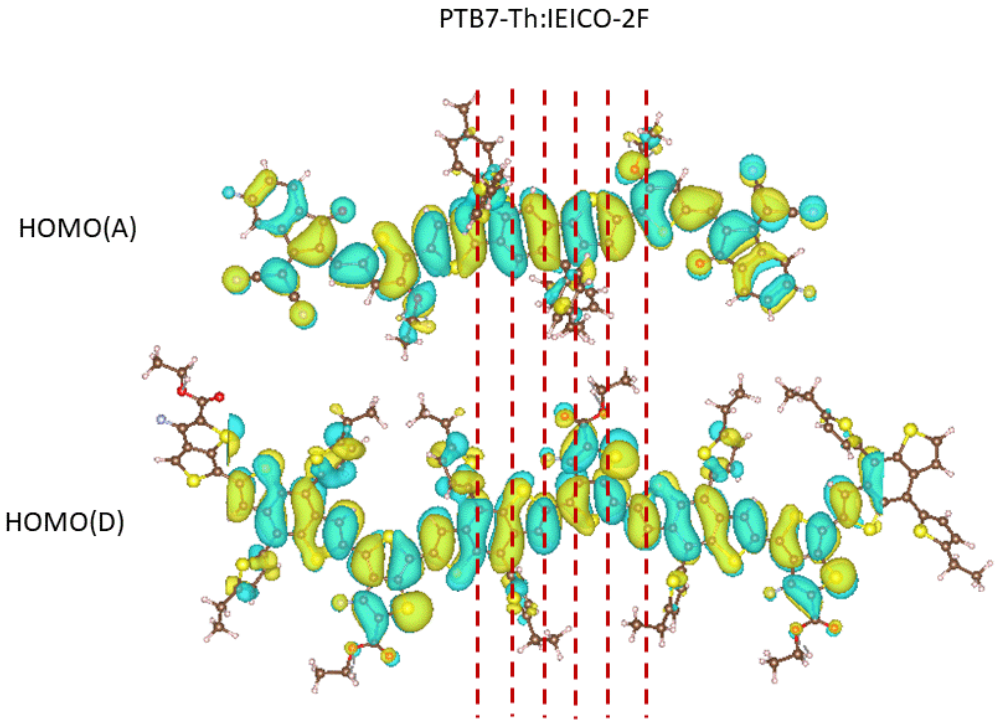

Figure S70: A diagram to demonstrate the strong wavefunction interactions that occur in th PTB7-Th and IEICO combination. As seen from the HOMO wavefunctions of PTB7-Th and IEICO, the MOs on the donor and acceptor molecules feature similar bonding-antibonding patterns (with vertical nodal planes separating regions of maximum electronic density that are indicated by the dashed lines) and, in addition, possess a spatial 'registry' with one another, leading to a sizeable orbital coupling (and, by extension, excited-state mixing, i.e. CTE-LE hybridization).

Bibliography

1. Xue, L. *et al.* Side Chain Engineering on Medium Bandgap Copolymers to Suppress Triplet Formation for High-Efficiency Polymer Solar Cells. *Adv. Mater.* **29**, 1703344 (2017).

2. Wang, R. *et al.* Charge Separation from an Intra-Moiety Intermediate State in the High-Performance PM6:Y6 Organic Photovoltaic Blend. *J. Am. Chem. Soc.* **142**, 12751–12759 (2020).

3. Gelinas, S. *et al.* Ultrafast Long-Range Charge Separation in Organic Semiconductor Photovoltaic Diodes. *Science (80-.).* **343**, 512–516 (2014).

4. Jakowetz, A. C. *et al.* Visualizing excitations at buried heterojunctions in organic semiconductor blends. *Nat. Mater.* **16**, 551–557 (2017).

5. Scarongella, M. *et al.* A Close Look at Charge Generation in Polymer:Fullerene Blends with Microstructure Control. *J. Am. Chem. Soc.* **137**, 2908–2918 (2015).

6. Menke, S. M. *et al.* Order enables efficient electron-hole separation at an organic heterojunction with a small energy loss. *Nat. Commun.* **9**, 277 (2018).

7. Howard, I. A., Mauer, R., Meister, M. & Laquai, F. Effect of Morphology on Ultrafast Free Carrier Generation in Polythiophene:Fullerene Organic Solar Cells. *J. Am. Chem. Soc.* **132**, 14866–14876 (2010).

8. Ziffer, M. E. *et al.* Long-Lived, Non-Geminate, Radiative Recombination of Photogenerated Charges in a Polymer/Small-Molecule Acceptor Photovoltaic Blend. *J. Am. Chem. Soc.* **140**, 9996–10008 (2018).

9. Tamai, Y. *et al.* Ultrafast Long-Range Charge Separation in Nonfullerene Organic Solar Cells. *ACS Nano* **11**, 12473–12481 (2017).

10. Qian, D. *et al.* Design rules for minimizing voltage losses in high-efficiency organic solar cells. *Nat. Mater.* **17**, 703–709 (2018).

11. Menke, S. M. *et al.* Limits for Recombination in a Low Energy Loss Organic Heterojunction. *ACS Nano* **10**, 10736–10744 (2016).

12. Rao, A. *et al.* The role of spin in the kinetic control of recombination in organic photovoltaics. *Nature* **500**, 435–439 (2013).

13. Chow, P. C. Y., Gélinas, S., Rao, A. & Friend, R. H. Quantitative bimolecular

recombination in organic photovoltaics through triplet exciton formation. *J. Am. Chem. Soc.* **136**, 3424–3429 (2014).

14. Hodgkiss, J. M. *et al.* Exciton-Charge Annihilation in Organic Semiconductor Films. *Adv. Funct. Mater.* **22**, 1567–1577 (2012).

15. Bakulin, A. A. *et al.* The Role of Driving Energy and Delocalized States for Charge Separation in Organic Semiconductors. *Science (80-.).* **335**, 1340–1344 (2012).

16. Brédas, J.-L., Beljonne, D., Coropceanu, V. & Cornil, J. Charge-Transfer and Energy-Transfer Processes in π-Conjugated Oligomers and Polymers: A Molecular Picture. *Chem. Rev.* **104**, 4971–5004 (2004).

17. Karuthedath, S. *et al.* Buildup of Triplet-State Population in Operating TQ1:PC 71 BM Devices Does Not Limit Their Performance. *J. Phys. Chem. Lett.* 2838–2845 (2020). doi:10.1021/acs.jpclett.0c00756

18. Gehrig, D. W., Howard, I. A. & Laquai, F. Charge Carrier Generation Followed by Triplet State Formation, Annihilation, and Carrier Recreation in PBDTTT-C/PC 60 BM Photovoltaic Blends. *J. Phys. Chem. C* **119**, 13509–13515 (2015).

19. Karki, A. *et al.* Understanding the High Performance of over 15% Efficiency in Single-Junction Bulk Heterojunction Organic Solar Cells. *Adv. Mater.* **31**, 1903868 (2019).

20. Perdigón-Toro, L. *et al.* Barrierless Free Charge Generation in the High-Performance PM6:Y6 Bulk Heterojunction Non-Fullerene Solar Cell. *Adv. Mater.* **32**, 1906763 (2020).

21. Biskup, T. Structure–Function Relationship of Organic Semiconductors: Detailed Insights From Time-Resolved EPR Spectroscopy. *Front. Chem.* **7**, (2019).

22. Richert, S., Tait, C. E. & Timmel, C. R. Delocalisation of photoexcited triplet states probed by transient EPR and hyperfine spectroscopy. *J. Magn. Reson.* **280**, 103–116 (2017).

23. Weil, J. A. & Bolton, J. R. *Electron Paramagnetic Resonance: Elementary Theory and Practical Applications, Second Edition*. *Electron Paramagnetic Resonance: Elementary Theory and Practical Applications, Second Edition* (2006). doi:10.1002/9780470084984

24. Thomson, S. A. J. *et al.* Charge Separation and Triplet Exciton Formation Pathways in Small-Molecule Solar Cells as Studied by Time-Resolved EPR Spectroscopy. *J. Phys. Chem. C* **121**, 22707–22719 (2017).

25. Righetto, M. *et al.* Engineering interactions in QDs–PCBM blends: a surface chemistry approach. *Nanoscale* **10**, 11913–11922 (2018).

26. Franco, L. *et al.* Time-Resolved EPR of Photoinduced Excited States in a Semiconducting Polymer/PCBM Blend. *J. Phys. Chem. C* **117**, 1554–1560 (2013).

27. Buckley, C. D., Hunter, D. A., Hore, P. J. & McLauchlan, K. A. Electron spin resonance of spin-correlated radical pairs. *Chem. Phys. Lett.* **135**, 307–312 (1987).

28. Hore, P. J., Hunter, D. A., McKie, C. D. & Hoff, A. J. Electron paramagnetic resonance of spin-correlated radical pairs in photosynthetic reactions. *Chem. Phys. Lett.* **137**, 495–500 (1987).

29. Segre, U., Pasimeni, L. & Ruzzi, M. Simulation of EPR and time resolved EPR lineshapes in partially ordered glasses. *Spectrochim. Acta Part A Mol. Biomol. Spectrosc.* **56**, 265–271 (2000).

30. Kobitski, A. Y., Scholz, R., Zahn, D. R. T. & Wagner, H. P. Time-resolved photoluminescence study of excitons in α-PTCDA as a function of temperature. *Phys. Rev. B* **68**, 155201 (2003).

31. Turro, N. J., Ramamurthy, V. & Scaiano, J. C. Modern Molecular Photochemistry of Organic Molecules. *Photochem. Photobiol.* **88**, 1033–1033 (2012).

32. Kotova, M. S. *et al.* On the absence of triplet exciton loss pathways in non-fullerene acceptor based organic solar cells. *Mater. Horizons* **7**, 1641–1649 (2020).

33. Sun, C. *et al.* High Efficiency Polymer Solar Cells with Efficient Hole Transfer at Zero Highest Occupied Molecular Orbital Offset between Methylated Polymer Donor and Brominated Acceptor. *J. Am. Chem. Soc.* **142**, 1465–1474 (2020).

34. Liu, Y., Zuo, L., Shi, X., Jen, A. K. Y. & Ginger, D. S. Unexpectedly Slow Yet Efficient Picosecond to Nanosecond Photoinduced Hole-Transfer Occurs in a Polymer/Nonfullerene Acceptor Organic Photovoltaic Blend. *ACS Energy Lett.* **3**, 2396–2403 (2018).

35. Menke, S. M. & Holmes, R. J. Exciton diffusion in organic photovoltaic cells. *Energy Environ. Sci.* **7**, 499–512 (2014).

36. Ma, C. *et al.* Unraveling the Temperature Dependence of Exciton Dissociation and Free Charge Generation in Nonfullerene Organic Solar Cells. *Sol. RRL* **2000789**, 2000789 (2021).

37. Dimitrov, S. D. *et al.* Polaron pair mediated triplet generation in polymer/fullerene

blends. *Nat. Commun.* **6**, 6501 (2015).

38. Salvadori, E. *et al.* Ultra-fast spin-mixing in a diketopyrrolopyrrole monomer/fullerene blend charge transfer state. *J. Mater. Chem. A* **5**, 24335–24343 (2017).

39. Atherton, N. M. Advanced EPR: Applications in biology and biochemistry. A. J. Hoff (Ed.). Elsevier, Amsterdam. 1989, pp. xxiii +918, ISBN 0-444-88050-X. *Magn. Reson. Chem.* **28**, 737–737 (1990).

40. Stoll, S. & Schweiger, A. EasySpin, a comprehensive software package for spectral simulation and analysis in EPR. *J. Magn. Reson.* **178**, 42–55 (2006).

41. Niklas, J. & Poluektov, O. G. Charge Transfer Processes in OPV Materials as Revealed by EPR Spectroscopy. *Adv. Energy Mater.* **7**, 1602226 (2017).

42. Thomas, T. H. *et al.* Short contacts between chains enhancing luminescence quantum yields and carrier mobilities in conjugated copolymers. *Nat. Commun.* **10**, 2614 (2019).

43. Niklas, J. *et al.* Photoinduced Dynamics of Charge Separation: From Photosynthesis to Polymer–Fullerene Bulk Heterojunctions. *J. Phys. Chem. B* **119**, 7407–7416 (2015).

44. Kraus, H. *et al.* Analysis of Triplet Exciton Loss Pathways in PTB7:PC71BM Bulk Heterojunction Solar Cells. *Sci. Rep.* **6**, 29158 (2016).

45. Köhler, A. & Bässler, H. Triplet states in organic semiconductors. *Mater. Sci. Eng. R Reports* **66**, 71–109 (2009).

46. Hintze, C., Steiner, U. E. & Drescher, M. Photoexcited Triplet State Kinetics Studied by Electron Paramagnetic Resonance Spectroscopy. *ChemPhysChem* **18**, 6–16 (2017).

47. Budil, D. E. & Thurnauer, M. C. The chlorophyll triplet state as a probe of structure and function in photosynthesis. *Biochim. Biophys. Acta - Bioenerg.* **1057**, 1–41 (1991).

48. Sharma, N. *et al.* Exciton efficiency beyond the spin statistical limit in organic light emitting diodes based on anthracene derivatives. *J. Mater. Chem. C* **8**, 3773–3783 (2020).

49. Zhang, G. *et al.* Delocalization of exciton and electron wavefunction in non-fullerene acceptor molecules enables efficient organic solar cells. *Nat. Commun.* **11**, 3943 (2020).

50. Hintze, C., Morgen, T. O. & Drescher, M. Heavy-atom effect on optically excited triplet state kinetics. *PLoS One* **12**, e0184239 (2017).

51. Vandewal, K. Interfacial Charge Transfer States in Condensed Phase Systems. *Annu. Rev. Phys. Chem.* **67**, 113–133 (2016).

52. Refaely-Abramson, S. *et al.* Gap renormalization of molecular crystals from density-functional theory. *Phys. Rev. B* **88**, 081204 (2013).

53. Tomasi, J., Mennucci, B. & Cammi, R. Quantum Mechanical Continuum Solvation Models. *Chem. Rev.* **105**, 2999–3094 (2005).

54. Kronik, L., Stein, T., Refaely-Abramson, S. & Baer, R. Excitation Gaps of Finite-Sized Systems from Optimally Tuned Range-Separated Hybrid Functionals. *J. Chem. Theory Comput.* **8**, 1515–1531 (2012).

55. Refaely-Abramson, S. *et al.* Quasiparticle Spectra from a Nonempirical Optimally Tuned Range-Separated Hybrid Density Functional. *Phys. Rev. Lett.* **109**, 226405 (2012).

56. Henderson, T. M., Izmaylov, A. F., Scalmani, G. & Scuseria, G. E. Can short-range hybrids describe long-range-dependent properties? *J. Chem. Phys.* **131**, 044108 (2009).

57. Frisch G. W.; Schlegel, H. B.; Scuseria, G. E.; Robb, M. A.; Cheeseman, J. R.; Scalmani, G.; Barone, V.; Petersson, G. A.; Nakatsuji, H.; Li, X.; Caricato, M.; Marenich, A. V.; Bloino, J.; Janesko, B. G.; Gomperts, R.; Mennucci, B.; Hratch, D. J., M. J. . T. Gaussian 16, Rev. A.03. *Gaussian, Inc., Wallingford, CT* (2016). doi:111

58. Azzouzi, M. *et al.* Nonradiative Energy Losses in Bulk-Heterojunction Organic Photovoltaics. *Phys. Rev. X* **8**, 031055 (2018).

59. Neuteboom, E. E. *et al.* Alternating Oligo(p -phenylene vinylene)−Perylene Bisimide Copolymers: Synthesis, Photophysics, and Photovoltaic Properties of a New Class of Donor−Acceptor Materials. *J. Am. Chem. Soc.* **125**, 8625–8638 (2003).

60. Zheng, J., Kang, Y. K., Therien, M. J. & Beratan, D. N. Generalized Mulliken−Hush Analysis of Electronic Coupling Interactions in Compressed π-Stacked Porphyrin−Bridge−Quinone Systems. *J. Am. Chem. Soc.* **127**, 11303–11310 (2005).

61. Lu, T. & Chen, F. Multiwfn: A multifunctional wavefunction analyzer. *J. Comput. Chem.* **33**, 580–592 (2012).

62. Marcus, R. A. Electron transfer reactions in chemistry. Theory and experiment. *Rev.*

Mod. Phys. **65**, 599–610 (1993).

63. Pershin, A. & Szalay, P. G. Development of highly accurate approximate scheme for computing the charge transfer integral. *J. Chem. Phys.* **143**, 074109 (2015).

64. Domcke, W. & Yarkony, D. R. Role of Conical Intersections in Molecular Spectroscopy and Photoinduced Chemical Dynamics. *Annu. Rev. Phys. Chem.* **63**, 325–352 (2012).

65. Chen, X.-K., Ravva, M. K., Li, H., Ryno, S. M. & Brédas, J.-L. Effect of Molecular Packing and Charge Delocalization on the Nonradiative Recombination of Charge-Transfer States in Organic Solar Cells. *Adv. Energy Mater.* **6**, 1601325 (2016).

66. D'Avino, G., Muccioli, L., Olivier, Y. & Beljonne, D. Charge Separation and Recombination at Polymer–Fullerene Heterojunctions: Delocalization and Hybridization Effects. *J. Phys. Chem. Lett.* **7**, 536–540 (2016).

67. Momma, K. & Izumi, F. VESTA 3 for three-dimensional visualization of crystal, volumetric and morphology data. *J. Appl. Crystallogr.* **44**, 1272–1276 (2011).